UNIVERSITY OF CALGARY

Coherence of Coupled Dangling-Bond Pairs on the Silicon Surface

by

Zahra Shaterzadeh-Yazdi

A DISSERTATION

SUBMITTED TO THE FACULTY OF GRADUATE STUDIES

IN PARTIAL FULFILLMENT OF THE REQUIREMENTS FOR THE

DEGREE OF DOCTOR OF PHILOSOPHY

DEPARTMENT OF PHYSICS AND ASTRONOMY

CALGARY, ALBERTA

April, 2014

© Zahra Shaterzadeh-Yazdi 2014

UNIVERSITY OF CALGARY

FACULTY OF GRADUATE STUDIES

The undersigned certify that they have read, and recommend to the Faculty of Graduate Studies for acceptance, a dissertation entitled "Coherence of Coupled Dangling-Bond Pairs on the Silicon Surface" submitted by Zahra Shaterzadeh-Yazdi in partial fulfillment of the requirements for the degree of DOCTOR OF PHILOSOPHY.

Chairman, Dr. Denis Leahy
Department of Physics and Astronomy
University of Calgary

Supervisor, Dr. Barry C. Sanders
Department of Physics and Astronomy
University of Calgary

Co-supervisor, Dr. Gino A. DiLabio
Department of Chemistry
University of British Columbia

Dr. David P. DiVincenzo
Department of Theoretical Nanoelectronics
Institute for Quantum Information at RWTH Aachen

Dr. Yujun Shi
Department of Chemistry
University of Calgary

Dr. Dennis Salahub
Department of Chemistry
University of Calgary

Dr. Simon Trudel
Department of Chemistry
University of Calgary

Date

Abstract

We characterize coherent dynamics of closely-spaced dangling bond (DB) pairs positioned on a silicon surface and sharing an excess electron. We investigate whether a coupled-DB pair is a potential candidate for a charge qubit. A dangling bond is an atomic-scale entity that acts like a quantum dot. By shrinking the scale of the quantum dots and the spacing between them, we expect that the excess-electron tunneling rate increases dramatically with decreasing inter-dot separation, while decoherence scales weakly.

Our analysis of the coherent dynamics of coupled-DB pairs shows promise in this respect. Extremely high tunneling rate of the DB excess charge greatly exceeds the expected decoherence rates for a silicon-based system, thereby overcoming the critical obstacle of charge qubit for quantum computing purposes. However, this scaling advantage comes at the price of requiring rapid control and readout. We devise a scheme for measuring the DB-pair dynamics, but investigating the fast control is beyond the scope of this thesis.

Furthermore, we investigate the effect of the silicon-surface structure on the coherence of a coupled-DB pair. The silicon surface of interest is well patterned, but it has an anisotropic structure. Therefore, coupling strength of a DB pair depends on the arrangement of the DBs on the silicon surface. We employ *ab initio* techniques and calculate energy splitting for a wide variety of coupled DB-pair configurations on this surface.

The results show that energy splitting (and consequently the tunneling rate of the DB-pair excess charge) is a function of the DBs' location on the surface and also it strongly depends on the structural orientation of the DBs' orbital. Based on the results, DB-pair configurations are categorized into four groups, such that the changing rate of energy splitting versus DB-pair separation is different among the groups. Knowing about the effect of the surface structure on the DB-pair energy splitting is especially useful when dealing with more complex systems such as DB subnanowires, quantum cellular automata cells, and quantum

computing schemes. Also, the results help to have a better understanding of the coherence and bonding on this Si surface.

As mentioned earlier, the high coherent dynamics of coupled-DB pairs comes at the price of being too fast to be directly measured by any conventional techniques. We therefore devise a scheme to characterize tunneling of the DB excess charge by measuring the time-averaged charge distribution of the DB pair with an atomic force microscope. In our approach, a DB pair is capacitively coupled to an atomic force microscope tip in the presence of an electrostatic potential bias applied along the DB pair, and a tunable mid-infrared laser to drive the pair.

With a non-resonant laser field, the time-averaged charge distribution in the dangling-bond pair is asymmetric as imposed by the bias. However, as the laser becomes resonant with the coherent electron tunneling in the biased pair the theory predicts that the time-averaged charge distribution becomes symmetric. This resonant symmetry effect should not only reveal the tunneling rate, but also the nature and rate of decoherence of single electron dynamics in our system.

Acknowledgements

First and foremost, I am grateful to the almighty Allah, the beneficent and the merciful, for all the things he has provided me so far in my life: health, excellent parents, a beautiful family, great mentors, supportive friends, and most importantly the ability to see and feel all of these great things. Of course, as the Nobel-prize winner G. W. Shaw said "life is not meant to be easy, but take courage: it can be delightful". During the last couple of years, I went through lots of struggles, some of which were serious enough to make me think about giving up on my studies. However, whenever I was about to make my decision, Allah was the one showing me new signs to start over again. He gave me strength and patience to get through the tough times.

I would like to thank my supervisor, Dr. Barry C. Sanders, and my co-supervisor, Dr. Gino A. DiLabio, for their great leadership. Barry taught me how to see the forest for the trees in research, how to lead project while working in a group, and how to be prompt and direct to the point. He provided me with opportunities that helped me discover my hidden skills some of which are: organizing conferences and summer schools, teaching at the graduate level, and mentoring at the undergraduate level. These opportunities helped me build my confidence in communicating with others. I learned from Gino how to communicate with a remotely-access student, how to work responsibly with others with different work styles. After each meeting with Gino, I felt at peace, full of positive energy and satisfied with the discussion, all of which helped me to move forward.

Also, I am very thankful to my parents, Mohsen Shaterzadeh-Yazdi and Azam Doorandish-Yazdi, who supported me with their prayers, wise words, and life experiences. They were and still are such great role models for me with their thoughtful and logical approaches to life's problems and challenges. Now myself being a mother, I know how much care, love, and energy is required for kids to grow up properly. Without any doubt, I cannot compensate

their dedication no matter how hard I try.

I would like to thank my husband, Asgar Khademvatani, who was supportive, helpful, and patient especially during the past year when I needed it the most. Without his help I think it would take me longer to finish up with writing my thesis. Also, I would like to thank my little angel, Fatima, who taught me lots of lessons. Looking at her when she was trying to sit, crawl, and walk, taught me to start from small steps and gradually but continuously practice to achieve big goals, and more importantly never give up on the failures even if it hurts badly. Her laughs, amusement and happiness gave me positive energy when I needed the most. It is a great pleasure to have such a companion in life.

I would also like to thank my friends who supported me and my family in different ways such as keeping in touch with us to make sure that we are okey, helping us with things like grocery shopping, and those who kindly helped with taking care of my daughter when I needed to go to a meeting or seminar. I especially thank our graduate coordinator, Mrs. Tracy Korsgaard, for her supportive and wise words and the inspiring quotes that she shared with me all at the right times. With her support, she greatly helped me complete the last piece of my thesis-writing puzzle.

Last but not least, I would like to thank Dr. Sean D. Barrett for his great suggestion which resulted in shaping one of the three main results of my research work. It was very tragic to hear that he died in an accident while still so young. May his soul rest in peace. During the course of my studies I have also benefited from collaboration with Dr. Bob Wolkow and his group members. Bob's way of talking about dangling bonds has always amazed me. Each time I was with him in a meeting, I really enjoyed his way of putting his thoughts into words. I wish that one day I can explain physics to others like Bob.

This research has been funded by Alberta Innovates Technology Futures. The DFT calculations were enabled by the use of computing resources provided by WestGrid and Compute/Calcul Canada.

Table of Contents

Abstract . . . ii
Acknowledgements . . . iv
Table of Contents . . . vi
List of Tables . . . viii
List of Figures . . . ix
List of Symbols . . . xiv
Thesis Content Previously Published . . . xvi
1 Introduction . . . 1
1.1 Motivation . . . 1
1.2 Research problem and objectives . . . 3
1.2.1 Research Problem . . . 3
1.2.2 Objectives . . . 4
1.3 Coherent dynamics of a coupled dangling-bond pair . . . 5
1.4 *Ab initio* energy splitting for various DBP^- configurations . . . 8
1.5 Scheme for characterizing DBP^- coherent dynamics . . . 12
1.6 Overview of chapters . . . 14
2 Background for System and Methods . . . 16
2.1 Hydrogen-terminated Si(100)–2×1 surface . . . 16
2.2 Bulk and surface phonon modes of Si crystal . . . 19
2.3 Dangling bonds on the silicon surface . . . 22
2.4 Solid-state qubit . . . 25
2.4.1 Semiconductor charge qubit . . . 26
2.4.2 Semiconductor spin qubit . . . 30
2.4.3 Superconductor charge qubit . . . 32
2.5 Extended Hubbard model . . . 32
2.6 Spin–boson model . . . 34
2.7 Wentzel–Kramers–Brillouin approximation . . . 36
2.8 Conclusion . . . 37
3 Background on the Experimental Tools and *Ab Initio* Techniques for DBP^- Characterization . . . 38
3.1 Experimental tools for characterization of DBP^- coherent dynamics . . . 38
3.1.1 Frequency-mode atomic force microscope . . . 38
3.1.2 Scanning tunneling microscope . . . 41
3.1.3 Electric-field biasing and space-charge layer . . . 43
3.1.4 Mid-infrared field . . . 44
3.2 Density-Functional Theory . . . 45
3.2.1 Functional . . . 50
3.2.2 Basis set . . . 52
3.3 Selection and limitations on chosen model chemistry . . . 53
3.4 Time-dependent density-functional theory . . . 56
3.5 Selection and limitations of TDDFT . . . 58
3.6 Summary . . . 59

4 Dangling-Bond Charge Qubit on a Silicon Surface 61
4.1 Dangling-bond pairs as charge qubits 62
4.2 Decoherence analysis for DB-pair qubit systems 65
4.2.1 Decoherence due to Johnson-Nyquist voltage fluctuations 66
4.2.2 Decoherence due to electron-phonon interaction 69
4.3 Quantum dynamics for any number of DBP^-s 72
4.4 Applications to quantum computation 75
4.5 Summary 76
5 Coherence of various DBP^- configurations: *ab initio* approach 78
5.1 Cluster modeling of the Si system 79
5.2 Dangling-bond orbital 84
5.3 Effect of cluster size and surface edges on DBP^- energy splitting 86
5.4 Effect of phosphorous location on DBP^- energy splitting 92
5.5 Replacing phosphorous dopant by an excess charge 94
5.6 Effect of the Si-surface structure on DBP^- energy splitting 95
5.7 Further discussion on the computed results 99
5.8 Summary 101
6 On Measuring Coherence in Coupled Dangling-Bond Dynamics 103
6.1 Dangling bond pair under static bias and driving laser field 104
6.1.1 Static bias 104
6.1.2 Mid-infrared driving field 106
6.1.3 The combined action of static bias and driving field 108
6.1.4 Effect of laser heating on the system 111
6.2 AFM characterization of tunneling between coupled dangling bonds 112
6.2.1 Tip-sample interactions 112
6.2.2 Trapped charge in the tip-sample system 113
6.3 Damped dangling bond pair dynamics 118
6.4 Summary 124
7 Summary, Conclusion and Future Work 126
7.1 Summary and Conclusion 127
7.1.1 DBP^- as a charge qubit 127
7.1.2 Ab initio calculation of DBP^-s energy splitting 128
7.1.3 Proposed scheme for characterizing DBP^- coherent dynamics 129
7.2 Future work 130
Bibliography 134
A Samples used for energy-splitting calculation 154
B From basic theory to computation 158

List of Tables

5.1 Seven sets of clusters, each corresponding to a particular DBP^- configuration. The sets are separated from each other by thick-black lines. This table contains the name of the clusters, DB-pair separation in that cluster (in Å), and the corresponding energy-splitting (in meV). The first two sets correspond to vertical configuration, the next set corresponds to horizontal and the four other sets are diagonal configurations. The clusters are named by $n \times m - Cx$ where n, m and C stand for rows, dimers per row, and DBP^- configuration, respectively. Some of the clusters' name end with a number x representing the order by which DB-pair separation increases for that particular configuration, with $x = 1$ corresponding to the smallest separation. 88

5.2 Energy splitting for all possible DBP^- configurations on cluster 4x4 in the presence and in the absence of dopant P within the cluster. Separation distance between DBs in a pair as well as the distance between P and each DB are given in the second column. The third and fourth columns correspond to the energy splittings, calculated in the presence of dopant P and when P in the model is replaced by a silicon atom plus an excess charge. 95

5.3 Four sets of clusters are available in this table separated from the neighboring ones by thick-black lines. From top to down, the sets correspond to vertical, horizontal, diagonal (DBs-on-same-row), and diagonal (DBs-on-different-rows) configurations, respectively. 97

List of Figures and Illustrations

1.1 (a) Ball-and-stick representation of hydrogen-terminated Si(100)–2×1 surface. The larger (gray) balls represent Si atoms and the smaller (white) balls are hydrogens. Each Si on the surface shares a dimer bond with its neighboring surface Si, and each Si atom is capped by a hydrogen. The inset depicts a top-down view of the surface and shows its bar-like feature. The bars correspond to Si-Si dimers. The notation $R_i, i \in$ {Si-H, Si-Si, row, dimer} represents distances between each Si and its neighbors on the surface. (b) Schematic view of a DBP^- sharing an excess electron located on the H–Si(100)–2×1 surface. Bubbles represent DBs and arrows represent electrons (with spin up or down). The couped DBs have their natural electrons and they share an excess electron provided by P. 6

1.2 (a) A schematic view of the pyramidal-shape of a Si cluster used for the *ab initio* calculations. This cluster is phosphorous-doped (the orange ball) and has hydrogen-terminated Si(100)–2×1 surface (white balls for hydrogen and green balls for Si), with two dangling bonds (purple balls) equidistant from the dopant P. (b)-(e) Four different types of DB-pair configurations on the surface of a cluster–(b) vertical, (c) horizontal, (d) diagonal same-row, (e) diagonal different-rows. The rectangular boxes represent the top-down view of the surface of the cluster given in (a). The short lines inside the boxes are Si dimers on this surface. The black dot accompanied with letter P is the phosphorous dopant and the other two dots are DBs. 10

1.3 (a) A schematic view of our proposed scheme for measuring DBP^- fast coherent dynamics. This scheme consists of: an atomic force microscope tip (AFM) capacitively coupled to the DBP^-, a bias V_b applied along the pair, and a mid-infrared field (MIR) driving the pair. The left (L) and right (R) dangling bonds are shown by bubbles on the Si surface. (b) The dangling-bond pair (DB_L and DB_R) is depicted as a double-well potential with the other elements as described in (a). The AFM tip is sensitive to the time-averaged charge distribution in the DBs, thus yielding the charge distribution ρ_L of the DB pair vs dangling-bond position x. 12

2.1 Woods notation for 2×1 reconstructed surface. Large circles are atoms on the surface plane and small circles are atoms in the underlying substrate. The short horizontal lines connecting the large circles represent surface-atoms dimer bonds. Three rows of surface atom pairs can be seen in this picture. . 17

2.2 Scanning tunneling microscope images of dangling bonds on (a) a low-doped and (b) high-doped n-type Si(100)-2×1 surface. In low-doped crystals, dangling bonds appear as bright spots whereas in high-doped they appear as dark spots. (c) Three coupled-DB pairs where their image brightness depends on DBs separation in each pair. [reproduced from ref. [1], Fig. 1] 24

4.1 (a) Variably spaced qubits in an atom-resolved STM image (46 Å×46 Å, 2 V, 0.2 nA) created from pairs of DBs on a H–Si(100)–2×1 surface, separated by 15.36 Å (qubit A) and 7.68 Å (qubit B). Dangling bonds appear as bright protrusions in the gray scale image. A schematic (left) shows the position of DBs (red and green circles) on the Si surface. Black dashes represent silicon dimers. (b) A DB-DB$^-$ pair modeled as double-well potential, with the extra electron at the left well immediately after initialization to $|0\rangle$. (c) Relaxed ground state of the DB electrons after lattice relaxation has completed. [reproduced from ref. [2], Fig. 1] 63

4.2 Bare tunneling rates of the excess electron in a DBP$^-$ by time-dependent density-functional theory (black circles) and the WKB method (black squares) versus DBP$^-$ separation d. The red line depicts the calculated decoherence rate due to longitudinal-acoustical (LA) phonons. The vertical blue dotted line indicates (to its left) the region in which the two DBs are tunnel coupled. [reproduced from ref. [2], Fig. 3] 65

4.3 Sketch of the gating geometry for our proposed DBP$^-$ qubit on silicon surface. DBs are indicated as red circles and are indexed L and R corresponding to their locations. The electrodes (based on STM tips) are indicated in blue and have fixed potentials V_1 and V_2, with $V_{12} = V_1 - V_2$. The radius of the electrode at the apex is a. [reproduced from ref. [2], Fig. 2] 67

5.1 Ball-and-stick model of the Si cell with two views: (a) along and (b) across a Si-Si dimer. The green balls are silicon atoms and the white ones are hydrogens. This cell contains sixteen layers of Si atoms, where one of the layers is shown by a dashed-horizontal line. The Si-Si dimer on the top layer is framed by an oval box. 81

5.2 (a) A pyramidal cluster that is used for modeling a P-doped Si crystal with a coupled DB-pair on its surface. This cluster has three dimer rows each having five Si dimers. One of the dimer rows is framed by a box. The purple balls on the surface are the silicons that ended with a dangling bond. The DBs are created by removing hydrogen atoms. The orange ball within the cluster represents a phosphorous atom. (b) A schematic view of a coupled DB-pair, DBP$^-$, located on P-doped H-terminated Si(100)–2×1 surface. The bubbles represent DBs and the arrows represent electrons with spin up or down. Each DB originally owns a single electron, and both DBs share an excess electron provided by a doped phosphorous. 82

5.3 Six sample of DBP^- configurations each accompanied by its name, which is composed of the cluster size and the type of DBP^- configuration ('V' for vertical, 'H' for horizontal, and 'D' for diagonal) on that cluster accompanied by a number representing the increasing order of DB-pair separation. Each sample belongs to a particular cluster size. The boxes represent top-down view of hydrogen-terminated Si(100)-2×1 surface and the horizontal short-lines represent Si-Si dimers. The DBs are shown by filled circles and the phosphorous atom doped within the cluster is shown by an open circle and the letter P. DBP^-s on these clusters have either vertical, horizontal, or diagonal configuration. 83
5.4 Representations of the dangling-bond orbital on hydrogen-terminated Si(100)-2×1 surface obtained from a DFT calculation (a) top-down view of the DB orbital and (b) the view along the surface dimer rows. In both images, Si and H atoms are shown by gray and white balls, respectively. The green and red portions of the orbital are representing the relative phases of the dangling bond orbital. The dimers are shown by short-yellow lines. The orientation of the dangling-bond orbital above the Si surface and within the substrate are shown by dash-curved lines. 85
5.5 Separation distances of DBs from 'left' and 'right' surface edges on 3×4, 4×4, and 5×4 clusters. The boxes represent top-down views of hydrogen-terminated Si(100)-2×1 surfaces and the horizontal short-lines represent Si dimers. The DBs are shown by red circles and the phosphorous atom doped within the cluster is shown by a yellow circle and the letter P. The letter 'V' stands for vertical configuration (of DBP^-). 89
5.6 A 3×7 cluster made of 578 atoms. The two DBs are shown with purple balls on the surface of the cluster. The three positions that P can be doped in this cluster are shown by orange balls and named by Px where $x \in \{1, 2, 3\}$. . . . 93
5.7 Log-line graph of DBP^- energy splitting (meV) as a function of DB-pair separation (Å). Each plot corresponds to a specific DBP^- configuration, i.e. vertical, horizontal, diagonal(DBs-on-same-row), and diagonal(DBs-on-different-rows). For vertical and horizontal configurations, the trend is almost linear, indicating that energy splitting for these two configurations varies almost exponentially as a function of DB-pair separation. Diagonal configurations behave somewhat differently than vertical and horizontal configurations. The circle highlights the part that DB-pair separation in different configurations are comparable with each other and indicates how configuration of DB pairs would affect their splitting. 98

6.1 The dangling-bond pair (DB_L-DB_R) is depicted as a double-well potential at the silicon-vacuum interface. An excess electron shown as a red (dark) dot oscillates between the two wells. The DB pair is subjected to a static electric bias and driven by laser radiation. An atomic-force microscope (AFM) tip is capacitively coupled to the DB pair due to electrostatic interaction between charges on the AFM tip (red (dark) zone on tip apex) and the excess electron in the double-well potential. The AFM tip oscillates with a frequency that is dependent on the location of this excess charge thereby modifying the tip oscillation frequency in a predictable way. [reproduced from ref. [3], Fig. 1] . 105
6.2 Time-averaged charge probability in the left DB as a function of applied static bias and under MIR lasers of different frequencies shown in the legend. Here, we have chosen $\Delta = 133$ THz and $\Omega_{\mathrm{MIR}} = 1$ GHz. In the absence of a driving radiation, the result becomes the smooth curve joining all the shown peaks. [reproduced from ref. [3], Fig. 3] 107
6.3 The effects of varying the driving field intensity on the resonance peak shapes. (a) Here ω_{MIR} is kept fixed at 200 THz, and as the field intensity is reduced the resonance peaks become narrower. (b) The peak widths are extracted from the above plots and are plotted against the corresponding Rabi frequencies. The color of each point here corresponds to a plot in (a). The bottom-left point corresponds to the lowest measurable field intensity as limited to the thermal noise in the biasing electrodes. [reproduced from ref. [3], Fig. 4] . . 109
6.4 Contour plots of loci in the parameter space (V_{b}, ω_{MIR}) where resonances occur, i.e. spikes in Fig. 6.2 where $\rho_{\mathrm{L}} = \frac{1}{2}$. Each contour corresponds to a different native DBP^- tunneling frequency Δ, indicated in the legend. [reproduced from ref. [3], Fig. 5] 111
6.5 Schematic of AFM setup for charge sensing, illustrating the geometrical parameters relevant for the tip-sample interactions. The choice of the coordinate system (xOz), the position vector of the DB charge ($\boldsymbol{r}$), and the "boss sphere" (dashed circle) fitted to the apex of the AFM tip are shown. [reproduced from ref. [3], Fig. 7] 113
6.6 AFM frequency shift as the tip scans along a line coinciding with the DBP axis. The three curves correspond to as many equilibrium heights of the AFM tip indicated in the legend, while the other scan characteristics have the values indicated in the text. [reproduced from ref. [3], Fig. 8] 116
6.7 AFM frequency shift (Δf_{AFM}) as a function of static bias ($\mathrm{V_b}$) for four different values of driving radiation frequency given in the legend and Ω_{MIR}= 1 GHz. At each frequency a set of two resonant peaks appear for two symmetric static bias values. [reproduced from ref. [3], Fig. 9] 119
6.8 Location of the resonance peaks in Δf_{AFM} in the two-dimensional parameter space of the static bias and the driving radiation frequency. The DBP^- has a separation of 7.68 Å and the Rabi frequency is Ω_{MIR}= 500 GHz. [reproduced from ref. [3], Fig. 10] 120

6.9 AFM frequency shift as a function of static bias for different decoherence rates shown in the legends and for three chosen values of the Rabi frequency: 1 THz in (a), 100 GHz in (b), and 10 GHz (c). The laser frequency was fixed to ω_{MIR}= 250 THz in all cases. Note the progressive narrowing of the range on the horizontal axis from top to the bottom panels. [reproduced from ref. [3], Fig. 11] 121
6.10 Resonant peak magnitudes in the AFM frequency shift as a function of decoherence rate Γ for different fixed frequency ω_{MIR} of the driving radiation shown in the legend and for a Rabi frequency set at 10 GHz. [reproduced from ref. [3], Fig. 12] 123

A.1 DBP^- configurations on two different sizes of cluster: 3×4 (i.e. 3 rows with 4 silicon dimers per row) and 4×4 (i.e. 4 rows with 4 silicon dimers per row). The rectangular box represents Si(100)-2×1 surface of a desired cluster model; horizontal short lines in each box represent Si dimers, and the red and yellow small circles represent the DBs and the P dopant, respectively. The letters V, D, and H stand for vertical, diagonal, and horizontal DBP^- configurations. . 155
A.2 DBP^- configurations on the cluster size 5×4; each cluster model has 5 rows with 4 silicon dimers per row). The rectangular box represents Si(100)-2×1 surface of a desired cluster model; horizontal short lines in each box represent Si dimers, and the red and yellow small circles represent the DBs and the P dopant, respectively. The letters V, D, and H stand for vertical, diagonal, and horizontal DBP^- configurations. 156
A.3 DBP^- configurations on cluster size $3\times m$ where $m \in \{5, 6, 7\}$; each cluster model has 3 rows and m number of dimers per row. The rectangular box represents Si(100)-2×1 surface of a desired cluster model; horizontal short lines in each box represent Si dimers, and the red and yellow small circles represent the DBs and the P dopant, respectively. The letters V, D, and H stand for vertical, diagonal, and horizontal DBP^- configurations. 157

List of Symbols, Abbreviations and Nomenclature

Symbol	Definition
DB	dangling bond
DB^-	negatively-charged dangling bond
DBP^-	coupled dangling-bond pair sharing an excess electron
Si	silicon
P	phosphorous
DFT	density functional theory
TDDFT	time-dependent density functional theory
QC	quantum computing
QD	quantum dot
QE	quantum engineering
MIR	mid infrared
STM	scanning tunneling microscope
H	hydrogen
WKB	Wentzel-Kramers-Brillouin
EHM	extended Hubbard model
AFM	atomic force microscope
FM	frequency mode
SD	Slater determinant
KS	Kohn-Sham
XC	exchange-correlation
LDA	local density approximation
GGA	generalized gradient approximation
B3LYP	Becke 3-Parameter, Lee, Yang and Parr

RG	Runge Gross
MO	molecular orbital
HOMO	highest-occupied molecular orbital
LUMO	lowest-unoccupied molecular orbital
SOMO	singly-occupied molecular orbital
BSIE	basis-set incompleteness error
BSSE	basis-set superposition error
H	horizontal
V	vertical
D	diagonal
L	left
R	right
CW	continuous wave
LA	longitudinal acoustic phonon
LO	longitudinal optical phonon
PAT	photon-assisted tunneling
QPC	quantum point contact
DEG	two-dimensional electron gas
SET	scanning electron transistor

Thesis Content Previously Published

We have two published papers, the content of which are used in my thesis wherever found appropriate. The main portion of these papers are used in Chapters 4 and 6 either verbatim or with some modifications as required. To avoid redundancy and to keep fluency in my thesis, I used the papers' introduction and background sections only in the relevant chapters of my thesis (see below for more details). In addition, we have an abstract published in the Bulletin of the American Physical Society, but the content is not incorporated into this thesis. Our publications are

1. Zahra Shaterzadeh-Yazdi, Lucian Livadaru, Marco Taucer, Josh Mutus, Jason L. Pitters, Robert A. Wolkow, Barry C. Sanders, Characterizing the rate and coherence of single-electron tunneling between two dangling bonds on the surface of silicon, *Physical Review B* (PRB), **89**(3): 035315 (12 pp.), 28 Jan 2014, arXiv.org:1305.6359v1.

2. Lucian Livadaru, Peng Xue, Zahra Shaterzadeh-Yazdi, Gino A. DiLabio, Josh Mutus, Jason L. Pitters, Barry C. Sanders and Robert A. Wolkow, Dangling-bond charge qubit on a silicon surface, *New Journal of Physics* (NJP), **12**(8): 083018 (15 pp.), 9 August 2010, arXiv.org:0910.1797, chosen by NJP for IOP Select.

3. Zahra Shaterzadeh-Yazdi and Barry C. Sanders, Extended Hubbard model simulations of charge-qubit circuits: from idealism to realism, *Bulletin of the American Physical Society*, **55**, 16 March 2010

The changes that are made to the materials taken from our published papers and used in my thesis are listed as follows:

- Chapter 1: Sections 1.3 and 1.5 each contain some sentences verbatim (but not explicitly marked) from the introduction section of our NJP and PRB papers, respectively.
- Chapter 2: Section 2.1 is copied from background section IIA of PRB paper. Also, Section 2.6 is copied from section 4 of the NJP paper with some modifications.
- Chapter 3: Section 3.1.1 is copied from subsection VA of the PRB paper with some modifications.
- Chapter 4 is mostly composed of the NJP paper. The changes made to the content of this chapter are listed below:
  - The words"DB-DB$^-$", "charge qubit", "DB-DB$^-$ qubit", and any similar word from the NJP paper is changed to "DBP$^-$" in this thesis chapter. All the figures in this chapter are cited to the relevant figures in the NJP paper.
  - Wherever found appropriate, a sentence is added to refer the reader to the background materials given in Chapters 2 and 3.
  - In Section 4.1: the first paragraph is split into two paragraphs with slight modification of words. The third paragraph is removed. The fifth paragraph is greatly modified. Two extra paragraphs are added at the end of this section.
  - The order of Section 4.2 and Section 4.3 is switched as compared to the order given in the NJP paper.

  - Section 4.2 begins with a single paragraph copied and modified from the first paragraph of section 4 from the NJP paper.
  - Subsection 4.2.1 is copied from subsection the 4.1 of NJP paper. $G(\omega)$ in Eq. (9) of the paper is changed to $J(\omega)$ in Eq. (4.1) in this chapter. The last two paragraphs are greatly modified.
  - Subsection 4.2.2 is copied verbatim from subsection 4.2 of the NJP paper; only a sentence is added to refer to background material on phonons.
  - Section 4.3 contains some portions of section 3 of the the NJP paper, but it is extended and greatly modified.
  - Section 4.4 is taken from section 5 of the NJP paper but greatly modified and shortened.

- Chapter 6 is mostly copied materials from our PRB paper. The changes made to the content of this chapter are listed below:
  - All figures in this chapter explicitly refer to the original figures in the PRB paper.
  - Wherever found appropriate, a sentence is added to refer the reader to the background materials given in Chapters 2 and 3.
  - Section 6.1 is copied with some modifications from Sec. III of the PRB paper. This section begins with a few sentences from the last paragraph of Sec. II in the paper. A couple of paragraphs are added to the end of this section, taken verbatim from Sec. IV of the PRB paper.
  - Section IV from the paper is changed to Subsection 6.1.4. The title is changed to "Effect of laser heating on the system" and

only the first two paragraphs from the paper is kept in Subsection 6.1.4.

- Section 6.2: a couple of sentences are added to the first paragraph.
- Section 6.3 is copied verbatim from section VI of the PRB paper.
- Section 6.4: a few sentences (about H-Si vibrational range) are taken out and moved to the background chapter, Section 2.2.

Chapter 1

Introduction

"People are like crystals. It is the defects in them that makes them interesting." *Sir F. C. Frank*

1.1 Motivation

Quantum computing (QC) enables some computational problems to be solved faster and more efficiently than would ever be possible with any conventional computer. Establishment of some important quantum algorithms [4, 5] has motivated scientists to look for feasible architectures for quantum computing. It has been speculated that the solid-state QC implementation is a suitable candidate because of the stability and possible scalability of solid-state systems. Among the suggested solid state QC schemes [6, 7, 8, 9, 10, 11], semiconductor implementations, especially in silicon, are particularly attractive because of the advanced state of silicon technology and the desire to integrate standard silicon-chip computing with quantum computation.

The first Si-based QC scheme was proposed by Kane in 1998, and it was based on the nuclear spin of phosphorous atoms buried in the silicon (Si) crystal [9]. Impressive progress has been achieved since then in developing silicon-based QC implementations not only with nuclear spin, but also with electron spin [12, 13, 14, 15] as well as electron charge [10, 11, 15]. A recent breakthrough towards Si-based QC was the experimental achievement of atomic precision in positioning phosphorous dopants in the Si crystal [16, 17]. However, despite all the achievements in this area, there are still serious obstacles remaining for realizing such schemes, at the heart of which are the challenges in realizing the qubit.

The qubit is the unit of quantum information and it is used as the building block for quantum computation and quantum communication. Quantum information is built on a

framework of logical qubits. Nature provides two-level systems that can serve as a physical means for encoding, processing and decoding quantum information. Whether physical qubits suffice for quantum information processing depend on whether they satisfy necessary conditions such as DiVincenzo's criteria [18]. Strictly speaking, these physical qubits and their operations are adequate if they meet the threshold condition for fault-tolerant quantum error correction [19, 20].

In silicon-based QC schemes the qubit is physically realized in the form of electron charge, electron spin and nuclei spin. The spin qubit, which is a superposition of spin up and down, has a long lifetime but faces severe challenges such as readout. A promising approach to read the spin qubit is to first convert it to a charge qubit [21], which is a superposition of charge in two locations (assuming that the spin degree of freedom is stationary). Thus, the semiconductor charge qubit is important both as a quantum information carrier and as an intercessor for spin-qubit measurements.

The semiconductor charge qubit manifests as a pair of coupled quantum dots (QD) that share a single electron via coherent tunneling [10, 11, 22]. The charge qubit also faces some obstacles such as the spread of tunneling rate due to variation in the size and positioning of QDs. Also, it suffers from a short coherence time [13, 23] due to environmental noise effects such as the semiconductor's surface and bulk phonon modes, stray charges in the system, charge carriers of the electronic gates, and the charges trapped in surface dangling bonds (DBs).

To overcome at least some of these obstacles, one should look for the right type of QD. We propose using silicon-surface dangling bonds as tunnel-coupled quantum dots sharing a controllable number of electrons in order to deal with some of the challenges of charge qubit [1, 2, 24]. Dangling bonds are identical in shape and their spacing is determined by the surface structure of the silicon crystal. Furthermore, fabrication of relatively large assemblies of DBs can be achieved using a scanning tunneling microscope [25], which is a

nanotool with atomic-scale precision, reliability, reproducibility, and virtually no variability at the single dot level. We predict that the excess electron shared in a pair of DBs is highly coherent [2]. Details on coupled-DB pairs (DBP^-) will be presented in the following sections.

1.2 Research problem and objectives

The aim is to turn coupled dangling-bond pairs (where DBs are known as semiconductor defects) into a useful tool for implementations at the quantum level. A dangling bond is an unsaturated bond located on a semiconductor surface [26, 27, 28]. Structural and electronic properties of DBs have been studied extensively [29, 30, 31, 32]. Also, recently various implementations of DBs have been explored with possible applications for engineering new devices on silicon surfaces [1, 33, 34, 35].

A dangling bond naturally possesses a single electron; hence it is capable of undergoing a chemical reaction with atomic and molecular species, or bonding with another DB. Alternatively, a DB can become negatively charged by hosting an excess electron either provided by a donor source such as a phosphorous (P) atom doped within a semiconductor material, or by trapping a stray charge from the semiconductor's conduction band.

1.2.1 Research Problem

For the first time in 2009, it was experimentally shown that pairs of appropriately separated DBs are coupled with each other and they precisely share one excess electron [1]. Also, the experiment illustrated that the coupling strength of the DB pairs depends on the separation distance between the two DBs. However, whether this coupling is coherent or not remains as an open question. This feature has opened up a new area of interest about coherent dynamics of coupled DBs on a silicon surface with the potential of employing them in devising quantum computing schemes and also utilizing them as building blocks for more complex nanosystems such as DB sub-nanowires [33] and quantum cellular automata cells [1, 25].

Dangling bonds are excellent candidates for quantum dots as they display localized features, have truly atomic-scale size, and are identical in shape. Furthermore, DBs can relatively easily be fabricated by selectively removing hydrogen atoms from a hydrogen-terminated Si surface by means of a scanning probe such as scanning tunneling microscope tip [1, 2, 24]. Therefore, as surface entities, DBs are directly amenable to control and read-out, and they can be precisely positioned within subnanometer distance from each other.

Considering the DB features listed above, a DBP^- is a potential candidate for a charge qubit, conditioned to having long coherence times. It may be impossible or hard to overcome decoherence due to inherent noises in the silicon crystal, but the atomic size of DBs helps to reduce inter-DB separation, leading to exponential increase in the tunneling rate of the DB-pair's excess electron. Also, the identical shape and controllable positioning of DBs prevent variation of tunneling rate. Thus, by employing DB as quantum dot, one can defeat the obstacles of other proposed QD charge qubits.

1.2.2 Objectives

In this thesis three objectives are pursued. First, we use proper theories to estimate coherent dynamics of DBP^-s on the phosphorous-doped hydrogen-terminated Si(100)–2×1 surface. Due to its well-ordered surface functionality, this Si surface is one of the most commonly used surfaces in the Si-wafer fabrication technology [36]. Therefore, analyzing the coherent dynamics of the DB pairs on this surface provides the opportunity to hybridize our system with the existing Si infrastructure technology.

As the second objective, we investigate the effect of the Si-surface structure on the coupling strength of various DB pairs. Although the Si surface of interest is well ordered, it has an anisotropic structure. Thus, the coupling strength of a DB pair (and consequently the tunneling rate of its excess charge) is expected to depend on the location of the corresponding DBs on the surface. We employ *ab initio* techniques to calculate energy splitting for various DBP^-s with different configurations on this surface. The calculated results help

us to choose a proper DB-pair configuration with the desired coherent dynamics for QC and QE implementations.

Our third objective is to devise a scheme for experimentally characterizing DB-pair coherent dynamics. Based on our theoretical estimations, the high tunneling rate of the DB excess-charge greatly exceeds any experimental capability to resolve at such a fast timescale. Thus, it is impossible to directly detect the dynamics of a DB pair from an experiment. We propose a scheme to indirectly retrieve information about the dynamics of a DB pair. This information helps to characterize the tunneling rate as well as the nature and rates of decoherence. In the following sections each objective is described in more detail.

1.3 Coherent dynamics of a coupled dangling-bond pair

A schematic view of the hydrogen-terminated Si(100)–2×1 surface is depicted in Fig. 1.1(a). On this surface, each silicon atom shares two bonds with the silicons in the bulk, has one bond with another surface silicon, and is capped by a hydrogen atom. A hydrogen can be removed by a scanning probe, thereby creating a dangling bond [26, 28, 37]. A dangling bond has only one confined electron with an energy state located within the Si crystal bandgap. Consequently, the energy state of a DB is decoupled from the crystal's conduction and valence bands, and this leads to the localized feature of the DB.

A DB can lose its single electron to the bulk, thereby becoming a positively charged DB^+, or it can host one excess electron (with opposite spin) from the bulk, hence becoming negatively charged DB^-. Losing or acquiring charge depends on the type and amount of doping in the host crystal, and on temperature. The crystal of our interest has a high concentration of n-type phosphorous doping, therefore each DB is highly likely to become negatively charged by carrying an excess electron [1].

Although, in the Si system of interest, an individual DB is most likely negatively charged, experiments show that for DB pairs with a separation less than 16 Å, the two DBs display

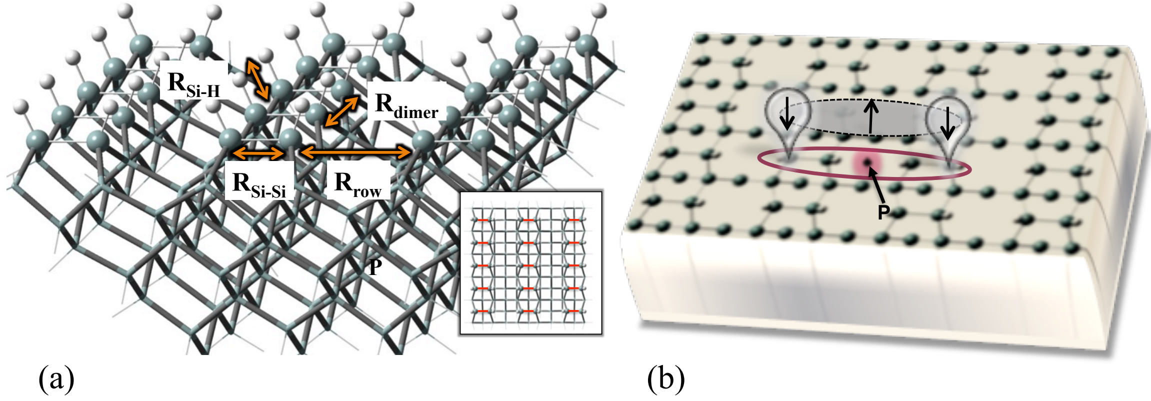

Figure 1.1: (a) Ball-and-stick representation of hydrogen-terminated Si(100)–2×1 surface. The larger (gray) balls represent Si atoms and the smaller (white) balls are hydrogens. Each Si on the surface shares a dimer bond with its neighboring surface Si, and each Si atom is capped by a hydrogen. The inset depicts a top-down view of the surface and shows its bar-like feature. The bars correspond to Si-Si dimers. The notation $R_i, i \in \{\text{Si-H, Si-Si, row, dimer}\}$ represents distances between each Si and its neighbors on the surface. (b) Schematic view of a DBP$^-$ sharing an excess electron located on the H–Si(100)–2×1 surface. Bubbles represent DBs and arrows represent electrons (with spin up or down). The couped DBs have their natural electrons and they share an excess electron provided by P.

coupling behavior [1, 25]. In fact, when the second DB is created within 16 Å of the first one, the strong Coulombic repulsion from the existing extra electron (located in the first DB) prevents the second DB to host an extra charge. The resulting configuration is a coupled-DB pair with the excess electron shared between the two DBs by tunnel coupling; see Fig. 1.1(b).

The excess electron tunnels between the two DBs with a rate that is a function of DB-pair separation distance. In addition, the excess-electron tunneling rate also depends on the geometry of the Si surface between the two DBs. Our theoretical estimations show that DB-pair tunneling rate has an upper and lower bound of $\sim$ 467 THz and $\sim$ 0.1 THz corresponding to the minimum and the maximum separation between the two DBs, respectively. The minimum separation is $\sim$ 3.84 Å, determined by the structure of the Si surface and the maximum separation is 16 Å, as stated above.

The excess electron, which is oscillating between the two DBs of a DB pair, can behave

as a two-level system in the sense that, in the position representation, the states of the system can be given in terms of the left and the right states. A useful alternative to the left and the right states is the symmetric and antisymmetric states, corresponding to the two lowest-lying energy levels of the DB-pair excess electron. These two states are given by linear superpositions of the left and the right states.

Based on our *ab initio* calculations, the symmetric and the antisymmetric states of a DBP^- are within the Si-crystal band gap [2]. The higher energy levels are all above the band gap. Consequently, any excitation of the excess electron to a higher energy level results in the electron loss to the bulk or the conduction band of the Si crystal. Hence, the two-level system approximation yields an excellent model for a DBP^-. However, for such a two-level system to be useful as a charge qubit, the oscillating excess electron should have long coherent dynamics.

Coherence of a DBP^- can be estimated by assessing the tunneling rate and the decoherence rates of the excess electron and finding the ratio between them. This ratio indicates the electron's number of oscillations before it decays due to environmental noise effects. The larger this ratio, the longer the DBP^- coherence.

We used two different approaches for calculating the tunneling rate of the DBP^- excess charge. For small DB-pair separations ($d_{\mathrm{DBP}^-} < 8$ Å), *ab inito* density functional theory (DFT) was used. For larger separations ($d_{\mathrm{DBP}^-} > 8$ Å), the size of the Si cluster model used for DFT computation becomes prohibitively expensive. Thus, we used a simpler method called Wentzel-Kramers-Brillouin (WKB) approximation to estimate the excess-charge tunneling rate.

For analyzing decoherence due to noise in our system, we employed the spin-boson model [38]. This is a well-established model for characterizing coupling between a two-level system and a generic bosonic bath corresponding to the relevant sources of noise. Based on the earlier studies on silicon systems [13, 39, 40], we estimate that the main sources of noise

in our system are the voltage fluctuations on the gate electrodes and the interaction between the DBP$^-$ and phonons in the silicon bulk and at the surface.

Decoherence due to stray charges in the silicon crystal is believed to be small [1], because the spacing between DBs in a DBP$^-$ is much smaller than distances to the nearest trapped charges in the semiconductor. Also, to avoid the effect of spin coupling with the host nuclear spins, we consider using ^{28}Si, which is a spinless isotope of silicon. Decoherence due to coupling with the spin of phosphorous atom is estimated to be $\approx 10^{-8}$ sec which is several orders of magnitude smaller than the tunneling time estimated for the DBP$^-$ excess charge.

Our analysis show that DBP$^-$ tunneling rate increases exponentially with decreasing DB separation, while decoherence rates scales weakly. For the particular model that we used, the ratio between the resultant tunneling rate and decoherence rate reaches above the threshold for fault-tolerant quantum computation [41]. Thus, DBP$^-$ has the potential to be a great candidate for semiconductor charge qubit.

As one step further, we also formulated the dynamics for N number of DBP$^-$s by adapting the extended Hubbard model (EHM) [42]. We assumed that the DBP$^-$s are put in a well-patterned form similar to the circuit-model proposed by Kane for the spin-qubit QC system [9]. We modified the EHM model by adding an extra term corresponding to the inter-DB potential bias. This term comes into play when control over the electron tunneling rate is required, and it can be used for instance when employing DBP$^-$s as the building blocks of a quantum computing architecture.

1.4 *Ab initio* energy splitting for various DBP$^-$ configurations

The hydrogen-terminated Si(100)–2×1 surface has an anisotropic structure. On this surface, any Si shares a dimer bond with its neighboring Si atom, such that the top-down view of the surface displays rows of Si-Si dimers; see the inset in Fig. 1.1(a). Spacing between the Si dimers in a single row is smaller than the spacing between the neighboring rows. Thus,

the coupling strength of a DBP^- and consequently the tunneling rate of the corresponding excess electron depend on the arrangement of the two DBs on the Si surface. Using *ab initio* techniques, we calculate the energy splitting for a wide variety of DBP^- configurations in order to investigate the effect of the surface structure on the excess-charge tunneling rate.

The tunneling rate of the excess electron is directly proportional to the energy difference (also called energy splitting) between the two lowest-lying energy states of the excess electron, i.e. the ground state and the first excited state. We use *ab initio* density functional theory (DFT) and time-dependent DFT to calculate the energies corresponding to the ground state and the first excited state of a DBP^-, respectively. Learning about the tunneling rate of different DBP^- configurations becomes specially important and useful when DBP^-s find applicability in larger systems, such as designing a QC scheme.

In order to calculate (from first principles) the ground-state energy of a DBP^- on a piece of Si crystal, one should solve the Schrödinger equation for a system of N nuclei and M electrons that are all interacting with each other. The Schrödinger equation is a function of spatial and spin coordinates of the system's particles. Thus solving the Schrödinger equation for such a large system is practically impossible due to the large number of unknown variables as well as the limitations on the required computational resources.

Density functional theory resolves this obstacle by considering the Schrödinger equation as a functional (i.e. a function of function) of the system's electron density, rather than a function of the spatial and spin coordinates. This technique is built based on a theorem [43] stating that there is a one-to-one correspondence between the electron-density of a system and its ground-state properties. Thus, knowing the electron density of a system is sufficient for determining any other properties of that system. To calculate the ground-state energy, DFT optimizes system's molecular geometry and then computes the corresponding energy [44].

Time-dependent density functional theory (TDDFT) is an extension of DFT, and their

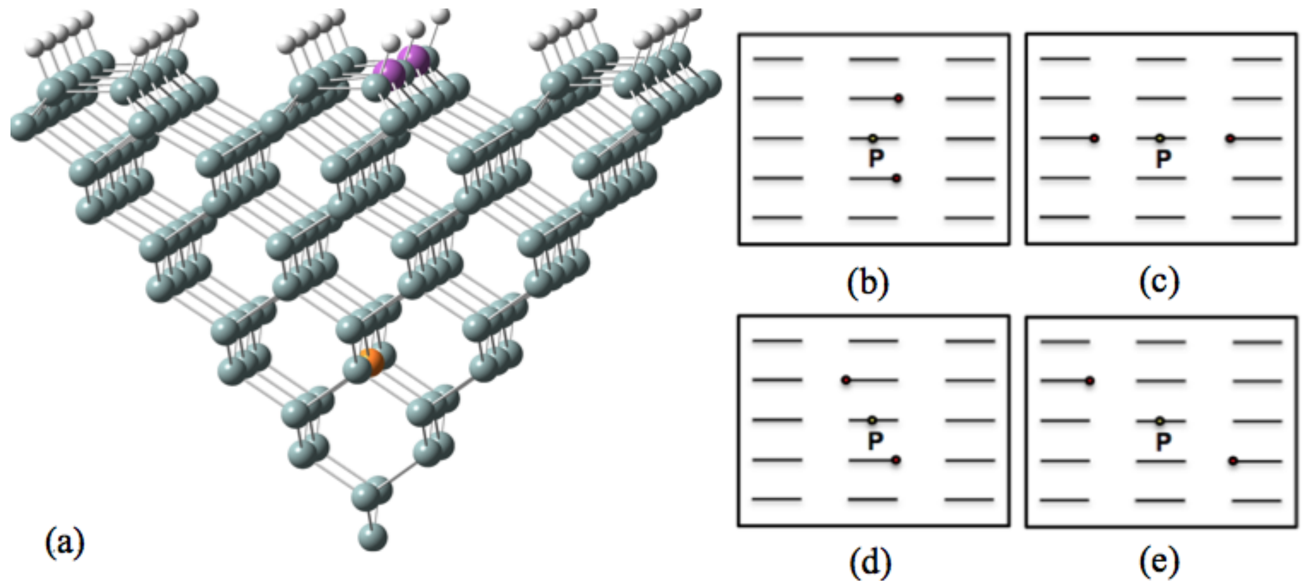

Figure 1.2: (a) A schematic view of the pyramidal-shape of a Si cluster used for the *ab initio* calculations. This cluster is phosphorous-doped (the orange ball) and has hydrogen-terminated Si(100)–2×1 surface (white balls for hydrogen and green balls for Si), with two dangling bonds (purple balls) equidistant from the dopant P. (b)-(e) Four different types of DB-pair configurations on the surface of a cluster–(b) vertical, (c) horizontal, (d) diagonal same-row, (e) diagonal different-rows. The rectangular boxes represent the top-down view of the surface of the cluster given in (a). The short lines inside the boxes are Si dimers on this surface. The black dot accompanied with letter P is the phosphorous dopant and the other two dots are DBs.

conceptual and computational foundations are analogous to each other [45]. Time-dependent DFT investigates the dynamics and the change in structural properties of a system in the presence of a time-dependent external perturbation. We employ time-dependent DFT to compute the energy of the first excited state of our system.

We model our system using Si clusters made of hundreds of Si atoms. Dangling bonds are created on a cluster by removing hydrogen atoms from the silicons of the surface. The DBP^- excess electron is provided by a doped phosphorous (P) atom, simply by replacing one of the Si atoms within the cluster with phosphorous. Some limitations are applied to the location of DBs and P to avoid significant errors in computation: DBs can not be positioned on the silicons of the surface borders as these Si atoms should be fixed in place by hydrogens for computational purposes. Also, P should be surrounded by a layer of silicon atoms and

it should not be in direct contact with DBs and with the lateral surfaces of the cluster.

The desired shape for a Si cluster is an upside-down pyramid with a DB pair on its base and a P atom equidistant from both DBs and doped in a location within the cluster so that it satisfies the conditions listed above; see Fig. 1.2(a). The pyramidal shape helps the bonds on the lateral surfaces to be appropriately terminated by fixed-in-place H atoms while preventing the H atoms to overlap each other. Furthermore, the pyramidal shape reduces computational costs (i.e. memory, processor and time) as compared to the cost associated with a cubic Si cluster.

We have three types of DBP^- configurations, namely vertical, horizontal, and diagonal; see Fig. 1.2(b). The computed results show that although the energy splitting of DBP^-s decreases with the increase of DBs separation, the rate of decrease is different from one configuration to the other. The rate difference is partially due to surface structure influencing each configuration differently, but it is also related to the shape and orientation of DBs orbital and the degree of overlap between them. Based on the results, we categorize DBP^-s into four different groups each corresponding to a particular configuration.

The size of cluster and the location of P can be potential sources of error in our calculations. We tested the effect of the former source by looking at a particular configuration on different cluster sizes. As a result, we found a lower bound on the size of the cluster in order to reduce its effect on the DBP^- energy splitting.

We used two different methods to check the effect of P location on the results: (1) by placing P at different depths of a cluster and looking at its effect on a particular DBP^- splitting, and (2) by replacing P with a Si but instead adding an excess charge to the system. According to the results, we found that P should not be very close to DBs to avoid strong interaction with them. On the other hand, as P gets further away from the DB pair, the results converge to a unique value, indicating that P would look like an excess charge for sufficiently far distances from DBs.

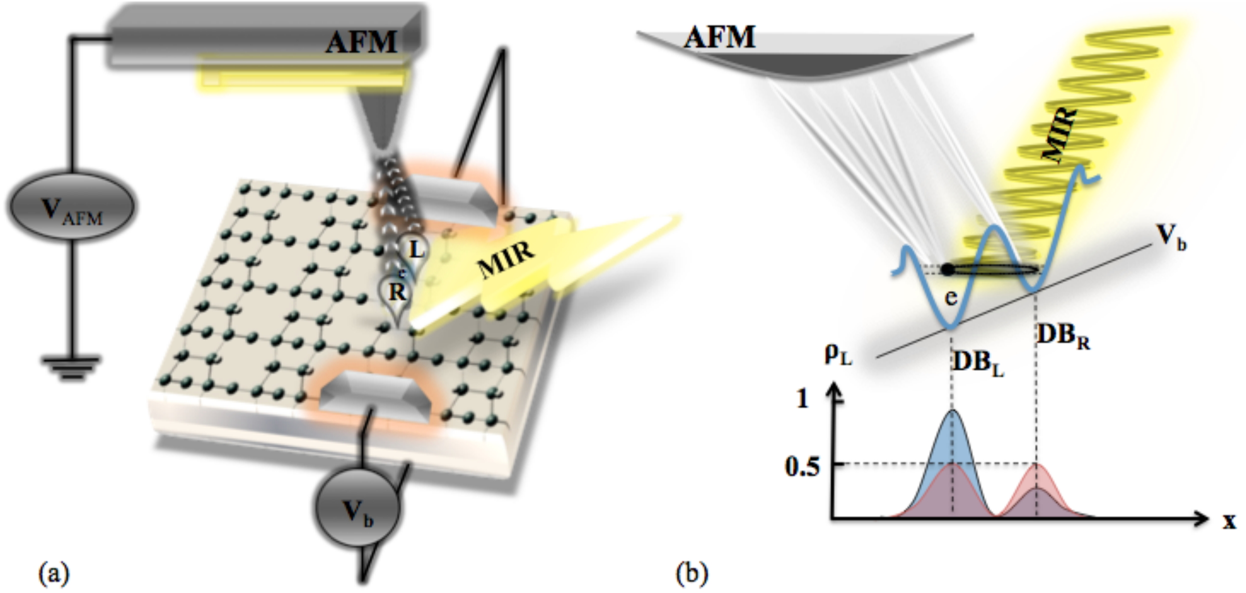

Figure 1.3: (a) A schematic view of our proposed scheme for measuring DBP^- fast coherent dynamics. This scheme consists of: an atomic force microscope tip (AFM) capacitively coupled to the DBP^-, a bias V_b applied along the pair, and a mid-infrared field (MIR) driving the pair. The left (L) and right (R) dangling bonds are shown by bubbles on the Si surface. (b) The dangling-bond pair (DB_L and DB_R) is depicted as a double-well potential with the other elements as described in (a). The AFM tip is sensitive to the time-averaged charge distribution in the DBs, thus yielding the charge distribution ρ_L of the DB pair vs dangling-bond position x.

The results of our calculation give us an insight on how the Si-surface structure is affecting the DBP^- energy splitting. Learning about different configurations of DBP^- helps us in choosing the appropriate type of DBP^-s when it comes to employing them in larger-scale systems such as building quantum cellular automata cells, devising quantum computing schemes and performing quantum engineering with a set of DBs.

1.5 Scheme for characterizing DBP^- coherent dynamics

The feature of fast tunneling and high coherence of DBP^-s comes at the price of some considerable practical difficulties. For instance, direct characterization of DBP^- dynamics by monitoring the oscillation of the DB excess-electron is not feasible electronically by any straightforward methods. To resolve this problem, we propose a strategy to measure the rate

and coherence of tunneling by controlling and monitoring time-averaged charge distribution in pairs of coupled DBs [46]. These measurements are inspired by previous experiments on double quantum-dot structures with tunneling rates in the microwave regime [47, 48].

Figure 1.3(a) shows our proposed scheme for measuring the coherent dynamics of a DBP^-. In our scheme, the excess electron's position within the 'left' or 'right' DB is discerned by an atomic force microscope (AFM) capacitively coupled to the pair. The AFM monitors the charge distribution in the presence of two other elements: a surface-parallel electrostatic bias applied along the two dangling bonds, and a tunable mid-infrared (MIR) laser field capable of driving the excess electron oscillation in the DBP^-.

When the MIR laser field is not resonant with the coherent electron tunneling of the DBP^-, the time-averaged charge distribution in the pair is asymmetric as imposed by the applied bias. However, as the laser becomes resonant, the theory predicts that the time-averaged charge distribution becomes symmetric; see Fig. 1.3(b). This resonant symmetry effect reveals the tunneling rate as well as the nature and rate of decoherence of the DB excess electron dynamics.

Despite the fact that an atomic force microscope (AFM) has single-electron resolution [46, 49], considering the fast DBP^- charge dynamics, the AFM measurement is relatively slow to directly realize the DB charge oscillation. In fact, AFM averages over many oscillations thereby losing all direct information about the excess-charge tunneling rate and decoherence. Nonetheless, during such a measurement, the DBP^- induces a shift in the AFM oscillation frequency, which is otherwise harmonic in the absence of capacitive coupling to localized charges [50]. The strength of this coupling reveals the time-averaged charge in the left and right DBs.

In general, it is possible to apply electrostatic biases by using lithographic contacts in order to locally address single atoms and molecules [16, 32, 51]. Such contacts can be used to establish an electric field along the two DBs in a DBP^-. This bias will cause the probability

distribution for the position of an excess electron to be more heavily weighted in the left or right DB depending on the sign and strength of the bias. In our scheme it is exactly this distribution that is observable by AFM. Furthermore, the actual tunneling rate is influenced by this static bias. For zero bias, the position of the excess electron is equally probable in the right and left DB; see Fig. 1.3(b).

In order to experimentally determine the tunneling rate and decoherence, we also need an oscillatory driving force pushing the excess electron back and forth rapidly between the two DBs at a rate comparable to the native tunneling frequency of the DB excess electron. In the case of two DBs, the driving field needs to be in the mid-infrared (MIR) regime. If the MIR field is off-resonant with the inter-dot tunneling frequency, the resultant force has only a small perturbative effect on the DB system so that the excess electron distribution is nearly the same as that without a driving field. If the MIR field is resonant, it can be theoretically shown that its field causes the electron to be equally probable at either DB. This effect can be measured experimentally by AFM and the data provided can be used to reveal the DBP^- tunneling rate and some properties and parameters of decoherence.

1.6 Overview of chapters

This chapter briefly explained the objectives pursued in the course of my PhD studies. The next two chapters cover the background information required for modeling and characterizing our DBP^- system. The following three chapters each contain the detailed description of each objective.

Chapter 2 contains background information about some electronic and structural properties of the Si crystal with the surface of interest, various types of charge qubit and their type of characterization, and models and methods employed for characterizing DBP^- dynamics. Chapter 3 covers background on the tools required for our proposed scheme in order to experimentally characterize the coherence of a DBP^-. This chapter also contains the details

about DFT and TDDFT methods used for calculating the tunneling rate of different DBP^- configurations.

Chapter 4 explains characterization of DBP^- coherent dynamics in full detail. Chapter 5 contains the results of *ab initio* calculations on the tunneling rate of different DBP^- configurations. Chapter 6 describes in detail our proposed scheme for measuring the coherent dynamics of a DBP^-. Chapter 7 summarizes the main conclusions of my thesis. In that chapter, I also suggest some new directions and future work that can be undertaken following my research project.

Chapter 2

Background for System and Methods

In this chapter, some background information is given about the system of interest and methods used for characterizing it. The chapter begins with a brief introduction on the silicon surface of interest, dangling bond, and charge qubit. Then, it continues with a short description of the extended Hubbard model, spin-boson model, and WKB approximation as the methods used for the characterization of coupled dangling-bond pairs.

2.1 Hydrogen-terminated Si(100)–2×1 surface

This section describes the structure and the nomenclature of the H-Si(100)-2×1 surface. A silicon (Si) crystal can be built by repeatedly putting together a unit cell[1] that has diamond-cubic structure with a lattice spacing of $a_0 \approx 5.43$ Å. The diamond-cubic structure is made of two merged face-centered cubics that are offset by 1/4 of the lattice constant in the x, y, and z directions. Each Si atom in the crystal shares the sp^3-type bond with its four nearest neighbors.

The surface plane of a crystal is defined by Miller indices with notation (hkl). These indices are determined by first finding the intercept of the desired surface plane with the three basis axes (xyz) in terms of the lattice constant and then taking the reciprocal of these values and reducing them to the smallest three integers that share the same ratio. Based on this notation, the indices '(100)' in Si(100)–2×1 indicate that the surface plane of interest is parallel to the yz-plane and has an intercept with the x-axis at one lattice constant. The three common surface planes of silicon crystals are Si(100), Si(110), and Si(111). The crystal orientations (100) and (111) are the most commonly used Si surfaces in the industry [52].

[1] A unit cell is a fundamental unit, made of one or more atoms, from which the whole crystal can be generated by putting copies of this cell together.

Atoms on a crystal surface can form different structures than those in the substrate. During surface reconstruction, surface atoms rearrange themselves and bond together so as to reduce the number of dangling bonds and to lower the free energy of the surface. The type of reconstruction depends on the material and the direction of the surface plane, as well as the environmental conditions, such as temperature and pressure, applied to the system. In general, two types of reconstruction can occur: conservative and non-conservative. In the former, all the original atoms remain at the surface while in the later some of the surface atoms will be missing after reconstruction.

A reconstructed surface is usually named by Wood's notation [53] given by X(hkl) ($m \times n$)–Rϕ, which uses the ratio of the lengths of the primitive translation vectors[2] of the top layer(s) 'm', to the primitive translation vectors of the underlying substrate 'n' and, if applicable, the angle to the underlying substrate 'ϕ'. In this notation,'X' denotes the type of atoms on the crystal surface and (hkl) is the Miller indices introduced above. As a simple example, Fig. 2.1 shows a 2×1 reconstructed surface.

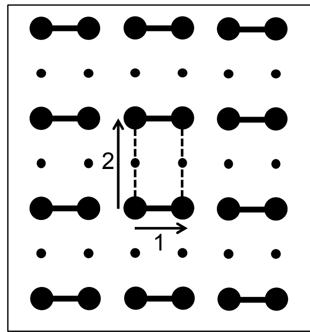

Figure 2.1: Woods notation for 2×1 reconstructed surface. Large circles are atoms on the surface plane and small circles are atoms in the underlying substrate. The short horizontal lines connecting the large circles represent surface-atoms dimer bonds. Three rows of surface atom pairs can be seen in this picture.

The Si(100) should ideally be a 1×1 surface, where the surface atoms are equally spaced in both directions. However, the Si(100) surface reconstructs into a 2×1 arrangement so that

[2]A primitive translation vector is the length and direction that the unit cell can be moved to still build the structure.

pairs of Si-atoms forms rows; see Fig. 2.1. In fact, by this DB-pairing the surface energy is lowered due to the reduction of dangling bonds. As a result, the surface atoms pair together and thus have two bonds to the underlying layer, one between the pairing neighbors and one unsaturated bond pointing out of the surface.

A clean Si(100)–2×1 surface is highly reactive, as each Si atom on the surface contains an unsaturated bond. A common way to passivate such a surface is achieved by allowing hydrogen atoms to react with the clean silicon surface in an ultrahigh vacuum chamber. The H atoms are provided by cracking HF gas or H_2 gas by means of a hot tungsten filament [54].

Ab initio calculations and experimental observations reveal that the Si-Si dimer bond is $R_{\text{Si-Si}} \sim 2.25$ Å, the Si-H bond is $R_{\text{Si-H}} \sim 1.509$ Å, the distance between adjacent dimers is $R_{\text{dimer}} \sim 3.84$ Å, and the distance between adjacent rows is $R_{\text{Row}} \sim 7.68$ Å, which is $\sim \sqrt{2} \times 5.431$ Å with 5.431 Å the unit cell length in Si [24].

Analogous to an atom having infinitely many energy levels, a semiconductor also has an infinite number of allowed bands. However, usually only those bands closest to the Fermi-level are most interesting as they have applications in electronics and optoelectonics. The Fermi level is located within the bandgap, which is a gap where the crystal's energy bands can not exist. The nearest energy bands above and below this bandgap are known as crystal conduction and valence bands, respectively. The energy bandgap of a semiconductor can be influenced by some phenomena such as temperature, pressure, and presence of impurities. At room temperature, i.e. 300 K, the energy bandgap of Si crystalline is 1.12 eV.

For a non-doped Si crystal, the Fermi level is located in the middle of the bandgap. However, when impurities are introduced to the system, the Fermi level shifts up or down so to preserve the neutrality of the crystal. In an n-type doped crystal the Fermi level gets closer to the conduction band as the donor provides an extra electron to the system. Similarly, for the p-type case the Fermi level lies nearer to the valence band. In general, the value of the absorption coefficient in the infrared range depends strongly on the doping level and can

become greater than 2000 cm^{-1} for donor concentrations above 10^{19} cm^{-3} [55].

2.2 Bulk and surface phonon modes of Si crystal

This section aims to introduce phonons and its different types in the bulk and surface of a semiconductor crystal, which is required for understanding the effect of phonon modes on the dynamics of a desired system. Considering a piece of crystal as a three-dimensional lattice of connected atoms, displacement of any number of atoms from their equilibrium positions leads to a set of vibration waves that propagate throughout the lattice. A phonon is a quanta of lattice vibrational motion (analogous to photon being the quanta of electromagnetic radiation), for which atoms in the lattice uniformly oscillate with a specific frequency. Any arbitrary lattice vibration can be written as a superposition of these primary phonons.

Similar to bulk phonons, a surface phonon is a quanta of lattice vibration on a crystal surface. Surface phonons can be either due to real surface vibration or it can be a consequence of bulk vibrations at the presence of a surface [56]. In both cases (i.e. bulk and surface), the nature of phonon modes depends on the structure of the crystal. Phonons play an important role in the determination of electronical, thermochemical and optical properties of condensed matter systems. For instance, understanding surface phonons provides useful information about the presence, quantity and type of defects existing on a crystal surface [57].

At non-zero temperatures, a lattice behaves as a collection of oscillators. Dynamics of atomic displacements, and consequently the energy of phonons generated in the lattice can be described by a harmonic approximation, such that the force exerted on each atom is proportional to the atom displacement with respect to its nearest neighbors. The force is characterized by a harmonic potential that depends on the atoms' separation distance. However, this assumption is valid only if the atoms remain close to their equilibrium positions.

The simplest model of a crystal lattice that leads to deriving information about the phonon modes of such system is a one-dimensional harmonic chain consisting of N identical

atoms that are connected with each other via springs that have a particular spring constant. The Hamiltonian for such model is the sum of atoms kinetic energy and springs potential energy and is given by

$$\hat{H} = \sum_{i=1}^{N} \frac{\hat{P}_i^2}{2m} + \frac{1}{2} m\omega^2 \sum_{\langle ij \rangle} (\hat{x}_i - \hat{x}_j)^2 \tag{2.1}$$

where m is the mass of each atom (assuming that all atoms in the system are identical), and P_i and x_i are the momentum and position operators of the i$^{\text{th}}$ atom. Also, $\langle ij \rangle$ denotes nearest neighbors of each atom.

This model can be generalized to 2 and 3 dimensions by replacing the momentum and position with their corresponding vectors having 2 or 3 coordinates. However, as we go to higher dimensions the polarization of phonons comes into play as well. As we go to 2 or 3 dimensions, propagation of vibrational modes is no longer restricted to one direction, while in one dimension phonons corresponds only to longitudinal waves.

Solving the equations of motion for such a system, one obtains a formula showing the relationship between angular frequency and wavenumber of phonon modes. This relation is called the "dispersion relation". The type of phonons can be characterized by this relation between phonon frequency and its wavenumber.

Two well-known types of phonons for which the energy can be described by the dispersion relation are acoustic phonons and optical phonons. In the acoustic type of phonons, the atoms' displacements are in-phase with each other, meaning that they all move in the same direction. Acoustic phonons correspond to lattice vibrations that have a wavelength much longer than the lattice constant so that the phonon wave behaves like a sound wave.

If the wavelength of acoustic phonon is very large as compared to lattice constant, this lattice movement corresponds to a displacement of the whole crystal. For long wavelengths, the dispersion curve for acoustic phonons show a linear relation between the phonon wavevector and its frequency, which is similar to the case of sound waves. As a consequence, acoustic phonons with long wavelengths can propagate a long distance through a crystal without

falling apart.

Optical phonons corresponds to lattice vibrations for which atom movements are out of phase, such that the neighboring atoms are moving in opposite direction of each other. They are called optical because this type of phonon modes are responsible for optical behavior of the lattice, for instance they can be excited by an infrared field [58]. In the long wavelength limit, optical modes interact with electromagnetic radiation. Optical phonons have high frequencies whereas acoustic phonons have low frequencies.

Depending on the direction of the atomic displacements in a phonon mode, the modes are either labeled as longitudinal or transverse. If the atomic displacement is in the direction of the wave propagation such that contraction and relaxation happens in the lattice, the phonon is named a longitudinal phonon. If the atomic displacement is perpendicular to the direction of propagation such that atoms vibrate side-to-side, the phonon is a transverse mode. Transverse phonon modes usually have smaller frequencies than the longitudinal ones [58].

Phonons have an important role in describing some of the characteristics of solid systems. Employing a suitable statistical model is one way to deal with the role of phonons in a system. For studying some of the electrical and thermodynamical properties of solid systems, especially those properties related to the system temperature (such as specific heat, thermal and electrical conductivity, and superconductivity) one must incorporate the role of the phonons of the system.

Phonons are boson-type particles, so they are indistinguishable and there is no limit on the number of phonon particles that can occupy an energy state. The collection of phonons in a given energy state is given by its density of states. Phonons obey Bose-Einstein distribution function which states that, in thermal equilibrium, the probability of finding phonons with a chosen angular frequency in a desired state is given by

$$n(\omega_{k,s}) = \left(\exp \hbar\omega_{k,s}/k_B T - 1\right)^{-1}, \tag{2.2}$$

where $\omega_{k,s}$ is the angular frequency of a phonon with wavenumber k and polarization s, K_B is the Boltzmann constant and T is the temperature of the system. In fact, $n(\omega_{k,s})$ is the mean occupation number of phonons at temperature T. The product of the phonon density of states and Bose-Einstein distribution function gives the number of phonons occupied states per unit volume at a given energy.

The scattering mechanism is a common approach for studying phonons of a system experimentally. This mechanism works based on inelastic scattering of photons or particles from the system where the resulting change of energy in the scattered particles provides information about phonons. Raman and X-ray scattering are two types of scattering mechanisms. The former is used for the study of optical phonons and the latter is employed for acoustic phonons.

Experimental studies of silicon phonon modes at room temperature show that the phonons have frequencies within the range of 50 GHz to 15 THz. More specifically, longitudinal acoustic phonons frequency were found to be within the range of 50-100 GHz [59]. In another experiment the optical phonon mode was reported to have a frequency of 15 THz [60]. On the other hand silicon surface vibrational modes of H-Si bonds were reported to be in the interval from 526 to 1111 cm^{-1} [61, 62].

2.3 Dangling bonds on the silicon surface

In this section, structural and electronic properties of dangling bond are explained in more detail and its applications in different systems are discussed. A dangling bond is an unsatisfied valence bond located on the surface of semiconductors or their interfaces; a DB is capable of accepting an excess charge or undergoing in a chemical reaction. The existence of DBs can be a consequence of surface imperfections due to missing atoms from the surface, or it can be the result of removing atoms by a physical or chemical process. Dangling bonds were first identified by Igor Tamm in 1932 [63, 64], and since then, it has been known and

studied as a defect in semiconductor devices. A common approach to reduce these defects is to expose hydrogen or oxygen atoms to the surface of the semiconductor.

The unique characteristic of the DB is its energy state which lies within the host semiconductor bandgap and so it is decoupled from the semiconductor conduction and valence bands. The DB energy state can either be discrete or may be continuous depending on the concentration of DBs on the host semiconductor [64]. High concentration of DBs pins the semiconductor Fermi level, and does not allow its energy bands to move freely under any applied bias, hence the reason for DBs to be considered as a defect. Oxidization or hydrogen passivation of the semiconductor surface shifts the DBs energy level out of the semiconductor bandgap and thus eliminates DBs electrical activity [65].

Dangling bonds usually have long lifetimes (from hours to days) depending on the level of cleanliness of their surrounding environment. Usually such surfaces are kept in an ultrahigh vacuum to prevent surface contamination with unwanted molecules/atoms. The reason for DB's long lifetime is its immobilized feature and the fact that most often a second adjacent DB is required for a molecule in order to bond to the surface [25]. Also, the strong bonding of DBs to their sites allows room-temperature experimental operations.

Generally speaking, the type and concentration of dopant atoms in a semiconductor, the density of DBs on the surface, local electric field and current applied directly to the DBs, all affect the charge state of a DB [66, 67]. More specifically, the location of the semiconductor Fermi level controls the DB charge state [68]. The Fermi level can be shifted up or down by changing the type and concentration of dopant in the semiconductor [24, 69].

For instance, high-levels of n-type doping in a semiconductor leads to high concentrations of electrons in the semiconductor. As a consequence, for a neutral DB (owning its inherit single electron) located on this semiconductor, the DB hosts a second electron with opposite spin (due to the Pauli exclusion principle) and thus becomes negatively charged. A negatively-charged DB exhibits a 0.5 eV upward shift of its energy level relative to that of a

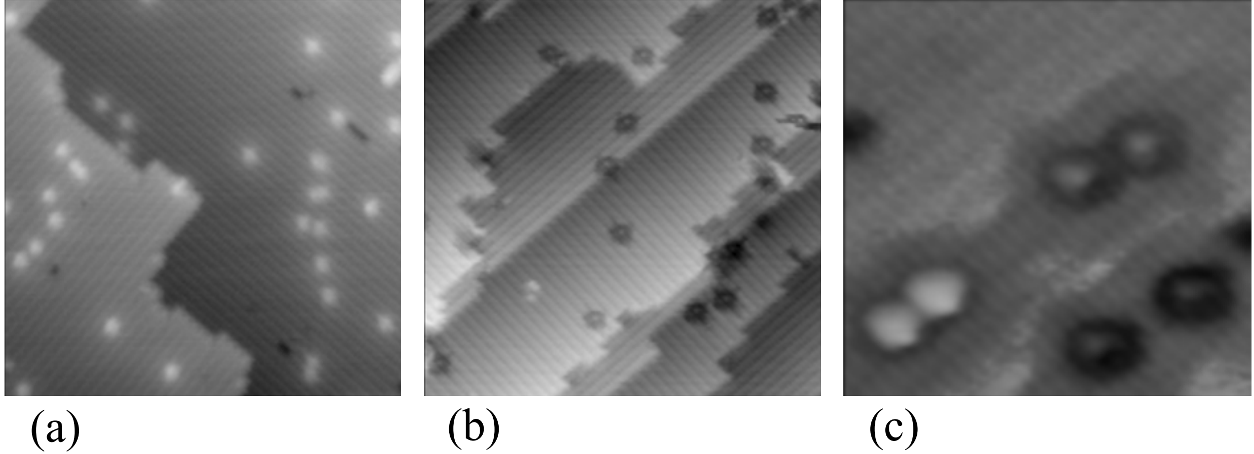

Figure 2.2: Scanning tunneling microscope images of dangling bonds on (a) a low-doped and (b) high-doped n-type Si(100)-2×1 surface. In low-doped crystals, dangling bonds appear as bright spots whereas in high-doped they appear as dark spots. (c) Three coupled-DB pairs where their image brightness depends on DBs separation in each pair. [reproduced from ref. [1], Fig. 1]

neutral DB Also, the silicon atom hosting a negatively-charged DB is elevated by 0.3 Å from the plane of the surface.

It has recently been shown that all three types of DB charging states (i.e. positive, neutral and negative charge states) are experimentally accessible as their energy states are well-separated from each other [70]. As mentioned above, specifying the level and type of doping is one way to control DB charge level. However, this type of control is passive because once it is set, there is no control over changing it. However, there are different ways to actively alter the charging level of a DB. The use of Schottky contacts [51], scanning tunneling microscope tip or any other type of probe tip, and the use of another charged DB are some examples of these approaches [71].

Scanning tunneling microscope (STM) imaging of DBs, located on a semiconductor with different level of doping, display differently; see Fig. 2.2. Low-level n-type doping causes DBs to be neutral, which is visible as white protrusions in STM imaging. On the other hand, in a high-doped n-type surface, STM imaging shows DBs as bumps surrounded by a dark region. In the case of coupled DBs, due to less local charge occupied by the coupled DBs,

they have a lighter appearance in the STM image. However, as the spacing between coupled DBs increases they look increasingly darker as the net charge approaches to two electrons per each DB.

Although DBs have been known as a defect for so many decades, recently new attempts have been taken towards finding possible applications of this entity in nanoscale technologies. With the progress made in fine-tuning control of nanotools such as the scanning tunneling microscope, it has become relatively easy to selectively create individual DBs on silicon surfaces and to pattern desired DB wires or clusters with an ensemble of DBs [51, 25]. This achievement has provided the opportunity to study the dynamics and electronic properties of DBs from a new perspective.

Ease and precise fabrication of DBs, plus having identical shapes, truly atomic-size, and the capability of hosting up to maximum 2 charges, all make DBs an excellent candidate for quantum dot [1] with the potential to be used for quantum computation. Furthermore, it was experimentally shown that DBs can control the type of chemical reactions occurring between organic molecules and a silicon surface [72, 73].

In another more recent experiment, it was demonstrated that DBs can be used as a truly atomic-scale bias-gate electrode to manipulate the charge distribution in coupled-DB clusters or a line of coupled cells served as DB-wire [1, 34, 24]. A linear chain of DBs will delocalize charge and allow biasing wires to be fabricated where needed. These applications of DBs implies that the high density ensembles of DBs enable passive components such as wires while widely spaced structures allow for the creation of the active elements in a circuit [25].

2.4 Solid-state qubit

This section discusses different types of qubits in solid-state systems and explains the methods used for characterizing coherent dynamics of such qubits. A qubit (or quantum bit) is the building block of quantum computation, and it is defined by the linear superposition of

two orthogonal states. Any candidate that is proposed for physical realization of a qubit must satisfy DiVincenzo's criteria [74]. Having a well-characterized qubit and long coherence time are two of these criteria, which are discussed in more detail in this section. The other DiVincenzo criteria are: the existence of a scalable system, ability to initialize the qubits in that system, having a universal set of quantum gates, and the capability to measure the qubit state.

Spin qubit and charge qubit are the two main types of candidates proposed for solid-state quantum computing. Different realizations of solid-state charge qubit can be categorized into two main groups of semiconductor [10, 11, 13, 22] and superconductor [6, 8] charge qubits. In the following, semiconductor charge and spin qubits are discussed followed by a brief discussion about superconductor charge qubit.

2.4.1 Semiconductor charge qubit

Semiconductor charge qubit is manifested, in general, as a coupled pair of quantum dots (QD) sharing a single electron. The electron bound between the two QDs can behave as a two-level system such that, in the position representation, the states of the system are defined by the electron position in the 'left' (L) or 'right' (R) quantum dot. We assume that the spin-degree of freedom of the electron is preserved and thus we only consider the charge position in the left or right QD.

This two-level system can be thought of as a double-well potential where the quantum states of the individual wells are given by $|\mathrm{L}\rangle$ and $|\mathrm{R}\rangle$, respectively [10, 11]. Approximating a two-level system by a double-well potential holds only if energy levels of each potential well are widely spaced so that only the ground states of each well are involved in the quantum superposition.

An alternative replacement for $|\mathrm{L}\rangle$ and $|\mathrm{R}\rangle$ states is the symmetric $|\psi_+\rangle$ and antisymmetric states $|\psi_-\rangle$, which are the eigenstates of the charge qubit Hamiltonian in the absence of any external field. In fact, the symmetric and antisymmetric qubit states correspond to

energy encoding, whereas the left and right states are used for position encoding. However, the left and right states are related to the symmetric and antisymmetric states according to

$$|\mathrm{L}\rangle = \frac{1}{\sqrt{2}}\left(|\psi_{+}\rangle - |\psi_{-}\rangle\right), \; |\mathrm{R}\rangle = \frac{1}{\sqrt{2}}\left(|\psi_{+}\rangle + |\psi_{-}\rangle\right). \tag{2.3}$$

The Hamiltonian for coherent dynamics of a charge qubit is given by

$$\hat{H}_0 = E_0\left(|\mathrm{L}\rangle\langle\mathrm{L}| + |\mathrm{R}\rangle\langle\mathrm{R}|\right) + \frac{\hbar\Delta}{2}\left(|\mathrm{R}\rangle\langle\mathrm{L}| + |\mathrm{L}\rangle\langle\mathrm{R}|\right), \tag{2.4}$$

where E_0 is the on-site energy of electron at each individual QD (considering that the two QDs are identical in shape) and Δ is the frequency (or rate) of the electron coherent tunneling between the two QDs. Diagonalizing the Hamiltonian $\hat{H}_0$ yields eigenenergies $E_0 \pm \hbar\Delta/2$ with corresponding eigenstates $|\psi_{\pm}\rangle$, respectively.

Qubit tunneling and decoherence are the two key components required for quantum computation. The qubit manipulation time should be a multiple factor of the qubit tunneling time, where the tunneling time is inversely proportional to its rate. Decoherence is a consequence of any unwanted coupling between the qubit and its surrounding environment, and manifests itself in two types of qubit-state relaxation and dephasing. Manipulation and measurement of charge qubit should be made before the charge dies out due to coupling with its surrounding environment.

The semiconductor charge qubit has been mainly realized based on two types of constituent, namely quantum dot and donor. The quantum dot (QD) is a small region in a semiconductor material where the motion of electrons is confined in all three spatial dimensions. The donor-type charge qubit is made of phosphorous atoms doped within a semiconductor [11, 22, 40, 75]. In both types of charge qubit, an excess electron is shared between two QD or P sites. In both cases, phonon modes and background charge fluctuations are known to be the two dominant sources of noise causing qubit decoherence [23, 47, 76].

Quantum dots are either self-assembled, or they are formed by spatial confinement of a region in a semiconductor by means of biased-gate electrodes [10, 23, 47, 77]. In the case

of electronically-confined-QD charge qubit, the dots are fabricated from a two-dimensional electron gas (2DEG) confined in either GaAs/AlGaAs [10, 47, 78, 79] or Si/SiGe [77] heterostructure. In fact, by putting together different types of semiconductor material, an edge is created in the band structure of the system; electrons can be confined in this edge and thereby forming a 2DEG. The number of electrons in the 2DEG is controlled by means of gate electrodes.

To experimentally characterize the dynamics of QD charge qubits, direct and indirect read-out schemes have been proposed. In direct read-out, the state of the qubit is measured by passing a current directly through the double QD, after applying an electric pulse for desired qubit manipulation. The qubit relaxation is controlled by the pulse period and its phase is controlled by tailoring the pulse shape [10, 23]. For indirect charge detection, a current-based quantum point contact (QPC) charge detector is employed. The QPC is located close to one of the QDs and the current passing through the QPC changes depending on the nearby QD being occupied or unoccupied (with the excess charge) [78, 79].

Another indirect technique proposed for characterizing the dynamics of a QD charge qubit is the photon-assisted tunneling (PAT) spectroscopy [47, 80, 81]. In this technique, the qubit state is driven by a microwave field and concomitantly is electronically biased; a QPC in close proximity to one of the quantum dots, detects the qubit dynamics by a continuous measurement of the photon-induced change in the charge-state occupancy of that QD. This method is different from the other methods in that it is based on a continuous measurement rather than a single-shot read-out. Thus, this technique is especially useful when the estimated coherent dynamics of the charge qubit is faster than the QPC-detecting resolution.

In the case of donor-type charge qubit, the qubit is comprised two shallow-doped phosphorous (P) atoms (in a semiconductor material such as silicon crystal) one of which is singly ionized. The outermost electron of the other P atom (that is not ionized) is shared between

the two P atoms resulting a P_2^+ (artificial) molecule [22, 40, 75, 76]. Phosphorous atoms are implanted within a silicon-on-insulator wafer [11]. The wafer is patterned and etched to form the desired electronic elements for the purpose of manipulation, control, and measurement of the qubit. The read-out is performed by means of single-electron transistor (SET) [11], which is a sensitive electrometer whose operation is based on qubit single-electron tunneling to a small island; the island is isolated from the qubit by two slightly-separated voltage-controlled electronic leads.

Both QD- and P-type charge qubits pose their own typical challenges. For instance, the dots in a double-QD charge qubit are never identical in shape. Furthermore, since the QDs are defined by the gate electrodes, charge fluctuation surrounding the gate electrodes have a significant influence on qubit coherent dynamics. On the other hand, while the constituents of P-type qubits are identical, there is the problem of precisely positioning P dopants in the host crystal. Furthermore, the tunnel coupling for this type of charge qubit is influenced by the Si crystal band structure. Thus, even keeping the separation between the two P atoms constant, qubit tunnelling rate can still vary over a wide range of values.

Experimental characterization of QD charge-qubit dynamics shows that maximum timescales obtained for qubit tunneling, relaxation, and dephasing are $\approx$ 0.5 nsec $\approx$ 10-18 nsec, and $\approx$ 60 ps-2 nsec, respectively [77, 78, 79]. For the case of P-type charge qubit, the latest experimental assessment gives a tunneling time of 10 psec and a relaxation time of 10 msec, but does not report on the dephasing time [40]. In an earlier experiment though, the tunneling, relaxation, and dephasing times are reported as 0.1 μsec, 100 μsec and 200 nsec, respectively [11].

In both cases, the tunneling time and worse-case decoherence time (which belongs to dephasing) are almost in the same order of magnitude, implying that these proposed qubits are not yet good enough for quantum computation. One rational approach to overcome this problem is to look for smaller-size quantum dots. In a recent experiment, a coupled

dangling-bond pair was proposed as a potential candidate for semiconductor charge qubit. However, characterization of the dangling-bond-pair coherent dynamics was left as an open question [1].

2.4.2 Semiconductor spin qubit

The spin qubit in semiconductors is realized in the form of electron spin and nuclear spin [9, 15]. The electron-spin qubit is usually a confined isolated electron in a gate-defined quantum dot [82]. The nuclear-spin qubit is manifested in the form of a neutral or ionized donor embedded in a host semiconductor material [9, 83]. In general, the qubit state in both cases is defined as a linear superposition of spin-up and -down of the electron or nuclei.

In 1998, Loss and DiVincenzo proposed using a single electron in a QD as spin qubit. In their proposal, electron spin was manipulated by controlling the potential barrier between quantum dots. They also suggested three different approaches for spin read-out, one of which is the well-known spin-to-charge conversion method. In this method, the spin qubit has a spin-dependent tunneling through a spin-valve into a third QD which then is measured by a charge-sensitive electrometer, such as a quantum point contact or a single electron transistor. The role of the spin-valve is to allow only one type of electron spin to pass into the third QD; thus the presence of a charge in the third QD is an indication of the spin of the qubit. Detecting charge occupancy and determining the type of spin is significantly easier than measuring the spin directly. This method has become a common approach for dealing with spin-qubit measurements [21].

The dominant source of decoherence for electron-spin qubit is determined to be qubit interactions with the host-material nuclear spin bath [84]. One way to overcome this problem is to use a host material with nuclei that are spinless. For instance ^{28}Si is an excellent host not only because it is spinless but also due to its wide application in the nanofabrication industry. In an alternative approach, it has been shown that a spin qubit made of a pair of electrons, each residing in a QD, is more robust against decoherence caused by nuclear

spins and also charge noises [85]. In this case, information is encoded in the superposition of electron-pair singlet/triplet states. Since these two states are spinless, they are unaffected by the nuclear spins.

Kane suggested using the nuclear spin of phosphorous donors embedded in a pure silicon crystal as spin qubit and proposed a quantum computing architecture, based on an array of individual ^{31}P atoms with nuclear spin of 1/2 [9] dopped in ^{28}Si material. In such a system, a large DC magnetic field is applied to create an energy splitting between spin-up and spin-down states and also to initialize the nuclear spin qubits in one of its states. Also, an AC magnetic field is applied to keep the nuclear spin oscillating between the up and down states at resonance and thus creates a linear superposition of them.

The spin qubits are then manipulated by electric gates located on the silicon surface above and between the spin qubits. The gates above the qubits control the resonance frequency of the nuclear spin and gates located between two nuclear spins control the electron-mediated coupling between the two nuclear spins. Electrons are used to mediate between nuclear-spin interactions and to facilitate nuclear spin measurement. The measurement is performed by first transferring the state of the phosphorous nuclear spin to the state of the corresponding electrons and then use the spin-to-charge conversion approach for read out.

In a recent experiment, a coherence time of ≈ 200 μsec has been observed for an electron-spin qubit in a GaAs quantum dot, which allows more than 1000 coherent quantum operations before the qubit decohers [86]. For the nuclear-spin qubit, a coherence time of 180 sec (at low temperature) has been reported [87]. It was recently shown that employing ionized donors rather than the neutral ones as nuclear-spin qubits help to dramatically increase the coherence time to 39 minutes, at room temperature [83]. In the same experiment, a coherence time of 3 hours was reported for the low-temperature condition.

Spin qubits, in general, are better isolated from the environment than charge qubits, consequently they have longer coherence times. On the other hand, a comparison between

the coherence of electron spin and nuclear spin shows that the nuclear spin has a much longer coherence than the electron spin. Furthermore, electron spin can be manipulated and also be coupled to other electron-spin qubits in a much shorter time-scale than the nuclear spin qubit. Therefore, the electron spin seems to be more suitable to be used as a quantum processor while the nuclear spin works better as a quantum memory for storing quantum information.

2.4.3 Superconductor charge qubit

The superconducting charge qubit [6, 8, 7] is realized by the superposition of zero and one Cooper pair in a nanometer-scale superconducting island, also known as Cooper-pair box. The island is connected via one or two Josephson junction(s) to the rest of the electronic circuit. The number of Cooper pairs tunneling across the junctions and the effective fields acting on the qubit are controlled by tuning the gate voltages in the circuit.

The architecture proposed for quantum computing with superconducting qubits involves embedding superconducting charge qubits in a one-dimensional transmission line resonator (i.e. a copper waveguide cavity) and coupling the lowest mode of the cavity with the qubit transition [88, 89]. This proposal enables coherent control, manipulation and readout of qubits. Recent achievements for coherence and decoherence rates of such qubits are in the order of $\approx 10^{-10}$ and $\approx 10^{-4}$sec, respectively [90, 91, 92]. The high quality factor of $\approx 10^{-6}$ makes the superconducting charge qubit a successful achievement towards quantum computation.

2.5 Extended Hubbard model

The Hubbard model is an approximate model used mostly in solid state and condensed matter physics for investigating the electronic and magnetic properties of interacting particles in a lattice [42, 93]. This model was originally proposed for fermions, but later it was applied

to bosonic systems as well [94]. The Hubbard model is originally composed of the on-site energy and Coulombic interaction of particles at any site of the lattice plus particles hopping between different lattice sites. If the long-range Coulombic interaction between particles at different sites are added to this model, then it is referred to as the "extended Hubbard model" [95]. In other words, the extended Hubbard model considers Coulombic interactions between the particles to be located in the nearest-neighbor lattice sites.

Dynamics of electrons, as fermionic particles, on a two-dimensional lattice can be described by a Hamiltonian $\hat{H}$ that acts upon the Hilbert space spanned by zero, one, or two electrons per each lattice site. The Hamiltonian of the extend Hubbard model can be expressed, in general, by:

$$\begin{aligned} \hat{H} &= \sum_{i,\sigma} E_{\mathrm{os}} \hat{n}_{i,\sigma} - \sum_{\substack{\langle i,j \rangle \\ \sigma}} T_{ij} (\hat{c}^{\dagger}_{i,\sigma} \hat{c}_{j,\sigma} + \hat{c}^{\dagger}_{j,\sigma} \hat{c}_{i,\sigma}) \\ &\quad + \sum_{i} U_i \hat{n}_{i,\uparrow} \hat{n}_{i,\downarrow} + \sum_{\langle i,j \rangle, \sigma, \sigma'} W_{i\sigma j\sigma'} \hat{n}_{i,\sigma} \hat{n}_{j,\sigma'}, \end{aligned} \tag{2.5}$$

where $\langle i,j \rangle$ indicates the nearest-neighbor interaction on the lattice sites i and j, and $\{\sigma, \sigma'\} \in \{\uparrow, \downarrow\}$ is the electron spin up and down. In addition, $\hat{c}^{\dagger}_{i,\sigma}$, $\hat{c}_{i,\sigma}$, and $\hat{n}_{i,\sigma}$ are the creation, annihilation, and number operators, respectively, acting on electrons with spin σ at lattice-site i.

The parameter E_{os} is the on-site energy of the electron at any site. The hopping (or tunneling) between sites i and j is given by T_{ij}, which depends on the separation distance between the two sites i and j. The on-site Coulombic interaction U_i denotes the energy cost of putting two electrons of opposite spin at the same site i. The inter-site Coulombic effect denoted by $W_{i\sigma j\sigma'}$ is the cost of putting one electron with spin σ at site i concomitantly with putting another electron of spin σ' at site j.

Depending on the level of electron filling in a lattice, and the strength and comparability of the terms in the Hamiltonian, which is manifested in the coefficient incorporated in each term, the extended Hubbard model is capable of describing a wide range of physical phe-

nomena. The strength of the coefficients in the Hamiltonian determines whether electrons have the tendency to be localized in the lattice sites or to be delocalized, which leads to better understanding of electronic or magnetic characteristics of a system. For example, the extended Hubbard model has been used for modeling high-temperature superconductivity [96, 97], and for identifying phase diagram [97, 98]. It has also been used for modeling trapped ions or atoms with fermion-type spin in optical lattices [96].

2.6 Spin–boson model

In this section we consider the spin-boson model which is a common model for studying environmentally induced decoherence for semiconductor qubits [38, 39]. The spin-boson model is a well-established simplified model for characterizing weak coupling between a two-level system, e.g. charge qubit, interacting with a bosonic bath of harmonic oscillators, such as phonons or charge fluctuations.

One of the simplifying features of the spin-boson model is that in the limit of weak coupling, the relaxation rate of the system (due to its population decay) and its decoherence rate (due to its coherence decay) are equal to second order in the coupling [38], which allows us to characterize the system by a single decoherence rate. This model has been used, for instance, in the estimation of decoherence rate for the P-P$^+$ charge qubit in bulk silicon [13]

The spin-boson model is described by a Hamiltonian given by [38]

$$\hat{H}_{\mathrm{sb}} = \sum_i \hbar\omega_i \hat{b}_i^\dagger \hat{b}_i + \hat{\sigma}_z \sum_i \lambda_i \left(\hat{b}_i^\dagger + \hat{b}_i\right) \tag{2.6}$$

where ω_i is the frequency of the bath i^{th} harmonic oscillator mode, $\hat{b}_i^\dagger$ and $\hat{b}_i$ are the corresponding creation and annihilation operators, and λ_i is the coupling strength between the two-level system and the ith mode of the bath.

The first term on the right-hand side of Eq. (6.28) is the bath free Hamiltonian, and the second term is the interaction Hamiltonian describing the system-bath coupling. The

interaction Hamiltonian can be rewritten as

$$\hat{H}_{\text{int}} = \hat{\sigma}_z \sum_i \lambda_i \left(\hat{b}_i^\dagger + \hat{b}_i\right) = \hat{\sigma}_z d \sum_i c_i \hat{x}_i, \tag{2.7}$$

with d being the distance between the two localized states of the system, $\hat{x}_i$ being the spatial coordinate of mode i, and c_i being the coupling strength between the system and mode i. Equation 2.7 clearly shows that the system-bath coupling depends linearly on the coordinates of the system and those of the bath harmonic-oscillator modes.

Studies show that, for any system characterized by the equilibrium statistical average over the initial and final states of the bath, the only physically relevant quantity in the spin-boson model is the spectral density function of the bath [38]

$$J(\omega) = \frac{\pi}{2} \sum_i \delta(\omega - \omega_i) \frac{c_i^2}{m_i \omega_i}. \tag{2.8}$$

A large class of open systems, i.e. systems interacting with their surrounding environment, can be characterized by a spectral density of the form

$$J(\omega) = \alpha \omega^s \exp(-\omega/\omega_{\text{c}}) \tag{2.9}$$

for ω_{c} being a cutoff frequency and α and s being empirically-fitted constants. For $s = 1$, the bath is said to be ohmic. The spin-boson model, although is known as a simple dissipative model, does not have a general analytic solution. The next step of assessing a system by this model depends on the ratio between the coherence rate of the system Δ, parameters ω_{c}, and $k\Theta$, where k is the Boltzmann constant and Θ is the temperature.

In a practical level, the most common solution for this model is the perturbative ones in which the weakest term in the total Hamiltonian plays the role of the perturbation. For example, in the adiabatic limit, where $\Delta \gg \omega_{\text{c}}$, the bath evolves quite slowly and has an almost classical behavior, whereas in the non-adiabatic limit, $\Delta \approx \omega_{\text{c}}$, the golden rule offers a reliable solution. There are also other limiting cases where $k\Theta$ and other energy scales are involved and are well understood [99, 100], but these are beyond the scope of our interest.

2.7 Wentzel–Kramers–Brillouin approximation

The aim of this section is to provide the WKB approximation that is used to estimate the tunneling rate in different systems such as electron tunneling in charge qubit systems and STM-sample tunneling current. The WKB approximation was first developed by Wentzel, Kramers and Brillouin (hence the acronym WKB) in 1926 [101, 102]. This approximation gives a semiclassical treatment of the Schrödinger equation associated with a particle moving towards a potential barrier $V(x)$ with an arbitrary (but slowly varying) shape. To apply this method one requires the shape of the potential barrier and the energy of the particle E (i.e. whether E is smaller or larger than $V(x)$) in order to calculate the particle wavefunction and its tunneling through the potential barrier.

Assuming that a potential barrier has a width of $x_1 < w < x_2$, based on WKB approximation, tunneling of a particle through the potential barrier can be estimated by calculating the probability densities of the particle wavefunction on the emerging side and the incident side of the barrier and then finding the ratio between them, i.e.

$$|T|^2 = \frac{|\psi(x_2)|^2}{|\psi_0|^2} = \exp\left(-2\int_{x_1}^{x_2} |k(x')|\mathrm{d}x'\right). \tag{2.10}$$

The parameter $k'(x) = \sqrt{\frac{2m(E-V(x))}{\hbar^2}}$ is the particle wavenumber. Equation (2.10) holds if the derivative of the wavenumber is much smaller than the wavenumber itself, i.e.

$$\left|\frac{\mathrm{d}k'(x)}{\mathrm{d}x}\right| \ll k'^2. \tag{2.11}$$

This condition implies that the particle wavelength λ (where $\lambda \propto k^{-1}$) must be much smaller than the variation of $k(x)$ (and consequently the variation of $V(x)$) with respect to x.

In cases where the energy of the particle is larger than the barrier height $E > V(x)$, the wavenumber is real, the probability density remains constant, i.e. $|\psi(x)|^2 = |\psi_0|^2$, the system can be treated classically. However, for the cases where the particle is passing through the potential barrier $E < V(x)$, the wavenumber becomes imaginary and should be treated quantum mechanically.

2.8 Conclusion

In this chapter, I established some of the basic frameworks that are required in order to understand the new results in chapters 4 and 6. This chapter includes the background material about the system of interest plus the methods used for theoretical modeling of the coherent dynamics of our system. The next chapter also covers the rest of the basic knowledge essential for employing in the study of our system of interest, i.e. a coupled DB pair on the Si(100)-2$\times$1 surface.

Chapter 3

Background on the Experimental Tools and *Ab Initio* Techniques for DBP$^-$ Characterization

In this chapter, I present the relevant background material behind the experimental tools and the *ab initio* techniques employed for characterizing coherent dynamics of different DBP$^-$ configurations. The experimental tools to be discussed are atomic force microscope, scanning tunneling microscope, mid-infrared laser field, and applied bias. These tools are used in our proposed scheme for characterizing DBP$^-$s tunneling rate and the nature and rate of decoherence, which is given in details in chapter 6.

Also, in this chapter, the basic concepts underlying *ab initio* density functional theory (DFT) and time-dependent DFT are explained and some of the features that lead to their widespread application as well as some of their failures in calculating properties of atomic and molecular systems are discussed. These *ab initio* methods are employed for calculating energy splitting of DBP$^-$s with different configurations and a variety of DB-pair separations. The results of these *ab initio* calculations are reported mainly in chapter 5.

3.1 Experimental tools for characterization of DBP$^-$ coherent dynamics

3.1.1 Frequency-mode atomic force microscope

Atomic force microscope is a very high-resolution nanotool which can achieve single-electron sensitivity [46, 49]. Recently, it has been used for detecting the electronic properties of individual and coupled quantum dots in contact with a reservoir [103, 104]. In the frequency-mode atomic force microscope, the AFM cantilever behaves as a simple harmonic oscillator

along the coordinate axis z perpendicular to the sample surface. The tip is driven by an externally controlled force $F_0 \sin \omega_0 t$, with F_0 being constant. When scanning a sample, the AFM tip experiences distance-dependent forces $F_{\mathrm{z}}(z)$ from its interaction with the sample.

In the limit of small oscillation amplitudes and small force gradients, the equation of motion for the AFM tip around its equilibrium position (chosen as the origin of the z-axis, at a height z_0 from the surface) is [105]

$$m\ddot{z} + \gamma\dot{z} + m\omega_0^2 z = F_0 \sin \omega_0 t + F_{\mathrm{z}}(z), \tag{3.1}$$

where γ is the AFM damping factor, m the mass of the probe and $k = m\omega_0^2$ the AFM probe spring constant.

In the same limit of small oscillation amplitudes (a few Å is anticipated), we can use a truncated Taylor expansion

$$F_{\mathrm{z}}(z) \simeq F_{\mathrm{z}}(0) + z \left.\frac{\partial F_{\mathrm{z}}}{\partial z}\right|_{z=0}, \tag{3.2}$$

with a resultant equation of motion for the tip,

$$m\ddot{z} + \gamma\dot{z} + m\omega^2 z \simeq F_0 \sin \omega_0 t + F_{\mathrm{z}}(0), \tag{3.3}$$

describing driven oscillations with a modified resonant frequency depending on the lateral tip position

$$\omega^2 = \omega_0^2 - \frac{1}{m}\left.\frac{\partial F_{\mathrm{z}}}{\partial z}\right|_{z=0}. \tag{3.4}$$

The right-hand side of Eq. (3.3) is a constant in space so the tip-sample force is detected by measuring the frequency response of the tip according to (3.4). Employing the binomial expansion on Eq. (3.4) yields the modified frequency expression

$$\Delta\omega := \omega - \omega_0 \simeq -\frac{\omega_0}{2k}\left.\frac{\partial F_{\mathrm{z}}}{\partial z}\right|_{z_0} \tag{3.5}$$

showing the proportionality between the frequency shift and the local force gradient.

Note that far from the limit of small amplitudes one can still approximate the AFM motion from the above equation, but instead of the force gradient at the equilibrium position, one should use an average force gradient over an entire oscillation range $[z_{\mathrm{min}}, z_{\mathrm{max}}]$, i.e.

$$\Delta\omega \simeq -\frac{\omega_0}{2k\left(z_{\mathrm{min}} - z_{\mathrm{max}}\right)} \int\limits_{z_{\mathrm{min}}}^{z_{\mathrm{max}}} \frac{\partial F_{\mathrm{z}}}{\partial z} \mathrm{d}z. \tag{3.6}$$

The experimental goal is then to measure these changes in the tip oscillation frequency thereby revealing information about the sample.

From Eq. (6.18), we see that the ratio ω_0/k gives the sensitivity of the cantilever, which in practice depends on the build geometry and material of the cantilever. Typical examples are silicon cantilevers with a sensitivity factor $\omega_0/k = 4000$ Hz m/N, and the qPlus tuning fork with $\omega_0/k = 20$ Hz m/N [50, 106, 107]. However, when choosing a cantilever for a given experiment, the sensitivity is not the only factor to consider, as scan stability (e.g. against jump-to-contact), quality factor, measurement bandwidth, and appropriate size of oscillation amplitudes also play important roles.

The minimum detectable signal of an AFM experimental setup is determined by assessing its frequency noise $\delta\left(\Delta\omega\right)$, i.e. the standard deviation of the frequency shift. Theoretically, $\delta\left(\Delta\omega\right)$ is given by [108, 109]

$$\delta\left(\Delta\omega\right) = \frac{2\pi}{A}\sqrt{\frac{\omega_0 B k_{\mathrm{B}} T}{2\pi^2 k Q} + \frac{n_q^2 B^3}{\pi^2} + \frac{n_q^2 B}{2Q^2}}, \tag{3.7}$$

where Q is the quality factor, A is the oscillation amplitude, B is the measurement bandwidth, $k_{\mathrm{B}}T$ is the thermal energy, and n_q is the deflection noise density. The first term on the right-hand side of Eq. (3.7) is the thermal noise of the AFM tip, the second term is the deflection-detector noise, and the third term is the noise of the instrumental setup. Thus, one should choose the experimental parameters such that the sensitivity and the signal-to-noise ratio of the AFM setup are optimized.

3.1.2 Scanning tunneling microscope

Scanning tunneling microscope (STM) is a tool capable of imaging conductive materials, such as metals and semiconductors, at the atomic level. It works based on current tunneling between a sharp conductive tip and the surface of the sample of interest. Most of the current is carried by the atom of the tip that is closest to the surface, which is the reason for STM atomic precision. The lateral resolution of STM is typically ≈ 0.1 nm and its depth resolution is ≈ 0.01nm [110]. With this resolution, STM is also capable of manipulating individual atoms or molecules on the surfaces and directing them to predetermined positions.

In scanning tunneling microscope, a sharp tip is held a few Ångstroms away from a sample. A small bias voltage is applied between the tip and the sample which results in tunneling current. The STM tip is typically made from tungsten and is mounted on a piezoelectric-crystal tube that allows positioning of the STM tip with subatomic precision in all three spatial directions [50]. Electronic properties of the sample of interest can be studied, by measuring the changes in current, bias voltage, the tip-surface separation distance, or the derivative of one with respect to the other.

The STM tip-sample tunneling current is given by [111]

$$I_t(z) = I_0 \exp\left(-2k_t z\right) \tag{3.8}$$

where I_0 is a function of the applied bias and a function of the density of states in both the tip and the sample. $k_t = \sqrt{2m\Phi_t/\hbar}$ where Φ_t is the average workfunction of the tip and the sample. The potential-barrier height between the tip and the sample is roughly approximated by the average workfunction of the sample and the tip. Since the tunneling current is exponentially proportional to the tip-sample distance, the current drops by an order of magnitude if z is displaced by 1 Å. The typical current in STM is in the order of $I_t \approx 100$ pA [50]

Scanning tunneling microscope can operate in constant current mode and constant height mode. In the former, while the current is kept constant, the tip's height changes as the tip

scans through the surface; thus the resultant image is from the tip topography of the sample and the image is showing the charge density of the surface of the sample. In the latter, the height and the voltage of the tip are both kept constant and thus the current varies as the tip is swept through the surface [111]. The scanning is much faster in the height mode than in the current mode, as the piezoelectric-scanning tube needs more time to adjust with the height change than with the current change [112].

In addition to topographic (real-space) imaging, STM can be used for spectroscopic purposes to obtain information about the electronic structure of the density of state in a chosen sample. For instance, the electronic structure at a desired location on a sample can be obtained by sweeping voltage and measuring current at that location [110].

The noise in the STM current measurement is related to the STM vertical noise δz. The vertical noise is described by the root-mean-square deviation of the mean value and for STM is given by

$$\delta z \approx \frac{\sqrt{4k_B T B/R}}{2k_t|I_t|} \tag{3.9}$$

where k_B is the Boltzmann constant, B is the measurement bandwidth, T is the temperature and R is the resistance in the feedback loop. For the STM imaging to work properly, the vertical noise of the tip should be smaller than the atomic corrugation of the sample.

Besides the benefits, STM faces some challenges and limitations. For instance, application of STM is limited to conductive materials and thin non-conductive films deposited on conductive substrates, in order to allow current tunneling between the STM biased tip and the sample. Also, the surface of the sample should be clean and stable. Furthermore, although STM has atomic spatial resolution, its temporal resolution is typically on the order of seconds. Therefore, STM is unable to image fast dynamics of the chemical processes on a sample.

3.1.3 Electric-field biasing and space-charge layer

The energy levels of a semiconductor can be altered by applying an external electric field. The applied field can be due to a metallic contact to the semiconductor surface, or a probe close to the surface, or even can be due to a charged surface state. A typical approach to treat the electric field effect on a semiconductor is the use of band-bending diagram.

The band-bending diagram represents energy of a semiconductor's band edges with respect to the depth into the material. When applying a voltage bias to a semiconductor, its conduction- and valence-band edges bend upward or downward depending on the sign of the applied bias. The amount of bending is determined by the difference between the work function of the bias gate and the semiconductor [113].

When a metallic bias electrode is brought close to a semiconductor or gets in contact with it, due to the low concentration of free charges in the semiconductor as compared to the bias, the free charges of the semiconductor get depleted or accumulated near the semiconductor surface. The depletion or accumulation of the charge depends on the sign (i.e. positive or negative) of the applied bias and results into a region called the space-charge layer [113]. In this region, the semiconductor energy bands are bent due to the applied electric field or due to the charge transfer caused by the field.

In the case where a metallic bias gate is in contact with a semiconductor, the free electrons will flow between the metal and the semiconductor until their Fermi levels are aligned. An example of nanoscale metallic contact is the titanium silicide (TiSi2) islands, which are patterned by optical lithography on Si(100) and Si(111) surfaces [51, 114]. This metallic contact causes upward band bending in the region surrounding the island. The band bending was detected by the shift observed in I-V spectra of the STM measurement. Since the resulted band bending leads to depletion of electrons in the region close to the island, TiSi2 contact can be used for controlling and alternating the charging state of the DBs created on the silicon surface. The depth and length of the depletion region can be varied by applying a

voltage bias to these metallic islands.

Another way to alter the energy bands of a semiconductor is to bring an STM or AFM tip close to the surface. When a voltage is applied between the STM/AFM tip and the semiconductor, it generates an electric field between them which results in the band bending of the semiconductor energy levels. Recently, it was experimentally shown that the charge state of individual DBs is controlled by STM tip where the control relies on the tip-induced band bending [70, 115]. Scanning tunneling microscope has not only been used as a tool to apply a bias to a semiconductor, but also as a means to measure the semiconductor band bending [113].

Negatively-charged dangling bonds can also lead to band bending and thus can play the role of a bias gate. In an experiment, it was shown that a negative DB located close to a string of identical molecules shifted their energy levels, while the amount of shift was a function of each molecule's distance from the DB [25, 116]. Due to their atomic size, dangling bonds have the potential for electrostatically addressing atomic structures that are too small to be addressed by any conventional biasing tools. It was recently proposed to use DB ultra-fine wires extended from TiSi2 contacts for precise control of atomic structures [25].

3.1.4 Mid-infrared field

Mid-infrared (MIR) sources have a wide range of varieties [117]. They have wavelengths ranging from $\approx 3 - 30$ μm (i.e. 300–3000 cm^{-1} / 0.4–0.04 eV / 10–100 THz). Mid-infrared sources cover the vibrational transition of many molecules and species and have a wide application in science, such as spectroscopy, chemical and bimolecular sensing, and material processing. Among tunable continuous wave (CW) mid-infrared sources, solid-state lasers and CO_2 lasers are the two examples of interest [118].

Semiconductor lasers and quantum-cascade lasers are two types of solid-state MIR sources. Semiconductor lasers operate in a wavelength range of $\approx 3 - 30$ μm. The field can be tuned anywhere between 100 cm^{-1} (for coarse tuning) to 1–2 cm^{-1} (for fine tuning). This type of

MIR lasers operates with an output power in the range of $0.1 - 0.5$ mW. Two drawbacks of such lasers are: (1) large beam divergence and (2) the requirement for cryogenic cooling, which imposes limitation on laser performance.

Quantum cascade lasers work based on inter sub-band transitions within a multiple-quantum-well structure [117, 119]. This type of MIR source emits in wavelengths ranging from 3–25 μm, but it can have single-frequency operation within the range of 4.3–24 μm, so it can operate either in CW mode or pulsed mode. The linewidth of CW quantum cascade lasers ranges from a few MHz to a few KHz, but for pulse operation it exceeds 150 MHz (HWHM). Quantum cascade lasers have a fine tuning of 3 cm^{-1} and a coarse tuning of 35 cm^{-1} and can operate with a power within the range of 1–100 mW. Similar to the case of semiconductor lasers, quantum cascade fields suffer from producing large amount of heat and having a large beam divergence.

Another type of MIR source is the carbon-dioxide laser. The gas-type CO_2 source has a continuous-wave field and can generate light with a wavelength within the domain of $\approx 9 - 11$ μm. Carbon-dioxide lasers have the ability for fine tuning of 1 cm^{-1} (i.e. 30 GHz) and operates with a power ranging from mW to hundreds of kW. Due to its wide range of power, this type of MIR source has a wide application in research, industry and military.

3.2 Density-Functional Theory

An unperturbed multi-particle system such as a piece of Si crystal can be characterized by solving its time-independent Schrödinger equation

$$\hat{H}\psi\left(\boldsymbol{x}_1, \boldsymbol{x}_2, \cdots\right) = E\psi\left(\boldsymbol{x}_1, \boldsymbol{x}_2, \cdots\right), \tag{3.10}$$

where $\hat{H}$ is the Hamiltonian of the system and $\psi\left(\boldsymbol{x}_1, \boldsymbol{x}_2, \cdots\right)$ is the wavefunction containing information about the spatial and the spin coordinates of the particles in the system. For a piece of Si crystal having M nuclei and N interacting electrons the Hamiltonian is composed of the kinetic energy of the electrons $\hat{T}_{\mathrm{e}}$ and the nuclei $\hat{T}_{\mathrm{n}}$, the attractive electron-nuclei

potential energy $\hat{V}_{\mathrm{ne}}$, and the repulsive electron-electron $\hat{V}_{\mathrm{ee}}$ and nucleus-nucleus interactions $\hat{V}_{\mathrm{nn}}$.

Assuming that the nuclei are spinless, the wavefunction depends on $4N + 3M$ variables, which is a considerably large number. Therefore, solving the Schrödinger equation is a big challenge as it requires a large amount of resources. The Schrödinger equation can be greatly simplified using the Born-Oppenheimer approximation, which assumes that nuclei are fixed in place as they are ≈ 1800 times heavier than electrons. Consequently, the nuclei kinetic energy in the Hamiltonian can be set to zero and the nucleus repulsive potential is almost a constant. Thus, the Hamiltonian reduces to the so-called electronic Hamiltonian, given by

$$\begin{aligned}\hat{H}_{\mathrm{elec}} =& \hat{T}_{\mathrm{e}} + \hat{V}_{\mathrm{ee}} + \hat{V}_{\mathrm{ne}} \\ =& -\frac{\hbar^2}{2m_{\mathrm{e}}}\sum_{i=1}^{N}\boldsymbol{\nabla}_i^2 + \frac{1}{2}\sum_{i,j=1}^{N}\frac{e^2}{|\boldsymbol{r}_i - \boldsymbol{r}_j|} - \sum_{i=1,I=1}^{N,M}\frac{Z_I e^2}{|\boldsymbol{r}_i - \boldsymbol{R}_I|},\end{aligned} \tag{3.11}$$

where m_{e} is the electron mass and Z_I is the atomic number. The number of variables is reduced to $4N$, however this number is still large enough to make solving the Schrödinger equation impractical.

Density functional theory provides an alternative approach for solving the Schrödinger equation. Density functional technique is a powerful technique that is built upon the Hohenberg-Kohn theorem [43]. This theorem states that the dynamics of a multi-particle system can be formulated in terms of its ground-state electron density rather than the coordinates of its electrons. Based on this theorem, there is a one-to-one correspondence between the potential energy of a system and its ground-state electron density.

As a result of this theorem, the value of any physical observable in a system is a unique functional[1] of the ground-state density of that system. This leads to a great simplification of the problem, because electron density is a scalar quantity of the electrons' coordinates. Therefore, the Schrödinger equation associated with a multi-particle system will only depend on three dimensions rather than depending on the coordinates of all the electrons in the

[1] Contrary to a function that maps a number to a number, a functional maps a function to a number.

system as is the case for the wavefunction theory [2] Furthermore, electron density can be measured by experiment, and with the knowledge of the ground-state density all the physical properties of a system can, in principle, be obtained.

In order to have a better understanding of the Hohenberg-Kohn theorem, a closer look at the Hamiltonian in Eq. (3.11) is required: the first and the second terms on the right hand side of the equal sign are 'universal', meaning that they are the same for any system; the third term is different from one system to another. Therefore, it is only the electron-nuclei potential that characterizes the Hamiltonian, the eigenstates and any other physical observables such as the ground-state electron density.

The mapping is invertible meaning that given the ground-state electron density, the Hamiltonian and all the eigenstates and the expectation value of any operator, can be uniquely determined. Therefore, by knowing the ground-state density of a system, everything about that system, including the system ground-state energy, can be obtained.

In addition, Hohenberg and Kohn have a second theorem stating that for the ground-state density $n_0(r)$, the functional $E[n]$ (which is obtained by calculating the expectation value of $\hat{H}_{\text{elec}}$) takes on the value E_0 [43]. The ground state energy is uniquely determined by $n_0(\boldsymbol{r})$, therefore

$$E_0 < E[n(\boldsymbol{r})] \quad \text{for} \quad n(\boldsymbol{r}) \neq n_0(\boldsymbol{r}), \tag{3.12}$$

where

$$E[n(\boldsymbol{r})] = \langle \psi[n(\boldsymbol{r})] | \hat{T} + \hat{V}_{\text{ee}} | \psi[n(\boldsymbol{r})] \rangle + \int \hat{V}_{\text{ne}}(\boldsymbol{r}) n(\boldsymbol{r}) d\boldsymbol{r}. \tag{3.13}$$

Thus, based on the second Hohenberg-Kohn theorem we can find the ground-state energy of a multi-particle system by varying the electron density to minimize the energy.

Later, Kohn and Sham provided a useful formalism for practically using these theorems [120]. They suggested to use an auxiliary system with non-interacting electrons and then find a potential for which both the auxiliary system and the system of interest (with

[2] From practical aspect, the DFT approach to a system with N number of correlated electrons scales as N^3 whereas in the standard wavefunction approach this scaling is N^7.

interacting electrons) have the same ground-state density.

Once this density is found, the ground-state energy of the desired system can be found. The advantage of using a system with non-interacting electrons is that it makes solving the Schrödinger much easier, because the wavefuntion as well as the electron density of such a non-interacting system can be written in terms of the Slater determinant[3] of single-particle orbitals. In other words, in the Kohn-Sham (KS) system, the non-interacting electrons obey the one-particle Schrödinger equation with an effective potential which should match with the potential of the system with interacting electrons.

The Hamiltonian of a KS system is given by

$$\hat{H}_{\rm s} = \hat{T}_{\rm s} + \hat{V}_{\rm s}(\boldsymbol{r}), \tag{3.15}$$

where $\hat{T}_{\rm s}$ is the kinetic energy of non-interacting electrons given by $-\frac{1}{2m}\sum_i^N \langle\phi_i|\hat{\nabla}^2|\phi_i\rangle$ and $\hat{V}_{\rm s}(\boldsymbol{r})$ is the potential of the KS system. The ground state density of such system is given by

$$n_{\rm s}(\boldsymbol{r}) = \sum_{i=1}^{N} |\phi_i(\boldsymbol{r})|^2 \tag{3.16}$$

where $\phi_i(\boldsymbol{r})$ are the lowest-lying single particle states or orbitals which satisfy

$$\hat{H}_{\rm s}\phi_i(\boldsymbol{r}) = \epsilon_i\phi_i(\boldsymbol{r}). \tag{3.17}$$

The KS potential $\hat{V}_{\rm s}(\boldsymbol{r})$ is related to the potential of the desired system by

$$\hat{V}_{\rm s}(\boldsymbol{r}) = \hat{V}_{\rm ne}(\boldsymbol{r}) + \hat{V}_{\rm H} + \hat{V}_{\rm xc}(\boldsymbol{r}) \tag{3.18}$$

where the first term is the electron-nuclei potential, the second term is the classical part of $\hat{V}_{\rm ee}$ also known as Hartree potential given by

$$\hat{V}_{\rm H} = e^2 \int \frac{n(\boldsymbol{r'})}{|\boldsymbol{r} - \boldsymbol{r'}|} d\boldsymbol{r'}, \tag{3.19}$$

[3]The Slater determinant is an antisymmetric product of N one-electron wave functions:

$$\phi_{\rm SD} = \frac{1}{\sqrt{N!}} \det\{\chi_1(\boldsymbol{r}_1) \;\; \chi_2(\boldsymbol{r}_2) \;\; \cdots \;\; \chi_N(\boldsymbol{r}_N)\}, \tag{3.14}$$

where $\chi_i(\boldsymbol{r}_i)$ are the diagonal elements. $\chi_i(\boldsymbol{r}_i)$s are called *spin orbitals*, and are composed of a spatial orbital plus one of the two spin functions, $\chi(\boldsymbol{r}_i) = \phi(\boldsymbol{r}_i)\sigma(s)$ where $\sigma = \alpha, \beta$. Spin functions are orthogonal and spin orbitals are chosen to be orthogonal.

and $\hat{V}_{\text{xc}}(\boldsymbol{r})$ is the exchange-correlation (XC) potential and is given by

$$\hat{V}_{\text{xc}}(\boldsymbol{r}) = \frac{\delta \hat{E}_{\text{xc}}[n]}{\delta n}. \tag{3.20}$$

The exchange part of the XC potential arises from the antisymmetry feature of the system's wavefuntion and the correlation part corresponds to the dynamic correlation in the motion of the individual electrons. In other words, the exchange part corresponds to the same-spin interactions and the correlation part is due to mixed-spin interactions.

The XC potential $\hat{V}_{\text{xc}}(\boldsymbol{r})$ contains all the complex and nontrivial part of electron interactions corresponding to their quantum behavior. There is no an exact formulation for $\hat{V}_{\text{xc}}(\boldsymbol{r})$ and we need to approximate it using physical arguments. So far, a variety of reasonably good approximations have been developed [45]. Obviously, the quality of the DFT results depends on the quality of the approximation used for the XC potential.

The KS potential $\hat{V}_{\text{s}}(\boldsymbol{r})$ is a functional of the electron density. Thus, the KS equations given in Eq. (3.17) should be solved self-consistently, which means that first we need to assume an initial electron density, plug it in Eq. (3.18) and find the potential $\hat{V}_{\text{s}}(\boldsymbol{r})$, then solve the KS equations, Eq. (3.17), for the single-particle orbitals, and then use the result and find the corresponding electron density $n_{\text{s}}(\boldsymbol{r})$ from Eq. (3.16). Next, we should substitute the resultant electron density $n_{\text{s}}(\boldsymbol{r})$ into Eq. (3.18) to find a new $\hat{V}_{\text{s}}(\boldsymbol{r})$. We need to repeat this procedure untill no further changes occur to the electron density. The final electron density not only satisfies the Schrödinger equation of the KS system, but it is also the correct electron density of the desired system for that particular functional.

To summarize this section, DFT is a highly efficient technique for finding the ground state properties of a system with interacting electrons. While being computationally cost-effective, the accuracy of DFT calculations is usually comparable with traditional *ab initio* techniques. Practically, DFT calculations are done by solving the KS equations for an auxiliary system having non-interacting electrons; then finding the electron density of that system which is the same as the one of the system of interest.

In the following, two essential components for performing DFT calculations are discussed; these components are called "functional" and "basis set". Any pairing of these two components is a uniquely defined and uniformly applicable "theoretical model", also known as "model chemistry". Each model provides a unique approximation to the Schrödinger equation.

3.2.1 Functional

One of the key components that must be specified prior to performing a DFT calculation is "functional" (also known as "method" or "level of theory"). Usually, DFT methods are composed of an exchange functional paired with a correlation functional. Since the introduction of DFT, a wide variety of functionals have been developed [121] where one differs from the other by the type of the exchange and the correlation functionals that are used for $\hat{V}_{\mathrm{xc}}(\boldsymbol{r})$. Generally speaking, there are two types of functionals, known as"pure" functionals and "hybrid" functionals, some of which are briefly introduced in this section.

As mentioned earlier, the XC potential is usually approximated because it contains all the complex interactions of the electrons in a multi-particle system. The simplest case of approximation is to set the correlation part of $\hat{V}_{\mathrm{xc}}(\boldsymbol{r})$ to zero. As a result, electrons are influenced by the exchange potential and a mean field potential consisting of the classical Coulomb interaction. This approximation is called the Hartree-Fock theory, which is known as the lowest *ab initio* quantum theory.

Kohn and Sham proposed the local density approximation (LDA) [120]. In the LDA, one uses the knowledge of the exchange-correlation energy of the homogeneous electron gas [122]. In general, the form of $\hat{V}_{\mathrm{xc}}(\boldsymbol{r})$ not only depends on local density, but also depends on the density at all other points, and this dependence is usually unknown. In the LDA, one assumes that the inhomogeneous density of a system varies slowly enough that the exchange-correlation energy of that system is locally the same as that of a homogeneous system.

Local density approximation can be considered as the lowest-order term in the expansion of the exchange-correlation potential with respect to the electron density. Local density approximation is a very simple and reliable approximation for determining the structure of many species, but it is less accurate for calculating binding energies and dealing with details of the potential energy surface away from equilibrium geometries, such as transition states. However, it can be improved by including the gradient of the density in the approximation. The gradient-corrected approximation is known as the generalized gradient approximation (GGA), and it shows a dramatic improvement in the accuracy of some of the calculations over LDA, e.g. relative error of 3 to 7 percent for binding energies.

The functionals introduced above are "pure" functionals. These density functionals provide an approximation to both exchange and correlation parts of $\hat{V}_{\mathrm{xc}}(\boldsymbol{r})$. However, considering that the Hartree-Fock theory provides an exact exchange potential for a system, it is possible to greatly improve the result of a computational method by mixing some proportions of Hartree-Fock formalism with local- and non-local density exchange functionals. This approach to build a functional was first introduced by Becke [123] and the resultant was called "hybrid" functional.

One of the most commonly used "hybrid" functional in computational chemistry is the three parameter functional B3LYP [124, 125, 126] given by

$$\mathrm{E}^{\mathrm{xc}}_{\mathrm{B3LYP}} = \mathrm{E}^{\mathrm{xc}}_{\mathrm{LDA}} + c_0\,(\mathrm{E}^{\mathrm{x}}_{\mathrm{HF}} - \mathrm{E}^{\mathrm{x}}_{\mathrm{LDA}}) + c_{\mathrm{x}}\,(\mathrm{E}^{\mathrm{x}}_{\mathrm{GGA}} - \mathrm{E}^{\mathrm{x}}_{\mathrm{LDA}}) + c_{\mathrm{c}}\,(\mathrm{E}^{\mathrm{c}}_{\mathrm{GGA}} - \mathrm{E}^{\mathrm{c}}_{\mathrm{LDA}}) \tag{3.21}$$

where parameters $c_0 = 0.20$, $c_{\mathrm{x}} = 0.72$, and $c_{\mathrm{c}} = 0.81$ are empirical constant values that are determined by fitting this hybrid functional with atomization energies, ionization potentials, and some other properties of the G1 molecule set [124][4]. The parameter c_0 allows combining the exchange HF with the LDA exchange functional. These terms are corrected by Becke's gradient correction [128] to LDA which is scaled by parameter c_{x}. Equation (3.21) also contains the Lee-Yang-Parr (LYP) gradient-corrected correlation functional [126], $\mathrm{E}^{\mathrm{c}}_{\mathrm{GGA}}$, with a

[4]G1 molecule set is a set of 55 molecules, representing a broad range of chemical environments, which is used as a benchmark tool for gauging the accuracy of a given computational functional [127].

correction provided by Vosko-Wilk-Nusair (VWN3) local correlation functional E^{c}_{LDA} [125].

The development of functionals continues to be updated. Nowadays, even more complex functionals have been developed such as meta-hybrid GGAs [129]. Besides other factors, meta-hybrid GGAs have explicit dependence on the kinetic energy of the density of the system, as well. However, they are not introduced here, as they are out of the scope of this work.

3.2.2 Basis set

A "basis set" is the second key component that must be specified for a DFT calculation. A basis set is the mathematical description of molecular orbitals (MOs) in a multi-atomic system. Based on the molecular orbital theory [130], the electronic wavefunction of a system ψ and its electron density can be decomposed into a combination of normalized and orthogonal set of molecular orbitals ϕ_i[5]. Molecular orbitals are themselves composed of a set of basis functions χ_μ. These basis functions are usually centered on the atomic nuclei, thus bearing some similarities to atomic orbitals, such as s, p, and d.

Similar to the case of functionals, nowadays a wide range of predefined basis sets are available that are categorized based on the number and the type of basis functions that they contain. A basis set assigns a group of basis functions to each atom within a system, and then the molecular orbital of the system is approximated, accordingly. In the Gaussian program, basis functions are built from linear combination of gaussian-type "primitive" functions that have general form of

$$g(\alpha, \mathbf{r}) = cx^n y^m z^l e^{-\alpha \mathbf{r}^2}, \tag{3.22}$$

where α is determining the spatial extent of the function, and $\mathbf{r}$ is the spatial vector composed of x, y, and z components and c is the normalization factor so that $g(\alpha, \mathbf{r})$ is normalized

[5]To include the electron spin in ψ, each molecular orbital is multiplied by a spin function. The product of a molecular orbital and a spin function is called 'spin orbital'. The wavefunction of a system is then built by the determinant of spin orbitals where each row represent possible assignments of electron i to all spin-orbital combinations.

over all space. Therefore, the basis functions are given by

$$\chi_\mu = \sum_p d_{\mu p} g_p \tag{3.23}$$

where $d_{\mu p}$ represents constants within a given basis set. Consequently, the molecular orbitals are given by

$$\phi_i = \sum_{\mu=1}^{N} c_{i\mu} \chi_\mu, \tag{3.24}$$

where $c_{i\mu}$ are the molecular expansion coefficients.

As an example of interest, the basis set 6-31G(d) assigns six Gaussian primitives to the core atomic orbitals of the atoms of a system of interest; it assigns two sets of basis functions to the valence orbitals, the first one comprising three Gaussian primitives and the second one made of only one Gaussian primitive. Also, this basis set assigns d-type polarization functions to the atoms of the desired system.

Positions of electrons in a system can only be determined probabilistically; thus the larger the basis set, the more accurate is the approximation of molecular orbitals (MOs). However, larger basis sets come at the price of higher computational costs. Therefore, the choice of basis set should be made carefully.

3.3 Selection and limitations on chosen model chemistry

Density functional theory has become a standard tool to deal with problems such as evaluating molecular properties and chemical reactions. Nowadays, a lot of collaborative experimental and theoretical work have been produced in which DFT is used as the theory of choice [44, 131]. However, due to the large number of proposed density functionals [45, 121] and basis sets [44], certain amount of care is required for choosing an appropriate and cost-effective level of theory to solve any specific problem. For instance, a feasible level of theory for a large system, e.g. a piece of crystal, is the one that can balance between the size of the cluster (or the periodic slab) used for modeling the system and the size of the basis set

and the XC functional employed to assess the desired properties or the chemical reactions in that system.

In the DFT approach, one way to deal with a large-size system is to model it by a cluster [132]. The size of the cluster plays an important role in the accuracy of the calculations. For instance, when studying chemical reactions on the surface of a cluster, the finite size of the cluster's surface introduces error in the computed energies and reformed structure of the surface (caused by the chemical reactions). Different studies have been performed in assessing the cluster-size effect on the DFT calculations of different systems [54, 133, 134, 135]. These studies demonstrate that despite the chemical models employed in the calculations, the calculated results show convergence with respect to the cluster-size increment and the converged results become more comparable to the results found in a relevant experiment.

Finite-size basis sets suffer from two common problems known as basis-set incompleteness error (BSIE) and basis-set superposition error (BSSE) [136]. A basis set is complete if it has an infinite number of basis functions. A finite-size basis set imposes restrictions on the position of electrons in the system of interest, which leads to BSIE error in the desired calculations. In the case of BSSE, the basis set associated with each atom of the cluster model overlaps with the basis set of the neighboring atoms, thereby they compensate the incompleteness of each other. This "borrowing" feature effectively increases the size of the basis set used in a computation, which in turn would influence calculations such as energy and structural properties. Different methods have been proposed to eliminate this type of error [137, 138]. However, in the cases where a small basis set is applied to a large cluster, basis-set superposition helps to improve the results of a desired computation while keeping the computational costs at a reasonable level. Thus, a small basis set should be sufficient for evaluating properties in large-size systems [54, 132].

For clusters made of hundreds of heavy atoms B3LYP/6-31G(d) is the recommended chemical model [44, 131, 139]. Among the XC functionals, the hybrid functional B3LYP has

been (and still is) popularly used in computational chemistry [140]. Due to the extensive use of B3LYP in different studies, a large set of databases have been developed for evaluation of this functional [44, 131].

In some case studies (such as dealing with relative energies in a system) B3LYP provides reasonably good results comparable with those obtained from experiments and/or higher-level theories [44, 135, 141]. There are also cases where B3LYP fails to predict properly [136, 140, 141, 142]; a few examples are: underestimation of reaction barrier heights, failure to give reliable energy ordering of isomers, and underestimation of energy bandgap in semiconductors and insulators. However, new methods have been proposed recently to correct and extend the reliability and applicability of B3LYP [140].

Similar to any other choice of model chemistry, performance of B3LYP/6-31G(d) in predicting the properties of a system strongly depends on the chemical nature of that system [132]. However, different studies show that this specific model chemistry is a reliable model when dealing with medium- to large-size systems as it is computationally less expensive than other high-level *ab initio* models, and usually provides fairly good results with reasonable accuracy [136, 139, 54]. Nevertheless, for a system of choice, even if this DFT model chemistry performs poorly, it may still provide valuable qualitative insights and help in establishing a "big picture" of the property that is being pursued for that system.

An alternative approach for modeling a large-size system is the use of a periodic slab. In the slab modeling calculations are performed using planewave expansion and pseudopotentials. However, for systems that are hosting extra charges, this approach does not work properly, because replication of the unit cell for making the slab of interest causes duplication of the charge in the system, therefore leading to incorrectly calculated results. Also, a comparative study between the use of these two approaches for modeling a Si(100) crystal shows a lack of any convincing evidence that the results from slab models are better than those from cluster models [132]. Therefore, it is more appropriate to employ cluster modeling

to deal with Si systems that contain extra charges to avoid wrong results.

3.4 Time-dependent density-functional theory

Time-dependent density-functional theory (TDDFT) is a reformulation of time-dependent quantum mechanics in which the fundamental variable is the electron density of a system rather than its wavefunction [45]. This theory is used to investigate the dynamics and properties of multi-particle systems at the presence of a time-dependent potential caused, for example, by an electric field or a magnetic field. The TDDFT is popularly used in calculating the excitation energies of multi-particle systems, because it is shown that the density response function to a potential change has poles in the exact location of the excited states of a system and thus gives the exact excitation energies of that system.

The conceptual and computational foundation behind TDDFT is analogous to the one for DFT. Time-dependent DFT is conceptually built based on the Runge-Gross (RG) theorem [143], which is the time-dependent analogue of the Hohenberg-Kohn theorem. The RG theorem states that in a time-dependent multi-particle system, there is a one-to-one correspondence between the external potential $V_{\text{ext}}(\boldsymbol{r}, t)$ and the electron density $n(\boldsymbol{r}, t)$ of the system, but this functional relationship depends on the choice of the initial state $\psi_0(\boldsymbol{r}, t)$ of the system [143].

The RG theorem conceptually implies that if one knows the density of a system then the external potential that produces this density can uniquely be determined. Once the potential is specified, one can solve the time-dependent Schrödinger equation of the system and find all other properties of that system. However, to obtain this information knowing the initial state of the system is also required.

To establish a computational formalism for TDDFT, one should consider a fictitious non-interacting system (known as the Kohn-Sham system) subjected to an effective external potential $V_{\text{s}}[n](\boldsymbol{r}, t)$ that causes the Kohn-Sham system to display the same density as the

system of interest (having interacting electrons). The time-dependent Schrödinger equation for the Kohn-Sham orbitals is

$$i\hbar \frac{\partial \varphi_{\mathrm{i}}(\boldsymbol{r},t)}{\partial t} = \left[-\frac{\hbar^2}{2m} \hat{\nabla}^2 + \hat{V}_{\mathrm{s}} \left[n\right] (\boldsymbol{r},t) \right] \varphi_{\mathrm{i}}(\boldsymbol{r},t). \tag{3.25}$$

The density of the desired system can then be calculated from the Kohn-Sham orbitals using

$$n(\boldsymbol{r},t) = \sum_{i}^{N} |\varphi_i(\boldsymbol{r},t)|^2. \tag{3.26}$$

The time-dependent Kohn-Sham potential is decomposed of three terms

$$\hat{V}_{\mathrm{s}} \left[n\right] (\boldsymbol{r},t) = \hat{V}_{\mathrm{xc}} \left[n\right] (\boldsymbol{r},t) + \hat{V}_{\mathrm{ext}} \left[n\right] (\boldsymbol{r},t) + \hat{V}_{\mathrm{H}} \left[n\right] (\boldsymbol{r},t). \tag{3.27}$$

Similar to DFT calculations, the first term corresponding to the exchange-correlation potential is the only functional approximation used in TDDFT calculations.

In TDDFT calculations the aim is to find changes in the density of the system as a response to the time-dependent external potential. Suppose that for a system with interacting electrons, up to some time t_0, the external potential is the one provided by the nuclei of the system, $V_0(\boldsymbol{r})$, and at $t \geqslant t_0$ a small time-dependent perturbation $V_1(\boldsymbol{r},t)$ is applied to the system. Applying a small potential guarantees that the ground state of the system is not completely destroyed due to this potential, thus the system properties found by DFT can be used to calculate the properties of its excited states. In this case, one can use the linear response of the system, which can be obtained by expanding the density in a Taylor series

$$n(\boldsymbol{r},t) = n_0(\boldsymbol{r}) + n_1(\boldsymbol{r},t) + \cdots \tag{3.28}$$

where the second term is a linear function of $V_1(\boldsymbol{r},t)$ and is given by

$$\delta n_1(\boldsymbol{r},t) = \chi(\boldsymbol{r},t;\boldsymbol{r'},t')\delta V_1(\boldsymbol{r'},t'). \tag{3.29}$$

$\chi(\boldsymbol{r},t;\boldsymbol{r'},t')$ is the response function and it describes the amount of change in the density of the system as a result of the change in the external potential.

Similarly, we can consider the response function of the non-interacting KS system to the external potential and then relate these two response functions together [45]. The KS response function is a function of the exchange-correlation potential. The Fourier transform of the system's response function turns out to have poles at the exact excitation energies of the interacting system. Thus, the linear response theory provides a practical way to calculate the excitation energies of a system with interacting electrons.

3.5 Selection and limitations of TDDFT

One can find the highest occupied molecular orbital (HOMO) and the lowest unoccupied molecular orbital (LUMO) of a system with the use of DFT. However whether these orbitals correspond to the ground state and the first excited state of the system, respectively, is under question. In fact the question is why should one employ TDDFT, when DFT is also able to provide information about the excited state of the system? This concern can be addressed by considering the cases where the system has only two energy levels such as H_2^- (which is similar to the case of a DBP^-).

In a two-level system containing three electrons (e.g. H_2^-), the lower energy state (i.e. called the ground state or the bonding orbital) is doubly occupied and the higher energy state (called the first excited state or the antibonding orbital) is singly occupied by an electron. Density functional theory calculates the energy corresponding to the highest occupied molecular orbital (HOMO), which in this case is the single electron in the anti-bonding orbital. Thus, DFT energy calculation of the antibonding orbital is associated with the HOMO of the system.

On the other hand, time-dependent DFT (TDDFT) determines the electron density of the ground state and the first excited state of the system, and calculates the transition energy required to move an electron from the former state to the latter. For instance, in the case of H_2^-, TDDFT enables estimating the energy required to move an electron from

doubly occupied (bonding) to singly occupied (antibonding) molecular orbital (SOMO). Thus, within the framework of the used model chemistry, TDDFT correctly addresses the excited state and consequently gives a better estimation of the corresponding excitation energy [144].

Time-dependent DFT has become a popular technique for dealing with electronic excitation spectra, specially in medium- and large-size molecular systems [145, 146] due to its relatively low computational cost. Especially for excitation states that are energetically below the first ionization potential, TDDFT has shown remarkably accurate results with an error range of $0.1 - 0.5$ eV as compared to the experimental data [133, 134].

Despite its high accuracy performance, since TDDFT employs XC functionals it suffers from certain severe problems such as correctly calculating Rydberg states, excited states involving significant charge transfer [147, 148], and excitation states in molecules with extended π-conjugation [142, 145, 146]. Perhaps the best way to check the reliability of TDDFT (and also DFT) calculations is to compare the results with the ones of a relevant experiment or with the results obtained from other choices of XC functionals. If the system is small enough that wavefunction-based calculations are feasible, then this can be an alternative for checking the reliability of the (TD) DFT calculated results.

3.6 Summary

To summarize, this chapter contains experimental tools and (TD) DFT techniques required for investigating the level of coherence of DBP^{-}s. For a multi-atomic system (e.g. the Si structure of our interest) finding the exact solution to the Schrödinger equation is impossible due to the limitation on the resources. Density-functional theory provides the best approach by suggesting to use the electron density of the system as the variable rather than using the electron and nuclear coordinates.

To solve the Schrödinger equation with this technique specifying a theoretical functional

and a basis set is required. A wide variety of functionals and basis sets are available. Employing larger basis sets and better functionals improves the ability of the computational model to approach the real results. However, this requires jobs running for longer times. Therefore, in choosing the right basis set and functional for calculating a chemical cluster, one should try to balance between accuracy of the result and the computational cost.

Chapter 4

Dangling-Bond Charge Qubit on a Silicon Surface

In this chapter, we propose a coupled dangling-bond pair (DBP^-) positioned on Si(100)–2×1 surface as a potential candidate for a charge qubit. A first-order analysis of the coherent dynamics of such a system shows that its extremely high tunneling rate greatly exceeds the expected decoherence rates for a silicon-based system, thereby overcoming a critical obstacle of the charge qubit for quantum computing. However, the fast dynamics of DBP^- comes at the price of requiring fast control and gating for quantum computation.

This chapter begins with a description of the formation of coupled dangling-bond pairs. Also, for a particular DBP^- configuration, its tunneling rate as a function of DB-pair separation is analyzed in Sec. 4.1. Then, the effect of dominant sources of noise (i.e. electrodes charge fluctuation and silicon-substrate phonon modes) on the dynamics of the DB system is investigated and the resultant decoherence rates are estimated in Sec. 4.2. The quantum dynamics of a large number of DBP^-s in the frame of a new architecture for quantum computing purposes is formulated in Sec. 4.3. In Sec. 4.4 we mention how these DBP^-s could find applicability in a quantum computing circuit. This chapter wraps up by briefly summarizing the main objectives of this work.

The majority of the material in this chapter is taken from our collaborative work which has been published in New Journal of Physics [2]. However, wherever required, new material is added or existing material is shifted or eliminated to keep the chapter fluent. Those parts that are reproduced verbatim from our journal paper are listed in "Materials reproduced from my published paper". As part of this collaboration, I designed a new architecture for quantum computing with any number of DBP^-s and determined the Hamiltonian that describes the quantum dynamics associated with this architecture. More specifically, I showed

the Hamiltonian assoicated with a bias-controlled DBP^- as well as the Hamiltonian incorporated with two DBP^-s having Coulombic interactions. These two specific Hamiltonians describe the quantum dynamics leading to single-qubit and two-qubit gates required for quantum computation.

The result of my calculations is reported in Sections 4.3 and 4.4. The result on decoherence analysis, which is reported in Sec. 4.2, is developed by our collaborators but it is included in this chapter because it is an essential part of our analysis on DBP^- coherent dynamics. However, I understand the concept of this section as it is part of the DBP^- characterization.

4.1 Dangling-bond pairs as charge qubits

Structural and electrical properties of dangling bonds are described in Sec. 2.3. A neutral DB hosts a bound electron within the Si 1.1 eV bulk band gap. The itinerant electrons available in a doped semiconductor can provide a second electron of opposite spin to the DB, thus rendering it a DB^-. If two DB^-s are sufficiently close together (≤ 16 Å), Coulombic repulsion ensures that a doubly-charged DB^--DB^- pair cannot form [1]. Hence, a closely-spaced DB pair (DBP^-) shares one extra electron tunneling between the two centers, suggesting its use as a charge qubit. Tunnel-coupled DBs, as shown in Fig. 4.1(a), have been created on a H–Si(100)–2×1 surface by using a scanning tunneling microscope (STM) tip to remove H atoms at selected sites [1]. A brief background information on STM can be found in Subsec. 3.1.2.

Separation between the two DBs forming a pair has a strict lower bound of 3.84 Å as determined by the lattice spacing of the Si(100) surface, whereas the upper bound for enabling a qubit is given by a separation of about 16 Å. Distinct pairs are created farther apart than this limit to avoid inter-pair tunnel coupling. Here, we claim that coupled dangling-bond pairs (DBP^-) exhibit coherent quantum dynamics and can serve as good charge qubits.

The localized nature of the DB wavefunction and its energy level in the band gap allows

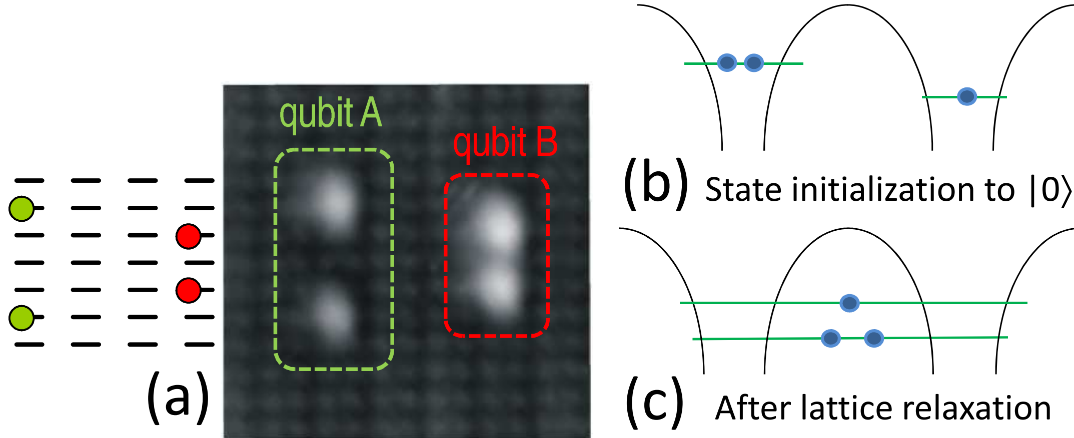

Figure 4.1: (a) Variably spaced qubits in an atom-resolved STM image (46 Å×46 Å, 2 V, 0.2 nA) created from pairs of DBs on a H–Si(100)–2×1 surface, separated by 15.36 Å (qubit A) and 7.68 Å (qubit B). Dangling bonds appear as bright protrusions in the gray scale image. A schematic (left) shows the position of DBs (red and green circles) on the Si surface. Black dashes represent silicon dimers. (b) A DB-DB$^-$ pair modeled as double-well potential, with the extra electron at the left well immediately after initialization to $|0\rangle$. (c) Relaxed ground state of the DB electrons after lattice relaxation has completed. [reproduced from ref. [2], Fig. 1]

us to formulate an electron-confinement model corresponding to a potential well accounting for the effect of the environment. Such a potential-well description must render the correct eigenstate energy and orbital size, and must allow for electron excitation into the bulk conduction band of the crystal. In a highly-doped n-type crystal, a high Fermi level of the crystal allows an extra electron to be localized at a DB, rendering the DB site negatively charged. Similarly, if the crystal is p-type, the DB can lose all its electrons thereby becoming positively charged.

In Figures 4.1(b) and (c), we depict a DB pair as an effective double-well potential with (b) an excess electron at the left well immediately after release from a biasing external field, as required for qubit initialization, and (c) after complete lattice equilibration when the potential landscape becomes symmetrical. Due to the localized extra charge, the double-well in case (b) does not exhibit the symmetry of case (c), and the DB energy is shifted upward at the left site. Consequently, during lattice relaxation, the coherent oscillation between the

two DBs takes place between two wells of slightly different shapes, resulting in a periodic oscillation that is biased towards the 'left' (excess electron spends more time on the left than on the 'right'). Slow relaxation of the lattice will modify the electron oscillation and cause weak decoherence.

We calculate tunneling rates of a DBP^- for various separations using two different methods. Employing (time-dependent) density-functional theory ((TD) DFT) on cluster models [149], the energy splitting for DBP^- separations of 3.84 Å and 7.68 Å is determined to be 307.7 meV and 87.8 meV, respectively. These values correspond to tunneling rates of $4.67\times10^{14}s^{-1}$ and $1.33\times10^{14}s^{-1}$, respectively. For these calculations, we assumed that the two DBs are located on the same-side Si dimers of one dimer row, and are separated by one or two dimer spacing resulting to the DBP^- separations given above; see Fig. 4.1(a).

For larger separations, the size of Si-cluster model becomes expensive for this type of computation. Thus, for the purpose of this chapter, we use a simpler approximations, namely the Wentzel-Kramers-Brillouin (WKB) method (see Sec. 2.7 for a description on this method). In Ch. 5, we evaluate the energy splitting of DBP^-s with larger separations and different configurations using (TD) DFT techniques. We use these *ab initio* methods, despite their computational costs, to investigate the effect of anisotropic structure of H-terminated Si(100)–2×1 surface on DBP^- energy splitting.

The Log-line plot in Fig. 4.2 shows the result of our calculations. Vertical axis represents the DB excess-charge tunneling rate while the horizontal axis shows the DB-pair separation. The first two points, shown by circles, are the results of *ab initio* (TD) DFT calculation and the rest of the points are found by WKB approximation. As expected, the DBP^- tunneling rate strongly depends on DB-pair separation and decreases exponentially by increasing the separation. Achieving the extremely high tunneling rate is the result of the atomic-size DBs and the capability of creating them very close to each other.

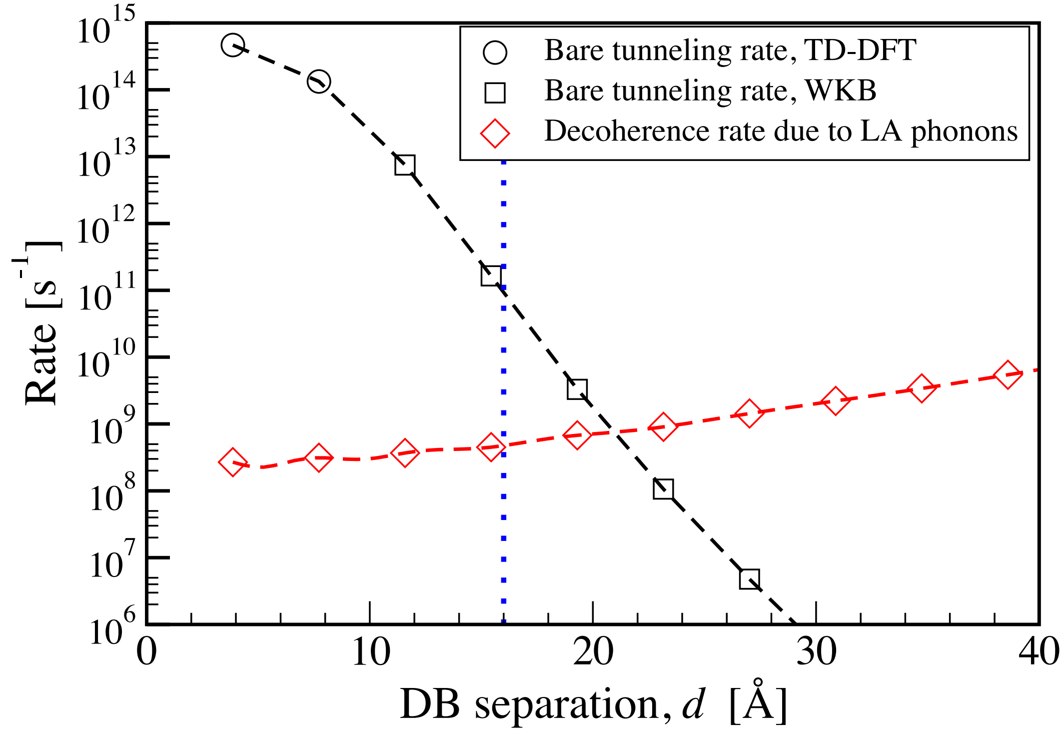

Figure 4.2: Bare tunneling rates of the excess electron in a DBP^- by time-dependent density-functional theory (black circles) and the WKB method (black squares) versus DBP^- separation d. The red line depicts the calculated decoherence rate due to longitudinal-acoustical (LA) phonons. The vertical blue dotted line indicates (to its left) the region in which the two DBs are tunnel coupled. [reproduced from ref. [2], Fig. 3]

4.2 Decoherence analysis for DB-pair qubit systems

For a DBP^- on a hydrogen-terminated Si(100) surface, we treat the decoherence mechanism due to various interactions with the environment using the spin-boson model[1] (see Sec. 2.6 for more detail on this model). Based on earlier studies on silicon systems [13, 40], we estimate that the main sources of decoherence for our system are: (i) the voltage fluctuations on the gate electrodes, and (ii) the interaction between the qubit electron and phonons in silicon bulk and at the surface. In the following, we analyze these two cases in detail.

[1] The material in this section was developed by co-author Lucian Livadaru

4.2.1 Decoherence due to Johnson-Nyquist voltage fluctuations

Johnson-Nyquist noise is due to random thermal fluctuations of the charge carriers in a conductor or semiconductor. For the purpose of calculating its effect on the coherent oscillations in a DBP$^-$, we employ the spin-boson model with the qubit being the two-level system and the gate electrode being the bath. In order to obtain a reliable estimate of the decoherence effect, we need to look at how the power spectrum of the bath compares to the bare tunneling frequency of the qubit.

The Johnson noise stretches uniformly in the frequency range from zero up to about 10^{11}-$10^{13}\mathrm{s}^{-1}$. In particular, we can see that for a temperature $\Theta = 4$ K the spectrum has a cutoff frequency $\omega_\mathrm{c} = 5.2 \times 10^{11}\mathrm{s}^{-1}$. As the bare tunneling frequency of our DBP$^-$ has a value of $\Delta \approx 10^{14}\mathrm{s}^{-1} \gg \omega_\mathrm{c} \approx 10^{12}\mathrm{s}^{-1}$, we can safely regard the effect of the bath on the qubit as being approximately adiabatic (i.e. changes in potential-energy experienced by a DBP$^-$ excess electron due to fluctuations in the bath vary slowly in time compared to the bare tunneling frequency of the DBP$^-$).

To proceed, we assume ohmic dissipation (corresponding to $s = 1$ in Eq. (2.9) for the bath spectral density function), so the spectral function in the spin-boson model has the form

$$J(\omega) = \alpha_\mathrm{JN}\omega \exp(-\omega/\omega_\mathrm{c}) \tag{4.1}$$

for

$$\alpha_\mathrm{JN} = \frac{\eta d}{2\pi\hbar} \tag{4.2}$$

a dimensionless dissipation/coupling function of the distance between the two charge centers d and viscosity coefficient η.

One of the simplifying features of the spin-boson Hamiltonian is that, in the limit of weak qubit-bath coupling, the decoherence times T_1 (describing population decay) and T_2 (describing coherence decay) are equal to second order in the coupling [38], which allows to characterize the system by a single decoherence rate $\Gamma = 1/T_1$. In the adiabatic limit

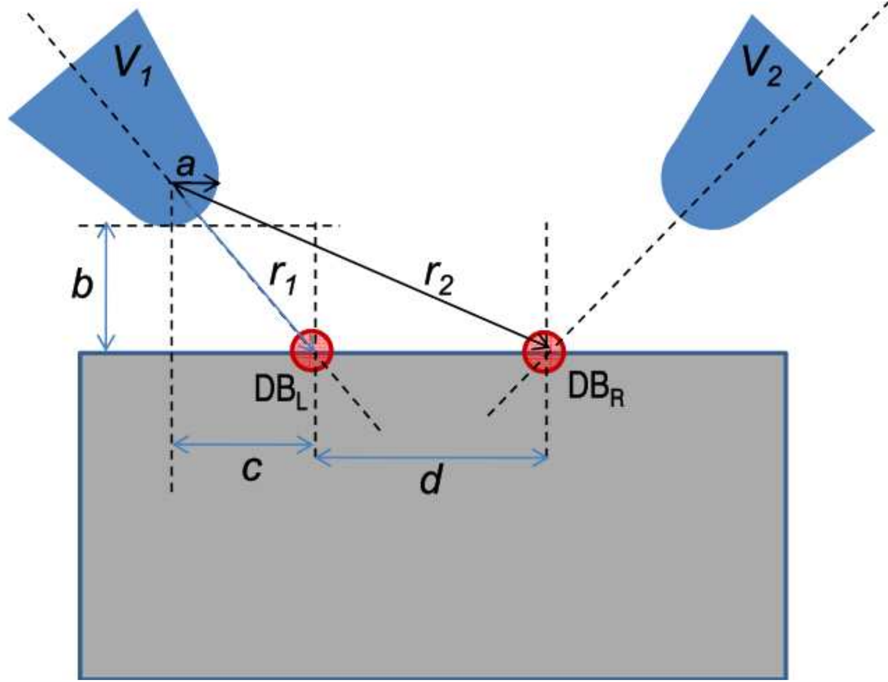

Figure 4.3: Sketch of the gating geometry for our proposed DBP^- qubit on silicon surface. DBs are indicated as red circles and are indexed L and R corresponding to their locations. The electrodes (based on STM tips) are indicated in blue and have fixed potentials V_1 and V_2, with $V_{12} = V_1 - V_2$. The radius of the electrode at the apex is a. [reproduced from ref. [2], Fig. 2]

($\Delta \gg \omega_c$), and for the case when $\omega_c \gg \Gamma$ (which can be verified a posteriori), the decoherence rate for the DBP^- can be determined according to [99, 100]

$$\Gamma_{JN} = \frac{1}{2} \frac{\sqrt{\pi}\hbar\Delta^2}{1 + \frac{\hbar\Delta^2}{\omega_c E_r}} \frac{\exp(-\frac{E_r}{4kT})}{\sqrt{\frac{E_r}{k\Theta}}} \tag{4.3}$$

for E_r the bath reorganization energy

$$E_r = \hbar \int_0^\infty d\omega \frac{G(\omega)}{\omega} \tag{4.4}$$

which can be calculated from Eq. (4.1) to yield

$$E_r = 2\alpha_{JN}\hbar\omega_c. \tag{4.5}$$

For a typical charge-qubit gating [13]

$$\alpha_{\rm JN} = \frac{e^2\beta^2 R_{\rm g}}{4h} \tag{4.6}$$

for $R_{\rm g}$ the resistance of the gate circuit, and

$$\beta = \frac{\delta V_{\rm LR}}{\delta V_{12}} \tag{4.7}$$

where $\delta V_{\rm LR}$ is the potential difference between the two DB sites, δV_{12} represents the bias-gate voltage fluctuation, and β is another dimensionless parameter that depends solely on the system geometry. Here, parameter $V_{\rm LR}$ the difference between the electrostatic potentials at the L and R sites and V_{12} the difference between in the applied voltage on the two electrodes.

A simple approximation (but yielding good order-of-magnitude estimate) for the electrostatic problem (Fig. 4.3) yields

$$\delta V_{\rm LR} \approx \left(\frac{a}{r_1} - \frac{a}{r_2}\right)(V_1 - V_2) \tag{4.8}$$

whence we obtain

$$\beta_{\rm JN} \approx a\left(\frac{1}{\sqrt{c^2+(a+b)^2}} - \frac{1}{\sqrt{(c+d)^2+(a+b)^2}}\right). \tag{4.9}$$

Plugging in reasonable estimates for the parameters: $a = b = c = 2$ nm, $d = 0.772$ nm, we find $\beta = 0.036$. Further, by assuming $R_g = 50\ \Omega$ and using Eq. (4.6) yields $\alpha_{\rm JN} = 6.364 \times 10^{-7}$.

Finally we can calculate the decoherence rate due to Johnson-Nyquist noise for a DBP$^-$ charge-qubit implementation depicted in Fig. 4.3 with typical parameters $\Delta = 1.33{\times}10^{14}$ s^{-1}, $\omega_{\rm c} = 1.31 \times 10^{11}$ s^{-1} (Θ= 1 K). From Eq. (4.3) we obtain

$$\Gamma_{\rm JN} = 1.30 \times 10^8 \text{ s}^{-1}, \tag{4.10}$$

which is much less than $\omega_{\rm c}$, thereby showing that our approximations are consistent. Note that as the bare tunneling rate in a qubit increases, fluctuations in the tunneling splitting

can play an important role in the coupling with the environment. The spin-boson model can only accommodate such system as far as the tunneling rate is much less than the classical oscillation frequency ω_0 corresponding to electron confinement in an isolated DB.

As the confinement energy in a DB is about 0.6 eV, this condition is generally fulfilled for all qubit configurations, with the exception of the qubit with a separation of 3.84 Å. Therefore, we must bear in mind that, in this limit, the accuracy of the spin-boson model may be unreliable. Nonetheless, the decoherence for all other DB separations can be accurately treated by this model because the corresponding tunnel-splitting energy is much less than the binding energy 0.6 eV. Therefore, we claim that decoherence rate of our DB system due to charge fluctuation is much smaller than the DBP^- bare tunneling frequency, which is a favorable fact for implementing reliable quantum gates.

4.2.2 Decoherence due to electron-phonon interaction

Previous studies on electron-phonon scattering in reduced-dimension systems have found that, for zero-dimensional systems, such as quantum dots, the scattering rates are smaller by at least an order of magnitude than in one- and two-dimensional systems [150]. This is due to the fact that, for a given initial state of the electron, the number of final states is greatly reduced in the zero-dimensional case. For our system, if the DBP^- excess charge is in the antibonding state (also known as the first excited state), only the bonding (ground) state is lower in energy, thereby drastically reducing coupling to phonons.

Nonetheless, for our system, the interaction between electrons and phonons can be a serious source of decoherence, and we anticipate that in our system as it dominates all other forms. From previous experimental and theoretical studies [151] on phonons in the Si(100) crystal, we know that the phonon spectrum can extend up to about 70 meV, corresponding to a frequency of $1.06 \times 10^{14}\text{s}^{-1}$. This rate is comparable to the bare tunneling frequency of our DB system, which means that the adiabatic approximation used in the previous section fails.

A different approach is required and, as in previous theoretical analyses of the electron-phonon interaction, we calculate the rates of electron-phonon scattering within the frame of the first-order perturbation theory via the Fermi golden rule given by [150]

$$\Gamma_{\text{e-ph}} = \frac{2\pi}{\hbar} \sum_{f,\boldsymbol{q}} \alpha^2(\boldsymbol{q}) \left| \langle \psi_f | e^{\pm i\boldsymbol{q}\cdot\boldsymbol{r}} | \psi_i \rangle \right|^2 \times \delta(E_f - E_i \mp E_q) \left[n_{\text{B}}(E_q, \Theta) + \frac{1}{2} \mp \frac{1}{2} \right] \tag{4.11}$$

for i and f indicating the initial and final electronic states, $\boldsymbol{q}$ the phonon wavevector and $q = |\boldsymbol{q}|$, E_q the phonon energy, $\alpha(q)$ a coupling function, n_{B} is the Bose occupation distribution, and upper/lower signs corresponds to absorption/emission of a phonon by the system of interest, i.e. the DBP$^-$ in our case.

Below, we quantify the coupling of the DBP$^-$ excess charge with the longitudinal-acoustic (LA) phonons only (see Sec. 2.2 for more details on different types of phonons). The coupling of the excess electron to the longitudinal-optical (LO) phonons is also possible. However, optical phonons have a more discrete-like energy spectrum (set of distinct spectral lines), and this fact prevents any first-order coupling to electrons, unless the energy matching condition

$$\hbar\omega_{\text{LO}} = E_f - E_i \tag{4.12}$$

is fulfilled. Condition (4.12) can be avoided in our system by judiciously choosing the inter-dot distance and the amplitude of the applied bias.

If the coupling is given via a deformation potential, D, then the coupling function above can be shown to be

$$\alpha^2(q) = \frac{D^2}{2\rho c_{\text{s}}^2 \Omega} \hbar c_{\text{s}}^2 q \tag{4.13}$$

where c_{s}^2 is the longitudinal sound velocity, ρ is the density, and Ω is a normalization volume. Piezoelectric coupling to acoustic phonons is also possible, but in general it is much weaker (by an order of magnitude [150]) than the coupling via a deformation potential. After appropriate manipulation, the expression for the scattering rate can be reduced to [152]

$$\Gamma_{\text{e-ph}} = \frac{D^2 q_{if}^3}{8\pi^2 \hbar \rho c_{\text{s}}^2} \left[n_{\text{B}}(E_q, \Theta) + \frac{1}{2} \mp \frac{1}{2} \right] \int \mathrm{d}\Omega_{\boldsymbol{q}} | \langle \psi_f | e^{\pm i\boldsymbol{q}\cdot\boldsymbol{r}} | \psi_i \rangle |^2 \tag{4.14}$$

where $q_{if} = E_{if}/\hbar c_{\mathrm{s}}$ for E_{if} the energy difference between the i and f states and $\mathrm{d}\Omega_{\boldsymbol{q}}$ is the solid angle element in $\boldsymbol{q}$-space.

As in previous studies [13, 40] we assume that a DB can be modeled as a 1s hydrogen-like orbital with a renormalized Bohr radius, a_{B}, and we fit this parameter so that the tunnel splitting of a DB pair derived from the hydrogen-like model reproduces the value predicted by our *ab initio* calculations for a DB separation of 7.68 Å. Then it can be shown that the rate of phonon emission is given by

$$\Gamma_{\text{e-ph}} = \frac{64D^2q^3\sin^2\theta}{\pi\rho\hbar c_{\mathrm{s}}} \frac{n_{\mathrm{B}}(E,\Theta)+1}{[(qa_{\mathrm{B}})^2+4]^4} \left(1 - \frac{\sin qd}{qd}\right) \tag{4.15}$$

where $\theta = \tan^{-1}(\hbar\Delta/\varepsilon)$, and ε is the applied bias on the qubit, and d is the dot separation. Note that the results for $\Gamma_{\text{e-ph}}$ are of the same order of magnitude for any other form of the isolated dot wavefunction exhibiting exponential decay, as long as the decay rate is similar.

The decoherence rate due to electron interaction with LA phonons is plotted in Fig. 4.2 as a function of dot separation. Note that, for our DB system, the above rate $\Gamma_{\text{e-ph}}$ is greater than the decoherence rate due to Johnson noise in the electrodes, Γ_{JN}, calculated in the previous section. Thus we identify $\Gamma_{\text{e-ph}}$ as the dominant decoherence rate. We note an important fact for our DBP$^-$: relaxation via this mode occurs over several nanoseconds whereas the tunneling period for the DBP$^-$ with a few Å separation is close to 10 fs, which enables many coherent qubit oscillations before decoherence sets in.

Other phonon modes both in bulk and at the surface [151] are less likely to couple to electron tunneling due to their discrete-like energy spectrum. At least for DB separations of 3.84 Å and 7.68 Å, there are no phonon modes to match the tunnel splitting energy, as the highest phonon energy is about 70 meV. A more detailed analysis of the qubit coupling to the optical phonon modes is beyond the scope of this paper. Overall, we estimate that for our closely spaced DBP$^-$s, the excess-charge oscillations will take place over many periods before the onset of critical decoherence, illustrating the advantage of closely spaced quantum dots for charge qubit.

4.3 Quantum dynamics for any number of DBP$^-$s

Consider i number of DBs on the Si surface, and let E_{os} to be the on-site energy of an electron in any DB site, and η_i be a site-dependent energy correction due to any local field effect (such as the lattice deformation due to the excess electron, or the potential-well deformation due to an external bias field). Also, suppose that electron tunneling between sites i and j is given by $T_{ij} = \hbar\Delta_{ij}/2$, where Δ_{ij} is the electron tunneling rate and depends on DB pair separation r_{ij}; and U_i and $W_{i\sigma j\sigma'}$ are the intra- and inter-DB Coulomb repulsion between electrons, respectively. The subscripts σ and σ' represent the electron spin $\{\uparrow, \downarrow\}$ at sites i and j, respectively. The above parameters are all incorporated into Hamiltonian $\hat{H}$.

Furthermore, tunneling between DB sites can be controlled by modifying the inter-site potential bias. For example two sites i and j can have a time-dependent potential difference of $V_{ij}(t)$. For $\hat{c}_{i,\sigma}$ ($\hat{c}^\dagger_{i,\sigma}$) the annihilation (creation) operator for an electron with spin σ at site i and $\hat{n}_{i,\sigma} = \hat{c}^\dagger_{i,\sigma}\hat{c}_{i,\sigma}$ the number operator for electrons of spin σ at site i, the potential difference operator between sites i and j is

$$\hat{V} \equiv \frac{1}{2}\sum_{i<j,\sigma} V_{ij}(\hat{n}_{i,\sigma} - \hat{n}_{j,\sigma}). \tag{4.16}$$

We now have all the terms required to express the Hamiltonian as an extended Hubbard model [42]:

$$\hat{H} = \sum_{i,\sigma}(E_{\text{os}} + \eta_i)\hat{n}_{i,\sigma} - \sum_{\substack{i<j \\ \sigma}} T_{ij}(\hat{c}^\dagger_{i,\sigma}\hat{c}_{j,\sigma} + \hat{c}^\dagger_{j,\sigma}\hat{c}_{i,\sigma}) + \sum_i U_i\hat{n}_{i,\uparrow}\hat{n}_{i,\downarrow} + \sum_{i<j,\sigma,\sigma'} W_{i\sigma j\sigma'}\hat{n}_{i,\sigma}\hat{n}_{j,\sigma'} + \hat{V}. \tag{4.17}$$

The Hamiltonian acts upon a Hilbert space that is spanned by zero, one, or two electrons per each DB site. Considering the spin of electrons as well as their position, the Hilbert space associated with the Hamiltonian is obtained by the tensor product of the Hilbert spaces $\mathscr{H}_{\text{p}}$ for electrons position and $\mathscr{H}_{\text{s}}$ for their spin. Alternatively, the Hilbert space can be written as a direct sum of $\mathscr{H}_\ell$, where ℓ stands for the number of electrons associated with each sector of the Hilbert space. For instance, for a pair of DBs, with the possibility of having zero up

to maximum four electrons, the Hilbert space is given by

$$\mathscr{H} = \mathscr{H}_{\mathrm{p}} \otimes \mathscr{H}_{\mathrm{s}} = \oplus_{\ell=0}^{4} \mathscr{H}_{\ell} = \mathrm{span}\left\{ \left| \varepsilon_{\mathrm{L}\uparrow}, \varepsilon_{\mathrm{L}\downarrow}, \varepsilon_{\mathrm{R}\uparrow}, \varepsilon_{\mathrm{R}\downarrow} \right\rangle \right\},$$

where $\varepsilon_{i\sigma} \in \{0,1\}$ and $\sum_{i\sigma} \varepsilon_{i\sigma} = \ell \in \{0,1,2,3,4\}$. Therefore, the Hilbert space for such a system is composed of five sectors, and consequently the Hamiltonian describing a pair of DBs has sixteen dimensions.

The above Hamiltonian describes the dynamics of any number of DBs in a quite general layout. However, we are interested to develop a well-patterned architecture comprising closely-spaced DB pairs, with each pair sharing one excess electron (DBP$^-$), and relatively large inter-DBP$^-$ separation so that T_{ij} is non negligible only for intra-pair dynamics. However, the amount of separation is such that it allows DBP$^-$s to have Coulombic interaction with each other. Using Eq. (4.17), we derive the Hamiltonian that describes the dynamics of such an architecture.

A coupled DB pair sharing an excess electron contains a total of three electrons; thus for a DBP$^-$ we focus on $\ell = 3$ portion of the Hilbert space. In the $\ell = 3$ sector, the Hamiltonian acts on a four-dimensional Hilbert space spanned by

$$\mathscr{H}_3 = \left\{ \left|1,1,1,0\right\rangle, \left|1,1,0,1\right\rangle, \left|1,0,1,1\right\rangle, \left|0,1,1,1\right\rangle \right\}.$$

In position representation this basis set is equivalent to $\{\left|\mathrm{L}\uparrow\right\rangle, \left|\mathrm{L}\downarrow\right\rangle, \left|\mathrm{R}\uparrow\right\rangle, \left|\mathrm{R}\downarrow\right\rangle\}$, where L and R stands for the 'left' and 'right' DBs in the DBP$^-$, respectively. The spin is unimportant provided that interactions are spin independent.

In our system of interest, we assume that the electron spin is preserved as the DBP$^-$ spin coupling with surrounding environment is believed to be small and negligible [1]. Consequently, the DBP$^-$ dynamics can be modeled by a two-level system and the corresponding four-dimensional Hamiltonian can be written as a direct sum of two identical (two-dimensional) Hamiltonians, each corresponding to one of the spins. Considering the 'left' (L) state $|0\rangle$ and the 'right' (R) state $|1\rangle$ to form a basis for the Hamiltonian and using

Eq. (4.17), the Hamiltonian for a DBP$^-$ influenced by an applied bias is derived to be

$$\hat{H}_{\mathrm{DBP}^-}(t) = (3E_{\mathrm{os}} + 3\eta + U_0 + 2W_0)\,\mathbb{1} + T\hat{X} + \frac{1}{2}\Delta V(t)\hat{Z}, \tag{4.18}$$

with U_0 and W_0 on-site and inter-site Coulombic interaction within the DBP$^-$. Also, $\mathbb{1} = |0\rangle\langle 0| + |1\rangle\langle 1|$ is the identity operator, and $\hat{X}$ and $\hat{Z}$ are the Pauli operators given by $\hat{X} = |0\rangle\langle 1| + |1\rangle\langle 0|$ and $\hat{Z} = |0\rangle\langle 0| - |1\rangle\langle 1|$.

Generalizing the above result, the Hamiltonian describing N number of DBP$^-$s is now expressed as an operator-sum that acts on and between DBP$^-$s:

$$\begin{aligned} \hat{H}(t) = &\left[N\left(3E_{\mathrm{os}} + 3\eta + U_0 + 2W_0\right) + \frac{9}{2}\sum_{\imath<\jmath}^{N} W_{\imath\jmath}^{+}\right]\mathbb{1} \\ &+ \sum_{\imath=1}^{N}\left[T\hat{X}_\imath + \frac{1}{2}\Delta V_\imath(t)\hat{Z}_\imath + \frac{1}{2}\sum_{\jmath<\imath} W_{\imath\jmath}^{-}\hat{Z}_\imath \otimes \hat{Z}_\jmath\right], \end{aligned} \tag{4.19}$$

where parameters $\imath$ and $\jmath$ denote DBP$^-$ sites, $\Delta V_\imath(t)$ denotes the time-dependent potential biasing, and T is the intra-qubit tunnel splitting energy. The inter-DBP$^-$ Coulombic repulsion is shown by $W_{\imath\jmath}$, where $W_{\imath\jmath}^{\pm} = W_{\imath\jmath}^{\mathrm{s}} \pm W_{\imath\jmath}^{\mathrm{c}}$ and $W_{\imath\jmath}^{\mathrm{s}}$ ($W_{\imath\jmath}^{\mathrm{c}}$) is the inter-site Coulombic interaction between the same (cross) sites of two DBP$^-$s. Also, we assume that intra-DBP$^-$ separation is constant. We emphasize that although the above Hamiltonian is derived for a system of DBP$^-$, it holds generally for any similar systems, such as those semiconductor systems made with any type of double-quantum-dot charge qubits.

The Hamiltonian given in Eq. (4.19) generates the unitary evolution of a system of DBP$^-$s, and thus it is responsible for the coherent dynamics of the system. However, this is true only if the system is completely isolated and it is not interacting with its surrounding environment. Coupling with the environment causes relative drift in the evolution of the system dynamics leading to its decoherence for which the above approach does not hold anymore.

4.4 Applications to quantum computation

For our DBP^- to be an effective charge qubit for quantum computation, it should satisfy at least DiVincenzo's five criteria [74] (see Sec. 2.4 for the criteria). We already discussed and estimated the tunneling rate and decoherence rates of the DBP^- as two of these criteria. In this section we discuss the rest of the DiVincenzo's criteria briefly, as complete fulfillment of the criteria is beyond the scope of our work.

Initialization of the DBP^- in the $|0\rangle$ state is performed by applying an electrostatic potential $\Delta V_i(t)$ so that the left DB is lower in energy thus attracting the pair's excess electron [13]. The electrostatic potential can be applied by means of an electronic gate such as an AFM or STM tip, or even a negatively-charged DB; see Sec. 3.1.3 for more details on biasing.

The amount of biasing should be large enough to dominate charge fluctuations in the electric gate. When initialization is complete, the electrostatic bias is eliminated, and tunneling between the two DBs commences. A lattice deformation due to charge localization is present during subsequent tunneling, but it is expected to relax at a much lower rate than Δ (by a few orders of magnitude), hence having a small decoherence effect.

In an experiment, application of a static potential (by a nearby negatively charged DB) has shown DBP^- polarization to be achievable [1]. In the same experiment, steps towards DBP^- readout were achieved by STM detection of the excess charge preferentially localized at one site in the DBP^-. This experiment thus shows that both state preparation on one side and readout of $|0\rangle$ vs $|1\rangle$ state is in principle feasible.

The Hamiltonian $H(t)$, Eq. (4.19), enables a universal set of gates [153]. A single-qubit gate can be implemented by varying the DBP^- tunneling rate by tilting the potential landscape by means of an applied bias then rapidly turning off the tilting. A second single-qubit gate that does not commute with the first one can be implemented by controlling an ancilla DBP^- nearby to the DBP^- of interest and letting the ancilla DBP^- affect the

evolution of the desired DBP$^-$ by Coulombic interaction. Similarly, for two-qubit gate we allow the two DBP$^-$ of interest to interact via Coulombic interaction, thus becoming entangled with each other. The time of interaction is determined by tilting one or two of the DBP$^-$s to control the position of the excess electron, or alternatively, by increasing the potential barrier between them.

The applied bias should have a timescale comparable with the tunneling rate of the DBP$^-$s. Since DBP$^-$s have fast dynamics, fast control is required for gate operations. Such fast and spatially precise control is beyond the current capability of standard electronics, but is in principle achievable by placing a suitable pattern of metallic nanowires near the surface and irradiating them with laser pulses. The laser pulse generates an electromagnetic discharge that biases the surface for a duration comparable to the duration of the pulse, which could be as short as femtoseconds. The laser carrier frequency should be low enough to avoid charging and discharging of DBs through excitation processes, thereby causing qubit losses. Different gates could be effected by time-varying biases achieved by controlled laser pulses.

Scalability of our surface DBP$^-$ quantum computing follows the same arguments as for the other proposed cases, but of course better understanding of small-scale devices is required to assess scalability to many-qubit devices. At this early stage, bearing in mind that many implementation details are in need of development, possible computing schemes appear to be: a four-rail flying qubit model analogous to the one for nuclear-spin qubits in bulk silicon [9], or a one-way quantum computer [154] where the qubits are stationary.

4.5 Summary

In this chapter, we demonstrated that a closely-spaced coupled DB pair (DBP$^-$) on the Si(100) surface is a potential candidate for charge qubit, as it shows excellent coherent dynamics due to its extreme miniaturization to the atomic realm. The excellent coherence is

a consequence of the fact that, based on our theoretical estimations, the tunneling rate is extremely high due to atomic-scale proximity of DBs, whereas the major source of decoherence scales weakly with DB-pair separation. However, we note that the scaling advantage comes at the price of having to achieve rapid gating control and measurement.

Furthermore, we developed a quantum computing architecture with DBP^- as its building block. To describe the quantum dynamics of such an architecture, we employed the extended Hubbard model and modified it in order to accommodate with our scheme of interest. The importance of this architecture lies in the fact that not only does it work with DBP^-s, but it is also compatible with other types of other semiconductor charge qubits. However, addressing all DiVincenzo's criteria in detail for such architecture will of course require more elaboration.

As the next step forward we believe that experimental characterization of the coherent dynamics of DBP^-s is of paramount importance, as it provides a way to test the theoretical estimations provided in this chapter. Due to the fast dynamics of DBP^-s, it is impossible to directly characterize DBP^- dynamics with conventional electronic tools. In Chap. 6, we propose a scheme to address this issue and to indirectly characterize DBP^-s coherent dynamics.

Chapter 5

Coherence of various DBP^- configurations: *ab initio* approach

In this chapter, we aim to develop a theory for characterizing energy splitting of coupled-DB pairs (DBP^-) for various DB-pair configurations and separations. We model the desired system by a Si cluster with the hydrogen-terminated Si(100)–2×1 surface, where two DBs are located on the surface and the DB-pair excess charge is provided by a P atom doped within the cluster. Energy splitting is a consequence of covalent bonding between the two DBs in a DBP^-; thus weaker bonding leads to smaller splitting. We employ *ab initio* density-functional theory (DFT) and time-dependent DFT techniques to calculate the energy splitting between bonding and antibonding states of the DBP^-.

Hydrogen-terminated Si(100)–2×1 is a well-patterned surface that has an anisotropic structure. The surface structure puts a constraint on the places where the DBs can be located. As a result, there is no continuous range of choice for DBs separation to explore DB-pair coupling strength and the information we obtain for energy splitting is quantized due to the structure of the surface. Coupled-DB pair can be used as the building block of more complex systems, such as DB nanowires and DB quantum cellular automata. Also, DBP^- has the potential to be used as a charge qubit for quantum computing. Hence, learning about the coherence of different DBP^- configurations helps in better understanding the effect of the surface structure on the construction of more complex systems on this surface.

As the cluster size, its edges, and the dopant position affect the calculated results, we explore the impact of these effects to find reliable models to use. Based on the results, we analyze the role of anisotropic structure of Si(100)–2×1 surface on the coherence of DBP^-s.

The chapter begins with Sec. 5.1 where we develop a cluster model for our system of interest. This section contains computational details (such as approximations used and limitations applied) about the clusters we built for modeling our desired system. In Sec. 5.2, the structure of the dangling-bond orbital is analyzed, which helps to understand the results presented in the following sections. In the next two sections, we develop an understanding on the effect of cluster size and dopant position by studying the convergence properties of the calculated results as a function of these factors. Any change in energy splitting less than 20% is considered as a good indicator of convergence.

In Sec. 5.3, we investigate the effect of cluster size and its surface edges on DBP^-s energy splitting. For each configuration, we use the minimum cluster size required to obtain reasonably reliable results while minimizing the computational-resources consumption. Similarly, in Sec. 5.4, we study the effect of dopant placement within the cluster on the calculated results. In Sec. 5.5, we test our results, presented in Sec. 5.4, by repeating the calculations where the dopant is replaced by an excess charge in the cluster model. We succeed in determining where the P atom should be placed within the cluster in order to behave like an excess charge for the DBP^-s. In Sec. 5.6, we analyze the effect of the Si-surface structure on DBP^- energy splitting. We learn that all DBP^- configurations can be put in four different groups, where each group has its unique behavior based on the arrangement of DBs. At the end, we wrap up this chapter with a summary on the main points and concluding remarks.

5.1 Cluster modeling of the Si system

A piece of silicon crystal can be modeled by a cluster, where the cluster is made from a lattice of a repeated cell. The cell is obtained by adequately replicating a cell of a section of Si crystal in the directions perpendicular to its surface; thus it consists of a few layers of silicon atoms. Repeated use of the cell leads to a cubic-shaped cluster; however for a Si cluster a pyramidal shape is desired because the unsaturated bonds on the surface edges of the cluster

should be fixed by hydrogen atoms for computational purposes, and the pyramid shape helps for having the bonds appropriately terminated without having H atoms overlapping each other. To shape the Si cluster to a pyramid, one can remove Si atoms such that the sides of the cluster have a (111) reconstruction. This also reduces computational costs compared to the cost associated with a cube of Si. Also, symmetrizing the cluster is another factor for reducing the need for computational resources. Therefore, an upside down pyramidal cluster is our desired model for a piece of Si crystal.

We use an energetically optimized cell, for which the structure was initially used for analyzing the change in the electronic properties of Si(100)–2×1 surface that was functionalized with organic molecules [155]. This cell is made of thirty-two Si atoms put in sixteen layers. The top layer has one Si-Si dimer where each Si is capped by a hydrogen (H); see Fig. 5.1. Duplicating this cell, one obtains a Si cluster with the H-terminated Si(100)–2×1 surface.

The resultant Si cluster is structurally optimized using a DFT-based method. In this process, all non-surface Si atoms are capped by hydrogens that are fixed in place and the position of the other atoms are optimized under this condition. The non-surface H atoms are fixed in order to simulate the bond connection to the rest of the Si atoms (in the crystal) that are not explicitly included in the cluster model. This ensures that the Si atoms in the cluster are less perturbed by truncation of the Si-Si bonds.

A phosphorous-doped Si crystal can be modeled by replacing one of the Si atoms located in the middle layers of the cluster with a phosphorous atoms. Dangling bonds can be created by removing some of the hydrogen atoms from the surface of the cluster. As the size of a cluster and consequently the number of atoms in the cluster increases, the amount of computing resources (i.e. processors, memory, and time) required for any type of calculation dramatically increase, and at one point it becomes unfeasible to perform the calculation. Therefore, it is essential to put some limitations on the desired cluster in order to make the computation practical. We use clusters with only one pair of DBs on the surface and one

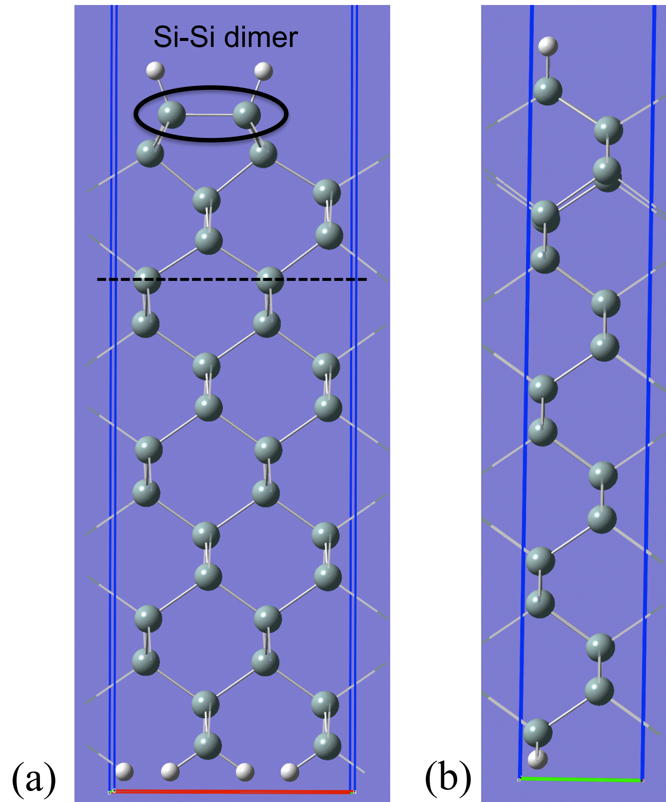

Figure 5.1: Ball-and-stick model of the Si cell with two views: (a) along and (b) across a Si-Si dimer. The green balls are silicon atoms and the white ones are hydrogens. This cell contains sixteen layers of Si atoms, where one of the layers is shown by a dashed-horizontal line. The Si-Si dimer on the top layer is framed by an oval box.

phosphorous (P) atom within the bulk. The P atom provides the excess electron for the DB pair. Such a cluster should be made symmetric to eliminate the possibility for the excess electron to become localized in one DB site.

There are some constraints on the location where P is allowed to reside within the cluster. The phosphorous atom should be in equal distance from both DBs to avoid symmetry breaking. It should not be in direct contact with the DBs to avoid complete bonding, thereby localizing the excess charge into the P-Si bond. Furthermore, P should be surrounded by Si atoms, so it can not be located on the cut edges. These constraints put a lower bound on the size of a Si cluster.

Based on the above constraints, the smallest cluster consists of three rows each with four Si-Si dimers. We study all possible DBP^{-} configurations on clusters of the size $n \times 4$ and

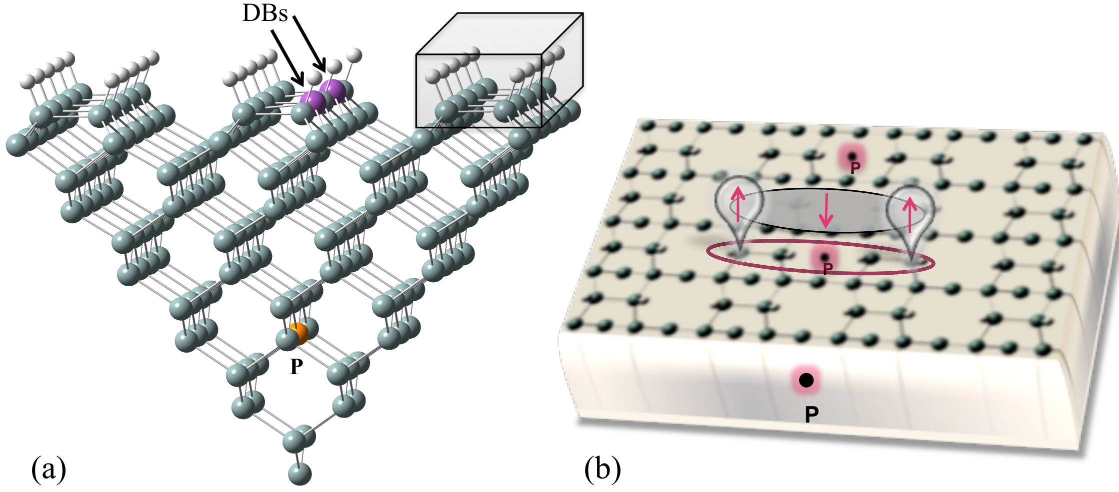

Figure 5.2: (a) A pyramidal cluster that is used for modeling a P-doped Si crystal with a coupled DB-pair on its surface. This cluster has three dimer rows each having five Si dimers. One of the dimer rows is framed by a box. The purple balls on the surface are the silicons that ended with a dangling bond. The DBs are created by removing hydrogen atoms. The orange ball within the cluster represents a phosphorous atom. (b) A schematic view of a coupled DB-pair, DBP$^-$, located on P-doped H-terminated Si(100)–2×1 surface. The bubbles represent DBs and the arrows represent electrons with spin up or down. Each DB originally owns a single electron, and both DBs share an excess electron provided by a doped phosphorous.

$3 \times m$, where $n \in \{3, 4, 5\}$ and $m \in \{5, 6, 7\}$, respectively. The parameter n is the number of rows and m is the number of Si dimers per row. Thus, the clusters are an extension of the smallest-size cluster either in the number of rows or in the number of dimers per row. The total number of atoms in these clusters (i.e. Si, H, and P) ranges from 243 to 443, corresponding to the smallest up to the largest cluster size, respectively. We categorize all the DBP$^-$ configurations to six groups. Each group contains only those configurations that belong to a particular cluster size.

Three types of DBP$^-$ configurations can be recognized based on the location of the two DBs. The'Vertical' configuration corresponds to the cases where DBs are located on the same side of one dimer row. The 'Horizontal' configuration occurs when DBs lay on a line

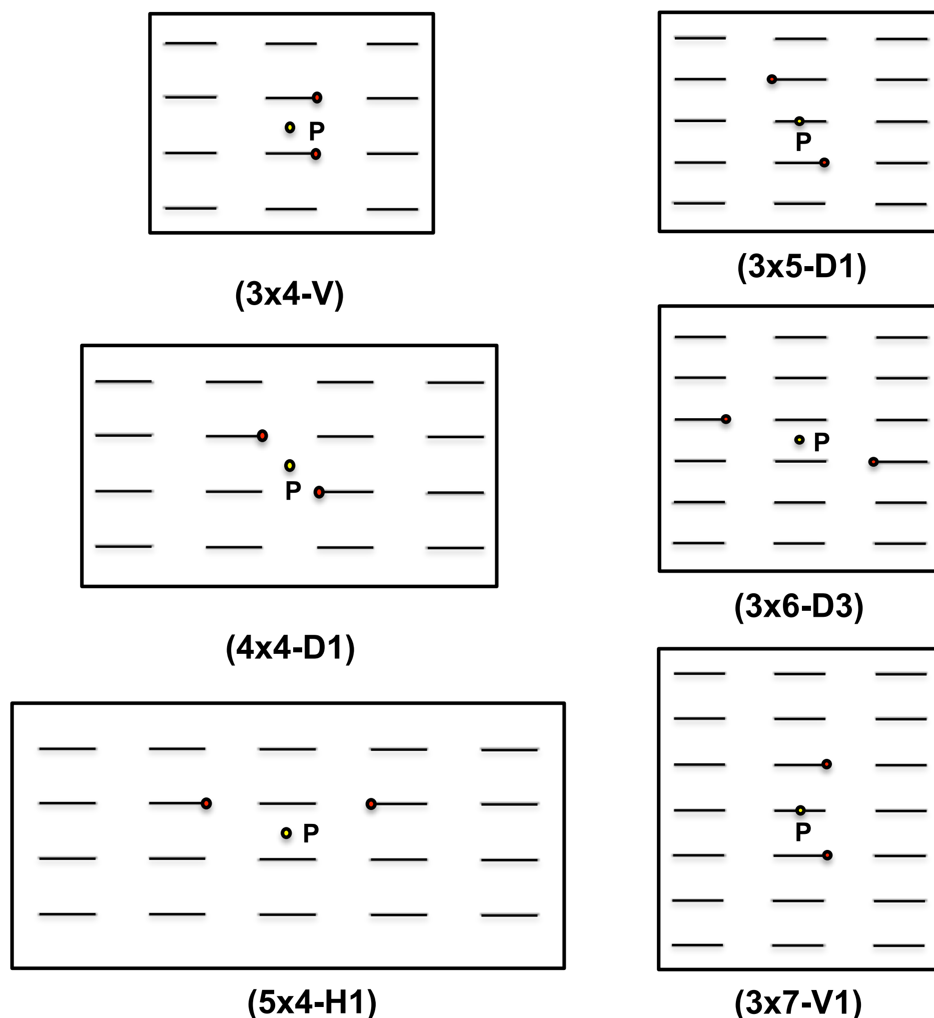

Figure 5.3: Six sample of DBP^{-} configurations each accompanied by its name, which is composed of the cluster size and the type of DBP^{-} configuration ('V' for vertical, 'H' for horizontal, and 'D' for diagonal) on that cluster accompanied by a number representing the increasing order of DB-pair separation. Each sample belongs to a particular cluster size. The boxes represent top-down view of hydrogen-terminated Si(100)-2$\times$1 surface and the horizontal short-lines represent Si-Si dimers. The DBs are shown by filled circles and the phosphorous atom doped within the cluster is shown by an open circle and the letter P. DBP^{-}s on these clusters have either vertical, horizontal, or diagonal configuration.

that is perpendicular to the rows. Any configuration other than these two we refer to it as a 'diagonal' configuration. We found a total of thirty-five DBP^- configurations on the cluster sizes mentioned above. Figure 5.3 shows a sample from each cluster size. All of the DBP^- configurations are given in Appendix A.

Each sample of a DBP^- is named by the cluster size it resides upon, accompanied by the DBP^- type of configuration. For a particular type of configuration, there might be more than one possibility for DBs separation. In such cases, the name ends with a number $x \in \{1, 2, 3\}$ representing the order by which DB-pair separation increases while symmetry is maintained, with $x = 1$ corresponding to the smallest separation. For instance, the name 3×5-D1 belongs to a DBP^- that is located on a 3×5 cluster size, has a diagonal configuration, and the DBs are separated by the 1st possible separation, determined by the surface structure; see Fig. 5.3.

We employed the Gaussian program [149, 156] on "Westgrid"[1] for computing the energy splitting of various DBP^- configurations. For each cluster, a Gaussian input file is prepared; Appendix B demonstrates a sample of the Gaussian input file. Computations are performed using the DFT-based method B3LYP/6-31G(d). This method has been employed in theoretical studies of various Si systems, and for some cases, the results are compared with experiment and show a good agreement in this respect [135, 139, 54, 133, 134, 132]. The conjecture is that this model gives reasonably good results for DBP^- energy-splitting calculations, as well. Nonetheless, one can improve the accuracy of the model by using a more accurate method and a larger basis set, but this will be at the cost of larger computational expenses.

5.2 Dangling-bond orbital

In this section, we analyze the structural properties of dangling-bond orbital, located on the Si(100)–2×1 surface. Learning about the shape and orientation of DB orbital leads to a

[1]Westgrid is a computing facility that is part of the Compute Canada Consortium.

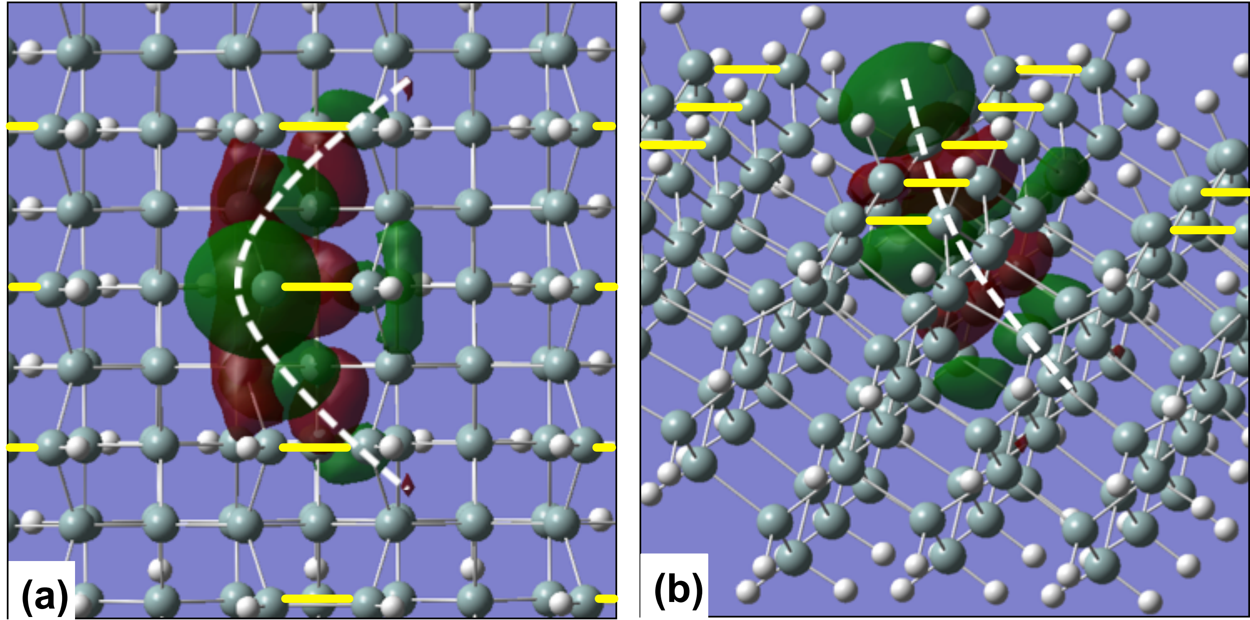

Figure 5.4: Representations of the dangling-bond orbital on hydrogen-terminated Si(100)-2×1 surface obtained from a DFT calculation (a) top-down view of the DB orbital and (b) the view along the surface dimer rows. In both images, Si and H atoms are shown by gray and white balls, respectively. The green and red portions of the orbital are representing the relative phases of the dangling bond orbital. The dimers are shown by short-yellow lines. The orientation of the dangling-bond orbital above the Si surface and within the substrate are shown by dash-curved lines.

better understanding of the coupling strength between DBs. Figure 5.4 shows a dangling-bond orbital from two different perspectives: (a) the top view and (b) the view along the dimer rows.

The dangling-bond orbital is a p-type orbital; hence it has two lobes. One lobe projects out of the surface and is oriented away from the corresponding Si dimer. This lobe is surrounded by the vacuum above the surface, and is mostly confined in a space less than 5 Å in radius; see Fig. 5.4 (b). The other lobe is distorted and is spread through the Si substrate. This lobe is made of portions with two different phases, which are shown by green and red in Fig. 5.4. Each phase is a consequence of the way the atomic orbitals are interacting with each other in order to build the orbital associated with the DB.

The lobe of the DB orbital that is spread through the Si substrate is curved in two

directions: (1) the direction parallel to the surface and along the corresponding row and (2) the direction perpendicular to the surface as the lobe spreads through the substrate. The portion of the lobe that is near the surface is extended away from the DB's location and is curved towards the opposite side of the corresponding row; see Fig. 5.4 (a). Also, as Fig. 5.4 (b) shows, the lobe bends towards its corresponding dimer row, as it roots into the Si substrate.

Figure 5.4 also demonstrates that the DB orbital is more extended along the dimer row than across it. This is expected as each row of Si dimers is surrounded by relatively large gullies of vacuum on both sides, which limits the spread of the DB orbital in that direction. This also matches with experimental observations of a DB spatial extension that is reported recently [31]. Knowing the structure of dangling-bond orbital is valuable in analyzing the effect of the Si(100)–2×1 surface structure on the coupling of DB pair, as it will be shown in the following sections.

5.3 Effect of cluster size and surface edges on DBP^- energy splitting

The size of the cluster used for modeling our system plays a crucial role in the accuracy of the calculated results. While the cluster size should not be too small to avoid results with large error, it can not be too large due to resource limitations (especially the computation time), so there is a lower and upper bound on the size of the cluster. However, between these two bounds, as the cluster size gets larger it is expected that the value of energy splitting for each DBP^- configuration converges to its asymptotic value[2], because there will be enough space on the cluster surface to investigate a desired configuration without positioning the DBs very close to the surface edges.

We address the effect of cluster size on energy splitting by studying each DBP^- configuration on different sizes of clusters and checking the variation in the calculated results. Once

[2] By 'asymptotic value' we mean the results that one would get if the desired DFT method and basis set was applied to an infinite-size Si cluster

the results converge and hardly change, we claim that the corresponding cluster has the appropriate size for modeling our system. As the DBs are located on the surface, in addition to cluster size, the edges of the surface can also affect our results. This is especially true for those DBP^- configurations in which DBs are closer to the surface edges. Thus, in this section we develop an understanding of how much these two factors impact our calculated results.

Among our collected data, those that meet the above condition are listed in Table 5.1. This table contains the name of the clusters as well as the DB-pair separation and the energy splitting associated with each cluster. There are seven sets of data in this table, each set corresponding to a single DBP^- configuration located on clusters that vary in size. Clusters in each set are extensions of the smallest-size cluster in that set either in the number of rows or the number of dimers per row.

The first two sets correspond to the vertical configuration. In the first set, the two DBs are separated by one dimer spacing. The energy splitting in this set is within 15.2 meV (i.e. 5.4%) of the average value of 322.9 meV for this configuration. For the second set, the DBs are two dimer spacings apart, and the energy splitting is within 18.3 meV (i.e. 17.25%) of the average value 106.1 meV for this configuration.

For the DBP^- configurations in the first two sets, energy splitting increases as the size of the cluster increases. The increase of energy splitting with respect to the cluster size is suggesting that the overlap between the two DBs wavefunction becomes larger with the cluster size increment. The splitting increase can be partially justified using basic quantum physics intuition. Considering a single particle in a finite-potential well with barriers of different widths, the particle wavefunction decays faster on the barrier side that is wider [157, 158, 159]. Thus, for the particle ground-state wavefunction it looks as if the wavefunction is shifted towards the side of the well with narrower barrier, which implies that the particle is more likely to tunnel through the barrier with smaller width.

Cluster name	DB-pair separation (Å)	Energy splitting (meV)
3×4-V	3.78	307.7
4×4-V	3.87	329.2
5×4-V	3.87	326.7
3×6-V1	3.87	338.0
3×5-V	7.73	87.8
3×7-V1	7.74	124.4
3×5-H2	13.00	16.9
3×7-H	13.14	28.0
5×4-H1	12.88	44.4
3×4-D1	4.65	81.8
5×4-D1	4.63	83.4
3×6-D1	4.63	79.6
3×5-D1	8.16	44.3
3×7-D1	8.16	35.7
3×4-D2	13.65	35.9
5×4-D2	13.45	32.6
3×6-D3	13.68	32.4
3×5-D2	15.13	16.6
3×7-D3	15.25	15.0

Table 5.1: Seven sets of clusters, each corresponding to a particular DBP^- configuration. The sets are separated from each other by thick-black lines. This table contains the name of the clusters, DB-pair separation in that cluster (in Å), and the corresponding energy-splitting (in meV). The first two sets correspond to vertical configuration, the next set corresponds to horizontal and the four other sets are diagonal configurations. The clusters are named by $n \times m - Cx$ where n, m and C stand for rows, dimers per row, and DBP^- configuration, respectively. Some of the clusters' name end with a number x representing the order by which DB-pair separation increases for that particular configuration, with $x = 1$ corresponding to the smallest separation.

Analogously, each DB in a DBP^- (i.e. an excess electron shared between two DBs) can be considered as a finite potential well with barriers that can have different widths. The width of the barriers is defined either by the separation distance between the DBs in the DBP^-, or the distance between each DB and the Si-surface edges. For a DBP^- on a cluster, if the distance between each DB and the surface edges gets larger than the separation distance between the two DBs, the excess-electron wavefunction tends to shift towards the potential barrier between the two DBs. Shifting of the electron wavefunction results in a larger overlap with a concomitantly larger energy splitting for the DBP^-.

We expect that there is a turning point after which any more increase in the distance between DBs and surface edges would not have a noticeable effect on the amount of splitting. Therefore, as the cluster continues to get larger the change in energy splitting for a particular DBP^- configuration becomes smaller and the splitting approaches an asymptotic value.

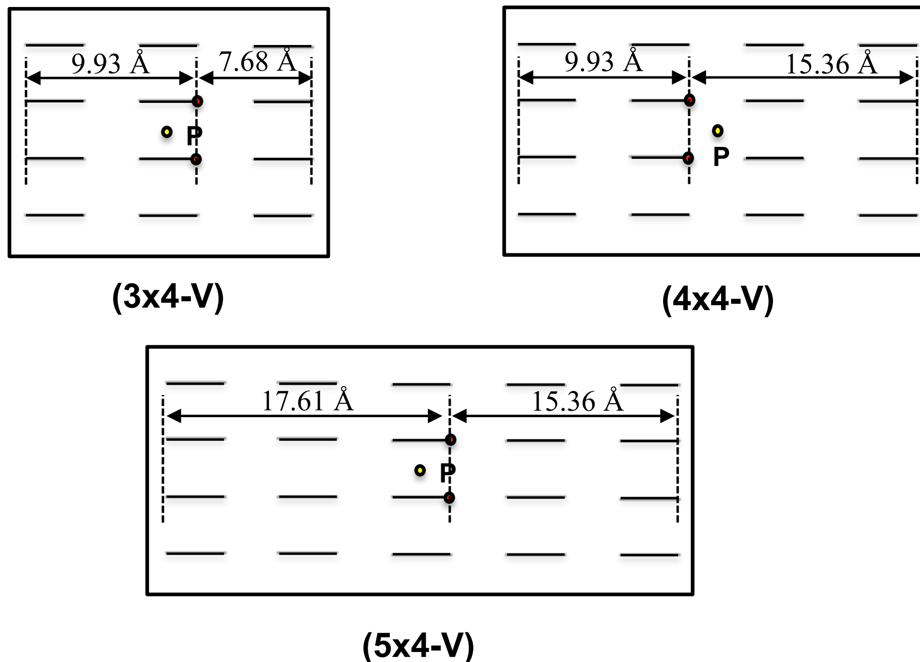

Figure 5.5: Separation distances of DBs from 'left' and 'right' surface edges on 3×4, 4×4, and 5×4 clusters. The boxes represent top-down views of hydrogen-terminated Si(100)-2×1 surfaces and the horizontal short-lines represent Si dimers. The DBs are shown by red circles and the phosphorous atom doped within the cluster is shown by a yellow circle and the letter P. The letter 'V' stands for vertical configuration (of DBP^-).

The first set of data in Table 5.1 shows that there is a significant discrepancy between energy splitting associated with the smallest cluster, i.e. 3×4-V, as compared to the splitting of the other clusters in the set. Based on the spatial extension of the DB orbital (explained in Sec. 5.2) and the basic explanation given above, this large discrepancy can be partially justified by pointing out that the distance between each DB and the closest edge is comparable to the DB-DB separation. This noticeable change suggests that the splitting on 3×4-V is strongly affected by the size of the cluster and its surface edges. Similarly, we conclude that the splitting for the smallest-size cluster in the second set, i.e. 3×5-V, also results from the same effects.

A comparison between the results in the first set shows that increasing the number of Si-dimers per each row has a dominant effect (as compared to increasing the number of rows) on the splitting of DBP^{-}s with vertical configuration. In other words, there is a larger change in splitting when the cluster size increases from 3×4 to 3×6 compared to when the size increases from 3×4 to 4×4 and 5×4. This implies that those surface edges perpendicular to dimer rows have more effect on splitting than those edges parallel to the rows. This could be an indication of greater extension of the DB wavefunction in the direction of the rows which is consistent with the description of DB orbital given in Sec. 5.2. More data is required to check whether the splitting value is converged for the cluster size extended along the rows. However, comparing the splitting value for 3×6 with the ones for 4×4 and 5×4 is suggesting that this splitting value is likely to be converged.

Also, a closer look at the first set may raise the question of why there is a large difference between energy splitting of 3×4-V as compared to 4×4-V and 5×4-V, while in all three cases the DBs have the same distance from their closest surface edge. Although in these clusters the DBs have the same distance from surface edges crossing the dimer rows, their distance from the two edges parallel to the rows are different from one cluster to the other; see Fig. 5.5. In 3×4-V, the DBs are closer to the 'right' edge by 2.25 Å as compared to the

'left' edge, whereas in 4×4-V, the distance between the DBs and the 'right' edge is doubled by adding an extra row of Si dimers. Furthermore, in 5×4-V an extra row is added to the left side of the DBs, but it does not affect the splitting significantly as compared to 4×4-V.

These comparisons suggest that, in the case of vertical configurations, the optimum distance to consider between DBs and those edges parallel to the Si-dimer rows is 9.93 Å, which is equivalent with two Si dimers separated by a vacuum gully; see Fig. 5.5. For smaller distances the results are not converged to the asymptotic value as a consequence of edge effects (similar to the case of 3×4-V), and for larger distances the value of splitting does not changing significantly (similar to the case of 5×4-V). Therefore, the best cluster model to use for vertical configurations in order to have the lowest of computational resource usage while getting asymptotically converged results is a cluster with four rows of Si dimers.

The third set in Table 5.1 corresponds to a horizontal configuration. In this set, DBs are one row apart; thus between the two DBs there is two vacuum gullies separated by a Si dimer. The energy splitting for the clusters of this set is within 13.7 meV from the average value 30.7 meV. Similar to the results for vertical configurations, we see that for the horizontal configuration the splitting increases with cluster-size increment. Hence, the justification given earlier is also valid for this case. As a result, the splitting for 3×5-H2 is affected more from the crystal-size effect than 3×7-H and 5×4-H1.

We notice that in this set of data the larger change in splitting occurs when the smallest cluster in the set gets larger by adding extra rows. This implies that splitting associated with horizontal configurations is affected more by the number of rows while for vertical configurations the splitting depends more on the number of dimers per row. Nonetheless, in this set, it remains unclear whether the splitting would converge as we go to larger cluster sizes. However, if the argument about keeping DBs 9.93 Å away from 'left' and 'right' edges also holds for horizontal configurations, then we expect that going to clusters with more rows would not change the splitting significantly with respect to the splitting associated

with 5×4-H1.

Finally, the last four sets in Table 5.1 correspond to DBP^-s with diagonal configurations. In the first two sets, the DBs are on the same row but opposite dimer sides, while for the other two sets the two DBs are located on different rows. The energy splitting associated with each of these four sets (from the first one to the last) are within 2.5%, 10.8%, 6.8%, and 5.1% of their average values, respectively. Thus, for diagonal configurations, the effect of cluster size and its surface edges on the splitting of DBP^-s seems insignificant, as the results in each set are quite close to each other.

A comparison between the first (second) set of vertical and the first (second) set of diagonal configurations shows that the energy splitting drops by $\approx 25\%$ while there is only a slight increase in the DB-pair separation (≈ 0.75 Å). The reason behind this dramatic drop is due to the orientation of the DBs orbital; see Sec. 5.2. More details on this point will be given in Sec. 5.6, but for the sake of argument here, we point out that larger splitting is due to larger overlap between the two DBs wavefunction, which in turn is influenced by the orientation of the DBs orbital.

5.4 Effect of phosphorous location on DBP^- energy splitting

Use of explicit phosphorous (P) dopant in a cluster is another factor affecting the calculated results. A dopant atom provides the excess electron for the coupled-DB pair. The phosphorous atom should not be in direct contact with the DBs to avoid any bonding. To fulfill the former condition, we locate P a couple of Si layers below the cluster surface. The later is not a problem for small-size clusters as the size of cluster would limit the allowed location for the dopant.

To examine the effect of P location on the DBP^- energy splitting, we choose a cluster large enough to accommodate the dopant in three different positions. Figure 5.6, shows the desired cluster made of 578 atoms. The two DBs on the surface are separated by two dimer

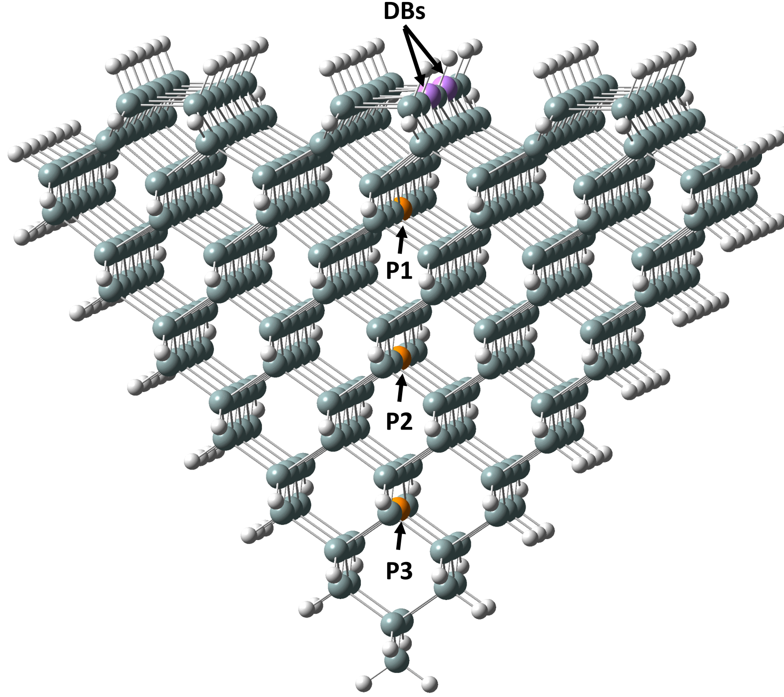

Figure 5.6: A 3×7 cluster made of 578 atoms. The two DBs are shown with purple balls on the surface of the cluster. The three positions that P can be doped in this cluster are shown by orange balls and named by Px where $x \in \{1, 2, 3\}$.

spacing, which results in DB-pair separation distance of ≈ 7.72 Å. For the three locations shown in Fig. 5.6, the dopant P is 5.83 Å, 10.46 Å, and 15.66 Å away from each DB. The energy splitting associated with these P-DB separations are 131.54 meV, 116.06 meV, and 115.75 meV, respectively. These values are within $\approx 8.6\%$ of the average value.

We see that when P is moved from P1 to P2 in Fig. 5.6, the energy splitting drops by ≈ 15 meV, while it only changes by ≈ 0.31 meV as the dopant is moved from P2 to P3. The change from P1 to P2 is significant and it suggests that Coulomb effects are quite large and distort the splitting energy.

In all of our clusters, P dopant is located within 8 to 16 Å away from both DBs, so the effect of P location on DBP$^-$ energy splitting is likely to be insignificant. It should be noted though, while positioning P at the position P1 is not suitable for our modeling, it does not mean that the calculated result does not have value. For instance, with the recent experimental achievements in controlling dopant position within the Si substrate [16, 17], it

is in principle possible to benefit from varying P location within the Si substrate in order to control DBs coupling. Nevertheless, for our particular purpose of understanding the impact of dopant placement, we can not rely on this location of P.

5.5 Replacing phosphorous dopant by an excess charge

In assessing the effect of P location on energy splitting, we noticed that for dopant placement beyond certain depth, there is only a small difference between the resultant energy splittings. This small difference can be an indication that splitting is converging to a specific value. The little change in splitting might also suggest that for P-DB separations beyond certain distance, dopant P looks like an electron to our system of DB pair. In this section, we put this conjecture to the test by replacing dopant P with an extra charge and checking whether this replacement would significantly change the energy splitting.

We choose a cluster with a surface comprised of four rows, each having four dimers, and evaluate energy splitting for all possible DBP^- configurations on this surface both in the presence and in the absence of explicit dopant P. In the case where there is no explicit dopant in our clusters the charge of the corresponding model is manually increased by one. The results obtained from both approaches are given in Table 5.2.

Table 5.2 contains clusters name, DB-DB and P-DB separations, and energy splitting associated with each DBP^- configuration that is calculated in the presence of a P dopant or an excess electron. The results show that the splitting obtained by these two approaches for each configuration are quite close to one another. The similarity of the splittings confirms that for dopant placement beyond certain amount ($d_{\text{P-DB}} \gtrsim 8$ Å) the P atom behaves as if there is only one extra electron in our cluster model. This result also indicates that the DBP^- excess-charge, hosted by the dopant, is not bonded to P atom and is delocalized between bonding and antibonding states of the coupled DBs.

It should be noted that for small-size clusters, using an extra charge might induce sig-

Cluster name	DB-pair separation (Å) / P-DB separation (Å)	Energy splitting (meV) (in presence of P)	Energy splitting (meV) (in presence of excess charge)
4×4-V	3.87/8.90	329.2	333.2
4×4-H1	5.19/8.92	34.9	33.4
4×4-D1	6.45/9.97	56.1	52.8
4×4-H2	10.29/13.39	37.6	31.6
4×4-D2	10.99/8.93	52.8	54.1
4×4-H3	20.65/9.96	34.1	33.3
4×4-D3	21.00/13.39	9.9	11.9

Table 5.2: Energy splitting for all possible DBP$^-$ configurations on cluster 4x4 in the presence and in the absence of dopant P within the cluster. Separation distance between DBs in a pair as well as the distance between P and each DB are given in the second column. The third and fourth columns correspond to the energy splittings, calculated in the presence of dopant P and when P in the model is replaced by a silicon atom plus an excess charge.

nificant perturbation to the system. On the other hand, for larger clusters using the charge might help to prevent various limits that the dopant is facing (i.e. being equidistant from both DBs, avoiding direct contact with DBs and also the cut edges). These constraints put a lower bound on the size of a Si cluster. Therefore, as the results of these two approaches are not significantly different, employing P is preferred for small-size clusters while an excess charge is more compatible with large-size clusters.

5.6 Effect of the Si-surface structure on DBP$^-$ energy splitting

In this section, we elaborate on the effect of the Si(100)–2×1 surface structure on DBP$^-$ energy splitting. For this purpose, the collected data on energy splitting is categorized into four sets, each corresponding to a specific DBP$^-$ configuration. For some of the DBP$^-$s more than one result is available, corresponding to different cluster size. We only consider those splitting values that correspond to the largest-size cluster, in the hope of minimizing the effect of cluster size on the calculated results. The values that are not included here are reported in Sec. 5.3 for the purpose of analyzing the effect of cluster size and surface edges on DBP$^-$ energy splitting.

The four sets of data, each corresponding to a specific configuration, are given in Table 5.3. Each set is separated from the neighboring ones by thick lines. The table contains the name of the clusters, DB-pair separation and the energy splitting associated with each cluster. The sets are arranged in the order of vertical, horizontal, diagonal (DBs-on-same-row), diagonal (DBs-on-different-rows) configurations, and the data in each set is sorted by increasing in DB-pair separation.

As expected, the value of energy splitting in each set decreases as the DB-pair separation increases. However, a more careful look at all the sets shows that for comparable DB-separations, vertical and diagonal (DBs-on-same-row) configurations lead to higher energy splitting than the other two configurations. Furthermore, comparing the splitting values in the first set with the ones in the third set clearly shows that for comparable DB-pair separations the splitting values are significantly larger for the vertical configuration as compared to the diagonal case. In the following, we justify these behaviors based on the shape and orientation of DB orbital and the structure of the surface.

Considering vacuum gullies between dimer rows, which separate each row from the neighboring ones, we expect to see larger energy splitting when the two DBs are located on the same dimer row as compared to the cases where the DBs are on different rows. This is due to the larger degree of overlap between the two DBs wavefunction located on a single row. Thus, for comparable DB-pair separations it is reasonable that the DBP^{-} energy-splitting for vertical and diagonal (DBs-on-same-row) configurations to be higher than horizontal and diagonal (DBs-on-different-rows) cases.

For the two DBs located on a single row, due to the orientation of the upper-lobe of the DB orbital (see Fig. 5.4) we expect to see larger energy splitting for vertical configuration as compared to the diagonal (DBs-on-same-row). This is related to the degree of overlap between the DBs wavefunction. In the case of vertical configuration, the upper-lobe of the two DBs are oriented in the same direction, whereas for the diagonal case the lobes are

Cluster name	DB-pair separation (Å)	Energy splitting (meV)
3×6-V1	3.87	338.0
3×7-V1	7.74	124.4
3×6-V2	11.64	93.8
3×7-V2	15.52	66.9
5×4-H1	12.88	44.4
5×4-H2	18.02	25.9
5×4-H3	28.38	14.8
3×6-D1	4.63	79.6
3×7-D1	8.16	35.7
3×6-D2	11.91	71.0
3×7-D2	15.73	34.9
5×4-D2	13.45	32.6
3×7-D3	15.25	15.0
3×6-D4	17.51	15.2
3×7-D4	20.29	9.9

Table 5.3: Four sets of clusters are available in this table separated from the neighboring ones by thick-black lines. From top to down, the sets correspond to vertical, horizontal, diagonal (DBs-on-same-row), and diagonal (DBs-on-different-rows) configurations, respectively.

pointing away from each other. Thus, we expect to have stronger bonding between the two DBs in vertical configuration and consequently larger splitting.

For further analysis, the data in Table 5.3 is visualized by a log-line graph, shown in Fig. 5.7. The logarithmic axis corresponds to the DBP^- energy splitting and the linear axis shows the DB-pair separation. This graph contains four plots, each corresponding to a set of data, listed in Table 5.3. In all of the four plots, energy splitting is apparently decreasing as a function of DBs separation, but the type of regression in these plots needs further consideration.

We notice that the plots corresponding to both vertical and horizontal configurations are *close to* linear, which implies that energy splitting for these two types of configuration changes *almost* exponentially as a function of DB-pair separation. The reason for not having completely-linear plots might be related to the shape of the dangling-bond orbital. In a coupled-DB pair, those lobes of the orbital that are above the surface overlap in the vacuum

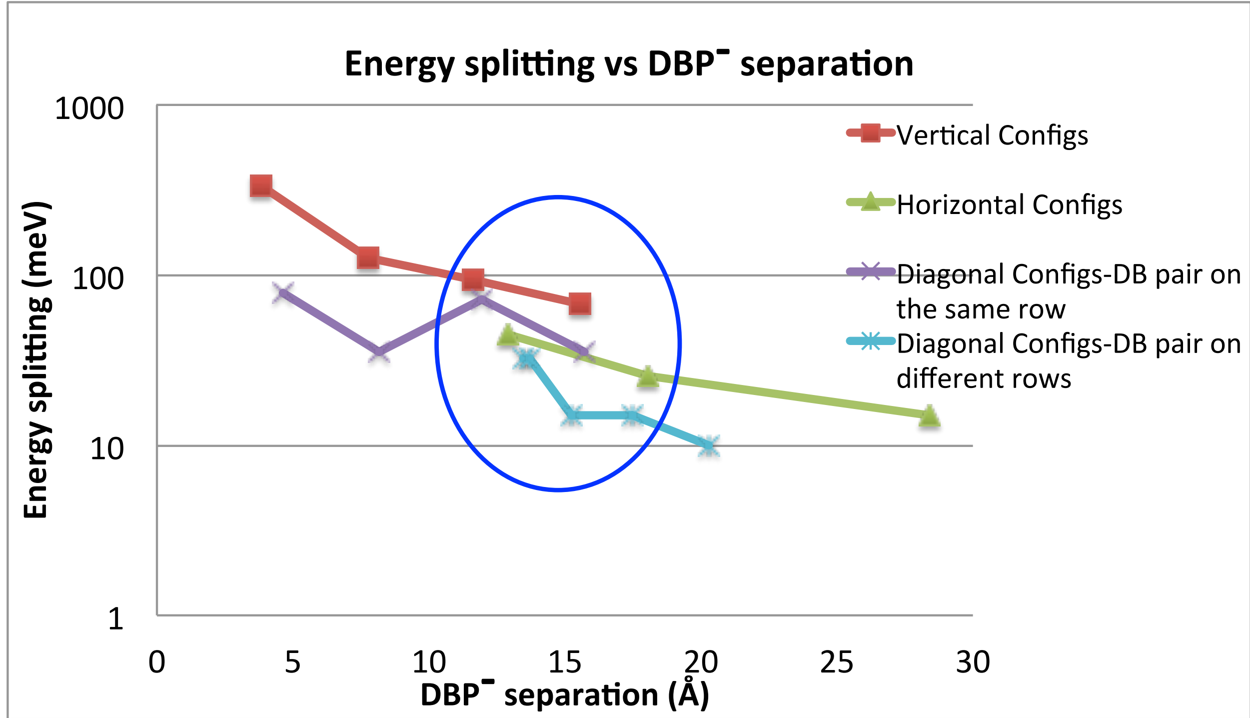

Figure 5.7: Log-line graph of DBP$^-$ energy splitting (meV) as a function of DB-pair separation (Å). Each plot corresponds to a specific DBP$^-$ configuration, i.e. vertical, horizontal, diagonal(DBs-on-same-row), and diagonal(DBs-on-different-rows). For vertical and horizontal configurations, the trend is almost linear, indicating that energy splitting for these two configurations varies almost exponentially as a function of DB-pair separation. Diagonal configurations behave somewhat differently than vertical and horizontal configurations. The circle highlights the part that DB-pair separation in different configurations are comparable with each other and indicates how configuration of DB pairs would affect their splitting.

space while the other two lobes overlap within the Si dielectric medium. Thus, although the overlap between the surface lobes as well as the ones in the substrate might each behave exponentially as a function of DB-pair separation, but each part has its own decay rate due to different environments. As the coupling strength in a DBP$^-$ is a consequence of the overall overlap between the two DBs orbital, the energy splitting is partially affected by the Si material between the two DBs.

In Fig. 5.7, another point to notice is that the plots associated with both types of diagonal configuration behave somewhat similarly. This similarity is despite the fact that surface structure between the two DBs changes significantly as we go from DB pair on the

same dimer row to DBs on different rows. Furthermore, these two plots look different from those corresponding to vertical and horizontal configurations, which implies that the change of energy-splitting versus DB-pair separation can not be easily predicted for this type of configuration.

Although for diagonal configurations the changing pattern in DBP^- splitting is legitimate in the framework of the theory we used, at this stage this behavior is not yet well understood and requires further investigation. However, we suggest that this pattern may be related to the overlap of different parts of the two DB orbitals and whether the overlapping parts are in-phase or out-of-phase; see Fig. 5.4.

In general, overlap between in-phase atomic orbitals leads to constructive bonding with an energy that is lower than that of the original orbitals. If the two overlapping orbitals are out-of-phase, the overlap results in antibonding orbital with an energy higher than those of the original atomic orbitals. The splitting values reflect the overall degree of overlap between DBs.

As the last point of this section, we suggest that the changing rate of energy splitting versus DBs separation should be different from one configuration to the other, because the surface structure between the two DBs is different for each configuration. However, more data is required to check this suggestion and we need to use larger clusters to accommodate DBP^-s with larger DB separation. For example, for the horizontal configuration, the next cluster should be 7×4 which contains 200 atoms more than 5×4; see Table 5.3. This dramatic increase in the number of atoms requires a considerable amount of computational resources (especially time), which one needs to consider if willing to collect more data.

5.7 Further discussion on the computed results

The results presented in this chapter provide some insights into the effect of the surface structure and the dopant position on the strength of DBs coupling. The converged results

are indicative of what to expect in a relevant experiment. This information becomes quite useful when dealing with DBs in more complex nano-systems such as quantum cellular automata, DB sub-nanowires, and quantum computing schemes.

We learned that for comparable DB-pair separations, those pairs located on the same row display significantly stronger coupling than those located on different rows. In addition, for DBP^-s with DBs located on different rows, those that are in the horizontal configuration displays stronger coupling than those in the diagonal configuration. This is especially useful when dealing with more complex systems built from DBs. One can benefit from this fact by positioning DBs on different rows for reducing undesired coupling while keeping coupled DBs on the same row. The coupling strength between the DBs in a coupled-DB pair can then be controlled by adjusting the separation distance between them.

Furthermore, the relative orientation of DB orbitals plays a crucial role in the strength of DBs coupling. For DBs located on the same row, there is a significant amount of change in the splitting value depending on whether both DBs are on the same side or on different sides of their corresponding dimer. Therefore, for more complex systems one can benefit from this factor as it provides an alternative way for controlling DBs-coupling strength.

Based on our analysis presented in the previous chapter (in Fig. 4.2), the phonon-induced decoherence for DBP^-s with a DB separation within 3.84 to 20 Å ranges from 0.1 to 1 meV. On the other hand, our calculated results show that the minimum amount of energy splitting is 9.9 meV, which belongs to a DBP^- with diagonal configuration where DBs are located on different rows and are 20.29 Å apart. The other values of splitting are at least one order of magnitude larger than the range of decoherence given above. Therefore, for quantum computation with DBP^-s, the distance between DBs should not exceed 20 Å as the decoherence induced by the crystal phonons would dominate the coherent dynamics of the DBP^-.

In addition, the spatial precision that can be achieved for implanting a P atom within

the Si crystal is of paramount importance. The dopant P should be equidistant from both DBs. Otherwise the excess charge will be localized in the DB that is closer to the P atom, consequently leading to the loss of usability of the DBP^-. Furthermore, the coupling strength of the DBP^-s is a function of the dopant's depth. Therefore, any variability in the dopant placement within the crystal results in variation of the coupling strength. The depth of P atoms can also affect the Coulombic interaction between neighboring DBP^-s, which is important to note if one aims to generate coupling between neighboring DBP^-s.

Considering the above points, the placement of a P atom with respect to a DBP^-, are especially important when dealing with complex systems that should be made of *identical* DBP^-s (e.g. a quantum computing architecture). Recently, it has been experimentally shown that a P atom can be deterministically positioned within a Si crystal with a lateral spatial accuracy of 3.8 Å, i.e. one lattice site [16, 17]. Therefore, embedding P atoms in selective locations within the Si substrate is now feasible.

However, for a more complex system (such as a quantum computing architecture) in which several donors (or arrays of donors) is required, perfect control over the lateral positioning of P atom is still beyond reach. Also, the accuracy of the P location with respect to the crystal surface (in other words dopant's depth) is still a concern. Therefore there are some errors resulted from imperfections associated with the process of implantation of P atoms.

5.8 Summary

In this chapter, we characterized energy splitting for a wide variety of DBP^- configurations and DB-pair separations, located on the Si(100)–2×1 surface. This surface has an anisotropic structure; thus the energy splitting of a DBP^- strongly depends on the location of the constituent DBs. We developed an appropriate cluster for modeling a piece of Si crystal with a coupled-DB pair on the surface that share an excess charge provided by a dopant atom. We analyzed the structure of a DB orbital, which helped to have a better understanding of

the effect of the surface structure on DBP^- energy splitting. Our analysis showed that all the DBP^- configurations can be categorized to four groups such that each group behaves differently from the others.

Furthermore, we developed an understanding of the impact of cluster size, its surface edges, and P dopant position on the value of energy splitting. We analyzed the role of cluster size as well as its surface edges by studying convergence in DBP^-s energy splitting as a function of cluster size. For the impact of dopant position, we determined where to place the P dopant within a cluster in order to avoid strong Coulombic interaction with the DB pair. Also, we learned that for the dopant far enough from DBs, a P atom behaves like an excess electron in our cluster models.

It is worth noting that for a couple of the data sets presented in this chapter, they would benefit from more data for more rigorous analysis. Specifically, for the cluster-size effect on the value of splitting, although the convergence has been met for most of the configurations, there were a few cases that we still need to go to larger cluster sizes and run more simulations in order to fulfill the convergence criteria. In addition, we need more data to determine the changing trend of energy splitting as a function of DBs separation for all four categories of DBP^- configurations. Addressing these issues are considered as near-future work, because successful termination of each running simulation will take several months.

Chapter 6

On Measuring Coherence in Coupled Dangling-Bond Dynamics

In this chapter, we propose a scheme to characterize the tunneling rate and coherence of the excess-charge shared by a coupled DB pair (DBP^-). Our theoretical estimations, given in chapter 4, indicate that the charge dynamics is highly coherent but too fast to be measured by any straightforward method. Our strategy is to measure the time-averaged charge distribution of the DBP^- by capacitively coupling the pair to an atomic force microscope (AFM) while the pair is imposed to a DC bias and concomitantly driven by a mid-infrared (MIR) field. When the MIR field becomes resonant with the biased DBP^-, resonant peaks appear in the AFM read-out from which the DBP^- excess-charge tunneling rate as well as the nature and rate of decoherence can be revealed.

This chapter begins with Sec. 6.1 containing a detailed description of the theory we developed for our scheme. In this section, we first analyze the role of an applied static bias and a mid-infrared field on the dynamics of a DBP^-, as well as the combined action of both elements on the system, thereof. Also, the effect of laser heating on our system is discussed in this section. In Sec. 6.2, we model the capacitive coupling between an AFM tip and the DBP^- by considering all the dominant forces acting between the tip and the system. In Sec. 6.3, we consider the effect of noise on our system and analyze the decoherence rate of DBP^- excess charge accordingly. We summarize this chapter by listing the main points.

The content of this chapter is the result of a collaborative work that is published in Physical Review B. In this work, I devised the scheme and developed the theory. However, in the process of improving the work, the theory was polished to a nicer and more simplified form with the help of our collaborators. The analysis of laser heating effect in the Physical

Review B paper was done by collaborators and it is not included in this chapter.

6.1 Dangling bond pair under static bias and driving laser field

In this section we discuss technical issues concerning each component of the proposed apparatus. This apparatus is shown in Fig. 6.1 and described in detail in the figure caption.

6.1.1 Static bias

The free Hamiltonian for uncoupled DBs is given by $E_{0,\mathrm{L}}|\mathrm{L}\rangle\langle\mathrm{L}|+E_{0,\mathrm{R}}|\mathrm{R}\rangle\langle\mathrm{R}|$, for $E_{0,\mathrm{L}}$ and $E_{0,\mathrm{R}}$ the on-site energies plus local field corrections for the left and right DBs, respectively. We assume that $E_0 \equiv E_{0,\mathrm{L}} = E_{0,\mathrm{R}}$ (a symmetry condition). The Hamiltonian for coherently coupled DBs is

$$\hat{H}_0 = E_0 \left(|\mathrm{L}\rangle\langle\mathrm{L}| + |\mathrm{R}\rangle\langle\mathrm{R}|\right) + \frac{\hbar\Delta}{2}\left(|\mathrm{R}\rangle\langle\mathrm{L}| + |\mathrm{L}\rangle\langle\mathrm{R}|\right). \tag{6.1}$$

Diagonalizing $\hat{H}_0$ yields eigenenergies $E_0 \pm \hbar\Delta/2$ with corresponding eigenstates $|\psi_\pm\rangle = \frac{1}{\sqrt{2}}\left(|\mathrm{R}\rangle \pm |\mathrm{L}\rangle\right)$, respectively.

Applying a static bias V_b to DBP^- enables one to control the tunneling rate in the system by creating an energy offset $eV_\mathrm{b} = E_{0,\mathrm{L}} - E_{0,\mathrm{R}}$ between the left and right DB while preserving the local confinement potential characteristics at each well as depicted in Fig. 6.1. This bias is physically implemented by local electrodes in the vicinity of the DBP^-. More background information on the applied bias can be found in Sec. 3.1.3.

The Hamiltonian of a DBP^- subjected to a static bias is given by [160]

$$\hat{H}_\mathrm{b} = E_0'\mathbb{1} + \frac{eV_\mathrm{b}}{2}\left(|L\rangle\langle L| - |R\rangle\langle R|\right) + \frac{\hbar\Delta}{2}\left(|L\rangle\langle R| + |R\rangle\langle L|\right) \tag{6.2}$$

with

$$E_0' := \frac{E_{0,\mathrm{L}} + E_{0,\mathrm{R}}}{2},\ eV_\mathrm{b} := E_{0,\mathrm{L}} - E_{0,\mathrm{R}}, \tag{6.3}$$

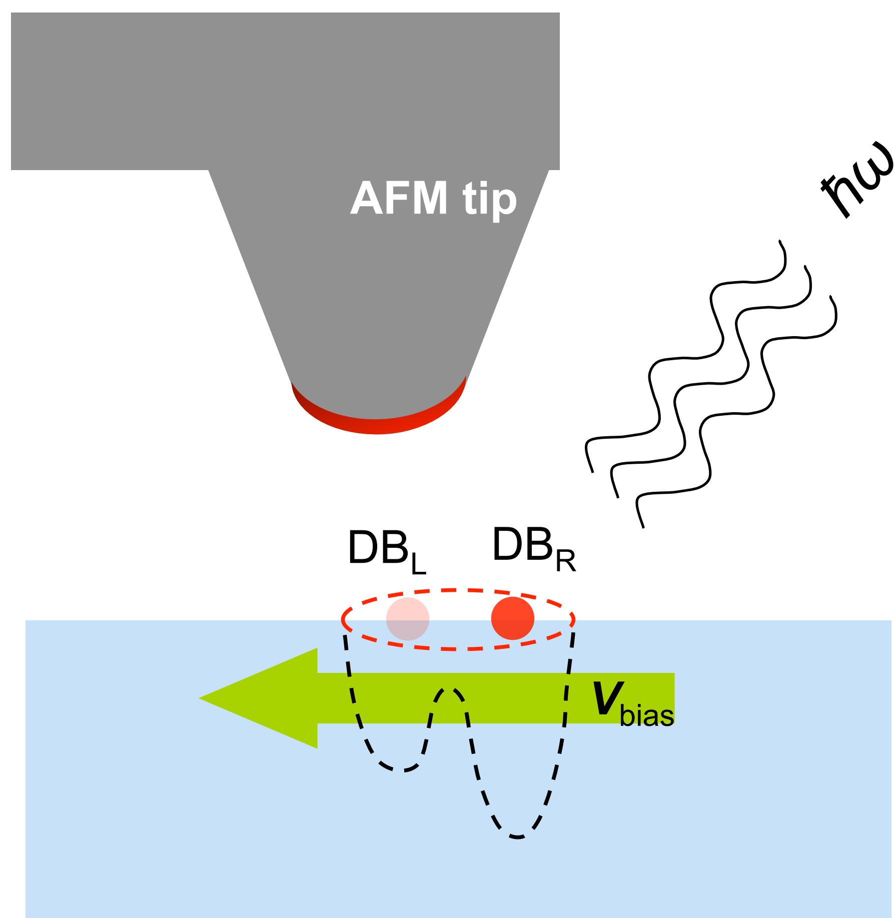

Figure 6.1: The dangling-bond pair (DB_L-DB_R) is depicted as a double-well potential at the silicon-vacuum interface. An excess electron shown as a red (dark) dot oscillates between the two wells. The DB pair is subjected to a static electric bias and driven by laser radiation. An atomic-force microscope (AFM) tip is capacitively coupled to the DB pair due to electrostatic interaction between charges on the AFM tip (red (dark) zone on tip apex) and the excess electron in the double-well potential. The AFM tip oscillates with a frequency that is dependent on the location of this excess charge thereby modifying the tip oscillation frequency in a predictable way. [reproduced from ref. [3], Fig. 1]

and where $\mathbb{1}$ is the identity matrix. Diagonalizing the biased Hamiltonian for the DBP$^-$ (6.2) yields

$$\hat{H}_\mathrm{b} = E_0'\mathbb{1} + \frac{\hbar\Delta'}{2}\left(|\mathrm{g}\rangle\langle\mathrm{g}| - |\mathrm{e}\rangle\langle\mathrm{e}|\right) \tag{6.4}$$

and

$$|\mathrm{g}\rangle = \cos\frac{\theta}{2}|\mathrm{L}\rangle + \sin\frac{\theta}{2}|\mathrm{R}\rangle,\ |\mathrm{e}\rangle = \cos\frac{\theta}{2}|\mathrm{R}\rangle - \sin\frac{\theta}{2}|\mathrm{L}\rangle$$

where

$$\theta = \tan^{-1}\left(\frac{\hbar\Delta}{eV_\mathrm{b}}\right).$$

The resultant modified tunnelling frequency is thus

$$\Delta' = \sqrt{\Delta^2 + \left(\frac{eV_\mathrm{b}}{\hbar}\right)^2}, \tag{6.5}$$

and the time-averaged charge distribution on the left dot is

$$\rho_\mathrm{L} = |\langle\mathrm{L}|\mathrm{g}\rangle|^2 = \cos^2\frac{\theta}{2} = \frac{\Delta^2}{\Delta^2 + \left(\Delta' + \frac{eV_\mathrm{b}}{\hbar}\right)^2}, \tag{6.6}$$

which is depicted as the solid curve (in purple) in Fig. 6.2. As expected, the charge distribution is equal for the two DBs when the electric potential bias is zero.

6.1.2 Mid-infrared driving field

We now add a MIR driving field with frequency ω_MIR to the scheme as shown in Fig. 6.1. The purpose of this driving field is to probe the system to discover resonance conditions whereby the barrier between the left and right DBs effectively vanishes [47]. A tunable continuous-wave solid-state laser or CO_2 gas laser are examples of suitable MIR sources [118]. More background material on MIR field is given in Sec. 3.1.4. The MIR beam intensity must be weak enough to ensure that multi-photon resonances are negligible [47, 48], but strong enough to drive the oscillation between left and right DBs.

A quantitative description of the dynamics begins by treating the biased DBP$^-$ as an electric dipole with an approximate transition dipole moment $\boldsymbol{d}_{\mathrm{DBP}^-} = -e\boldsymbol{x}$, which is the

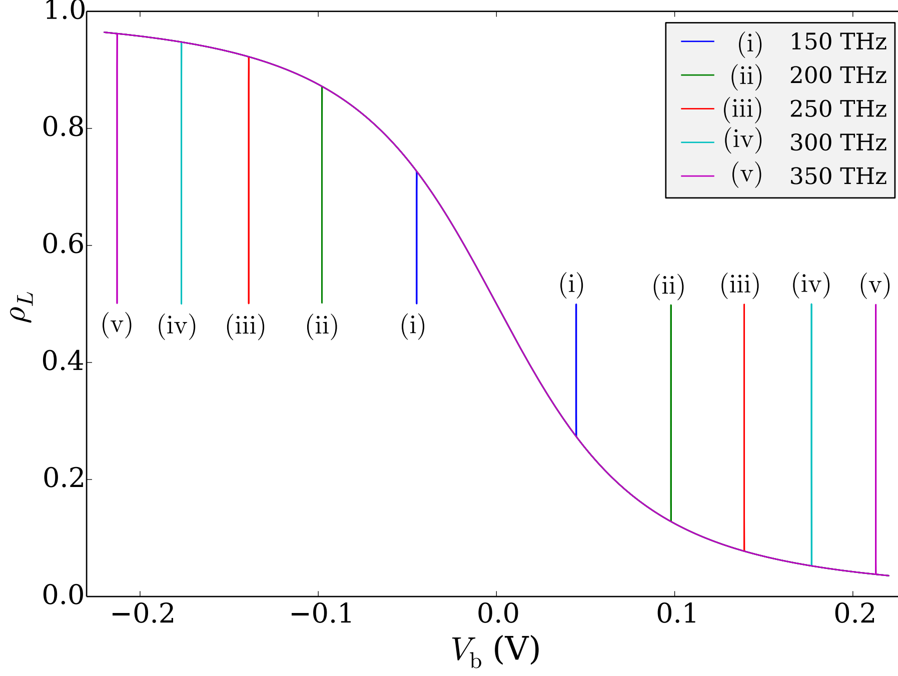

Figure 6.2: Time-averaged charge probability in the left DB as a function of applied static bias and under MIR lasers of different frequencies shown in the legend. Here, we have chosen $\Delta = 133$ THz and $\Omega_{\mathrm{MIR}} = 1$ GHz. In the absence of a driving radiation, the result becomes the smooth curve joining all the shown peaks. [reproduced from ref. [3], Fig. 3]

product of the electron charge e and the inter-DB separation vector $\boldsymbol{x}$ pointing from the negative to the neutral DB. The corresponding dipole-moment operator is $\hat{\boldsymbol{d}} = \boldsymbol{d}_{\mathrm{DBP}^-}\hat{\sigma}_x$.

The electric-dipole interaction with the MIR electric field $\boldsymbol{E}_{\mathrm{MIR}}$ is given by the interaction Hamiltonian [161]

$$\hat{H}_{\mathrm{dipole}} = -\hat{\boldsymbol{d}} \cdot \boldsymbol{E}_{\mathrm{MIR}}. \tag{6.7}$$

The interaction strength is quantified by the Rabi frequency

$$\Omega_{\mathrm{MIR}} = \frac{\hat{\boldsymbol{d}} \cdot \boldsymbol{E}_{\mathrm{MIR}}}{\hbar}, \tag{6.8}$$

and the resultant driving-field interaction Hamiltonian is [81]

$$\hat{H}_{\mathrm{d}} = \hbar\,|\Omega_{\mathrm{MIR}}| \cos\omega_{\mathrm{MIR}} t \big[\cos\delta\,(|\mathrm{R}\rangle\langle\mathrm{R}| - |\mathrm{L}\rangle\langle\mathrm{L}|) + \sin\delta\,(|\mathrm{L}\rangle\langle\mathrm{R}| + |\mathrm{R}\rangle\langle\mathrm{L}|) \big] \tag{6.9}$$

for δ a parameter containing information about the laser beam angle and ratio of wavelength to dipole length.

The intensity of the radiation is related to the Rabi frequency via the electric-field amplitude, $I = \epsilon_0 |\boldsymbol{E}|^2 c$ with ϵ_0 the permittivity, $\boldsymbol{E}$ the electric-field amplitude, and c the speed of light. Assuming that $\boldsymbol{E}_{\mathrm{MIR}}$ and $\boldsymbol{d}_{\mathrm{DBP}^-}$ are parallel, Eq. (6.8) yields

$$|\boldsymbol{E}| = \hbar\Omega_{\mathrm{MIR}}/|\boldsymbol{d}_{\mathrm{DBP}^-}|. \tag{6.10}$$

For a DBP$^-$ with inter-DB distance $|\boldsymbol{x}| = 7.68$ Å, we obtain $\boldsymbol{d}_{\mathrm{DBP}^-} \approx 10^{-28}$ Cm.

In addition to the conditions above, the Rabi frequency is low enough to avoid multi-photon resonances, but high enough to drive the oscillation, and the choice of $\Omega_{\mathrm{MIR}}/\omega_{\mathrm{MIR}}$ offers some flexibility to tune these parameters. We therefore studied the effects of the intensity of the applied laser in Fig. 6.3, where we varied this quantity over a few orders of magnitude.

We can see in this figure that, as the intensity is decreased, the width of the resonance peaks is decreased as well. Eventually the width becomes lower than the noise in the applied bias, for a laser intensity of about 20 W/m^2. The horizontal resolution was estimated by treating the width as being due to the thermal noise in the biasing electrodes, namely the Johnson-Nyquist noise given by the formula

$$V_{JN} = \sqrt{4kTRB} \tag{6.11}$$

for $R = 1$ MΩ, and $B = 3$ kHz, similar to values present in an STM instrumental setup. The corresponding Rabi frequencies for each peak width are plotted in Fig 6.3(b) (anticipating that this is also the range of useful Rabi frequencies for the purpose of this study, i.e. 0.1 GHz to 1 THz.)

6.1.3 The combined action of static bias and driving field

The Hamiltonian including both the static bias and the driving field is

$$\hat{H}_{\mathrm{bd}} = \hat{H}_{\mathrm{b}} + \hat{H}_{\mathrm{d}}. \tag{6.12}$$

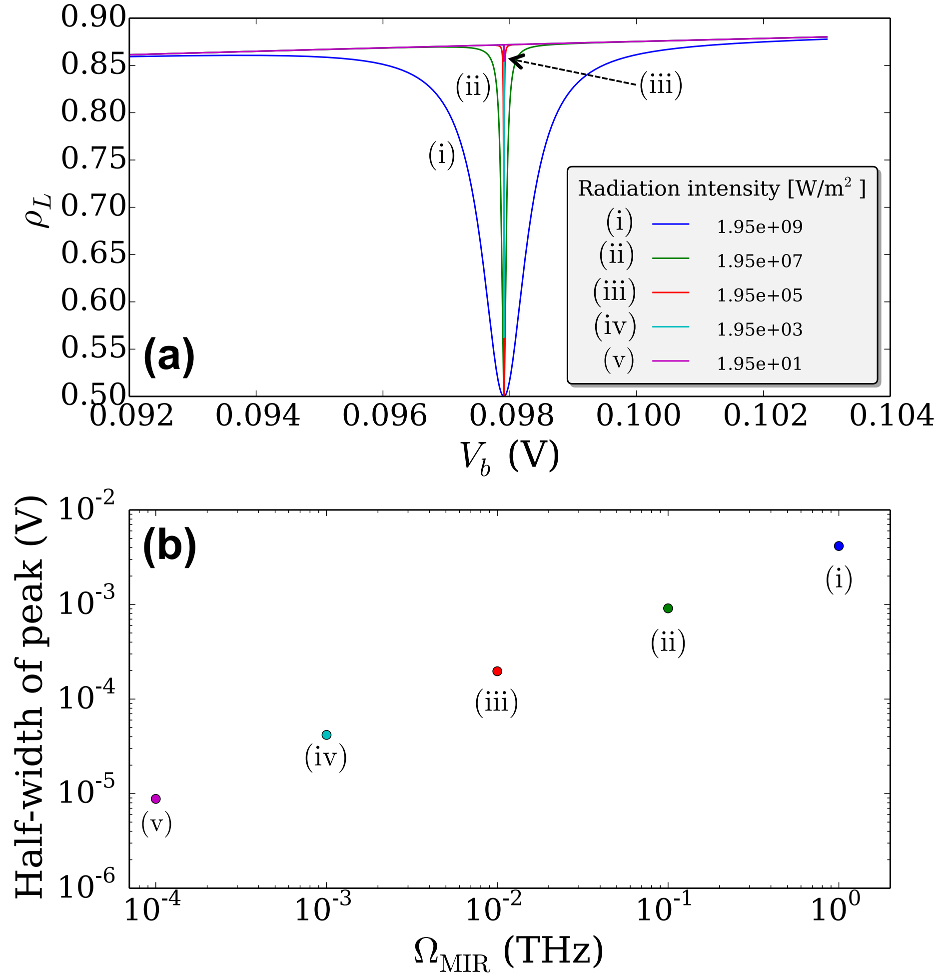

Figure 6.3: The effects of varying the driving field intensity on the resonance peak shapes. (a) Here ω_{MIR} is kept fixed at 200 THz, and as the field intensity is reduced the resonance peaks become narrower. (b) The peak widths are extracted from the above plots and are plotted against the corresponding Rabi frequencies. The color of each point here corresponds to a plot in (a). The bottom-left point corresponds to the lowest measurable field intensity as limited to the thermal noise in the biasing electrodes. [reproduced from ref. [3], Fig. 4]

Converting to the interaction picture according to

$$\hat{H}_{\mathrm{I}} = U^{\dagger}\hat{H}_{\mathrm{bd}}U,\ U := \exp\left[-\mathrm{i}\frac{\omega_{\mathrm{MIR}}t}{2}\left(|\mathrm{R}\rangle\langle\mathrm{R}| - |\mathrm{L}\rangle\langle\mathrm{L}|\right)\right]$$

eliminates explicit time dependence. If the detuning $\eta := \omega_{\mathrm{MIR}} - \Delta'$ is small compared to the frequency sum $\omega_{\mathrm{MIR}} + \Delta'$, then [81]

$$\frac{\hat{H}_{\mathrm{I}}}{\hbar} \approx \frac{\Omega}{2}\left(|\mathrm{g}\rangle\langle\mathrm{e}| + |\mathrm{e}\rangle\langle\mathrm{g}|\right) + \frac{\eta}{2}\left(|\mathrm{g}\rangle\langle\mathrm{g}| - |\mathrm{e}\rangle\langle\mathrm{e}|\right), \tag{6.13}$$

where

$$\Omega := |\Omega_{\mathrm{MIR}}| \sin(\theta - \delta) \tag{6.14}$$

for a weak MIR field, namely $\Omega_{\mathrm{MIR}} \ll \omega_{\mathrm{MIR}}$ [161].

The eigenenergies of the approximate interaction Hamiltonian $\hat{H}_{\mathrm{I}}$ in (6.13) are [81]

$$\varpi_{\pm} := \pm\frac{\hbar}{2}\sqrt{\Omega^2 + \eta^2}, \tag{6.15}$$

which represent the modified Rabi frequencies. The corresponding eigenstates are

$$|\mathrm{g}\rangle_{\varphi} = \cos\frac{\varphi}{2}|\mathrm{g}\rangle - \sin\frac{\varphi}{2}|\mathrm{e}\rangle,\ |\mathrm{e}\rangle_{\varphi} = \cos\frac{\varphi}{2}|\mathrm{e}\rangle + \sin\frac{\varphi}{2}|\mathrm{g}\rangle \tag{6.16}$$

where $\varphi = \tan^{-1}\left(\frac{|\Omega|}{\eta}\right)$. The probability for the charge to be on the left DB is

$$\rho_{\mathrm{L}} = |\langle\mathrm{L}|\mathrm{g}\rangle_{\varphi}|^2 = \frac{1}{2} + \frac{eV_{\mathrm{b}}}{2\hbar\Delta'}\frac{1}{1 + \frac{1}{2}\tan^2\varphi} \tag{6.17}$$

analogous to the undriven distribution (6.6).

In an actual experiment, for a given MIR frequency ω_{MIR}, the potential bias V_{b} is adjusted until a resonance is found whereby the charge distribution is equal on the two DBs. Thus, one is expected to obtain curves similar to those in Fig. 6.2, where the spikes correspond to cases that $\omega_{\mathrm{MIR}} = \Delta'$. Intuitively, these resonances correspond to the MIR driving field overwhelming the biasing field, effectively making the barrier negligible and the charge distribution equal in either DB.

Fig. 6.4 shows an extended parameter space as contour plots of loci where, for fixed values of Δ indicated in the legend, resonances such as those in Fig. 6.2 occur. This figure

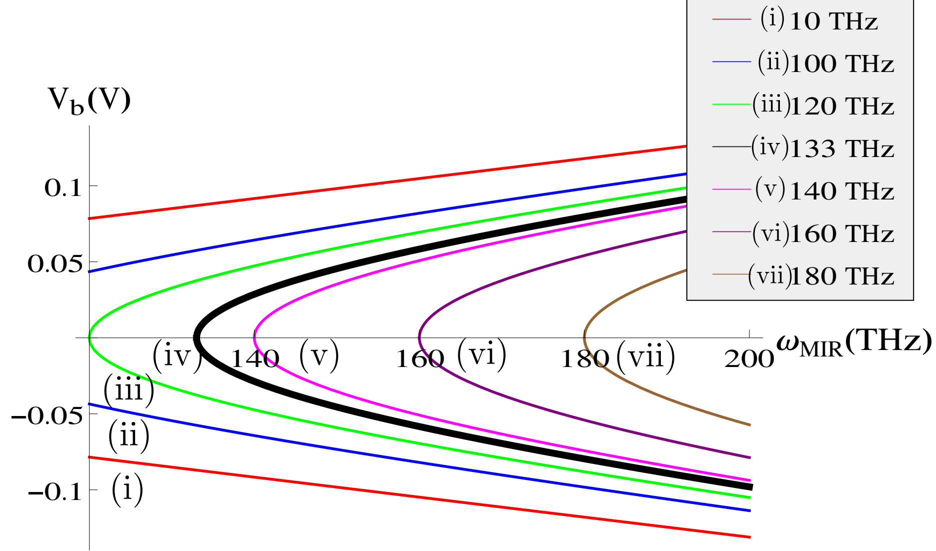

Figure 6.4: Contour plots of loci in the parameter space (V_{b}, ω_{MIR}) where resonances occur, i.e. spikes in Fig. 6.2 where $\rho_{\mathrm{L}} = \frac{1}{2}$. Each contour corresponds to a different native DBP^{-} tunneling frequency Δ, indicated in the legend. [reproduced from ref. [3], Fig. 5]

illustrates a key point of our scheme, namely that the MIR frequency and potential bias can be tuned to discover the tunneling frequency Δ simply by measuring the probability of the excess charge being in the left DB.

6.1.4 Effect of laser heating on the system

Excessive heating by the incident laser radiation can lead to damage of the sample. An important detail when estimating laser damage in our sample is that we only require radiation with sub-bandgap energy, for which the silicon absorption coefficient is relatively small. Therefore, silicon crystals are resilient to heating and have a high thermal and optical damage threshold[162] in the MIR range of interest due to low absorption for this spectral domain.

For the H–Si(100) substrate in our study, above-bandgap driving radiation (λ= 532 nm) with an intensity of 2.67×10^{11} W/m^2 suffices to cause hydrogen desorption but does not damage the sample [163]. Given that we require sub-bandgap radiation (λ= 9-19 μm) with two orders of magnitude lower intensity, any damage to the sample is expected to be highly unlikely. At these greatly reduced intensity levels, hydrogen desorption is also unlikely [163].

Therefore we expect excessive heating can be avoided by using a cooling system even in cases with the most intense radiation required for our experimental apparatus.

6.2 AFM characterization of tunneling between coupled dangling bonds

Atomic force microscope is ideally suited to measure the spatial charge distribution in a DBP^- (Fig. 6.1) without significantly distorting the electronic landscape of the sample. The AFM has been shown to detect single charges [164, 165]. We are interested in frequency mode (FM) of the AFM. Details on the modeling of FM-AFM can be found in Subsec. 3.1.1.

6.2.1 Tip-sample interactions

In the limit of small oscillation amplitudes, the AFM tip motion is given by

$$\Delta\omega := \omega - \omega_0 \simeq -\frac{\omega_0}{2k} \frac{\partial F_\text{z}}{\partial z}\bigg|_{z_0} \tag{6.18}$$

which is showing the proportionality between the frequency shift and the local force gradient. In using the AFM to measure the charge distribution at the silicon surface, all significant tip-sample forces must be considered by our model. These can be short-range chemical forces (less than 5 Å), long-range van der Waals forces, electrostatic forces, or magnetic forces (up to 100 nm) [50]. However, we choose operational parameters to ensure that electrostatic forces produced by the DBP^- dominate over these other forces.

The external source potential V_t is kept constant during the interaction with the sample. If the tip is sufficiently far from the surface, chemical forces can be ignored, and magnetic forces are negligible if the tip is made of non-magnetic material, e.g. tungsten. An ultrasharp nanotip [166] is employed to minimize forces arising from induced polarization of the sample. Reducing the tip oscillation amplitude to the Ångstrom scale, for example with a quartz-made qPlus sensor [106, 50, 107] also helps to minimize this form of interaction.

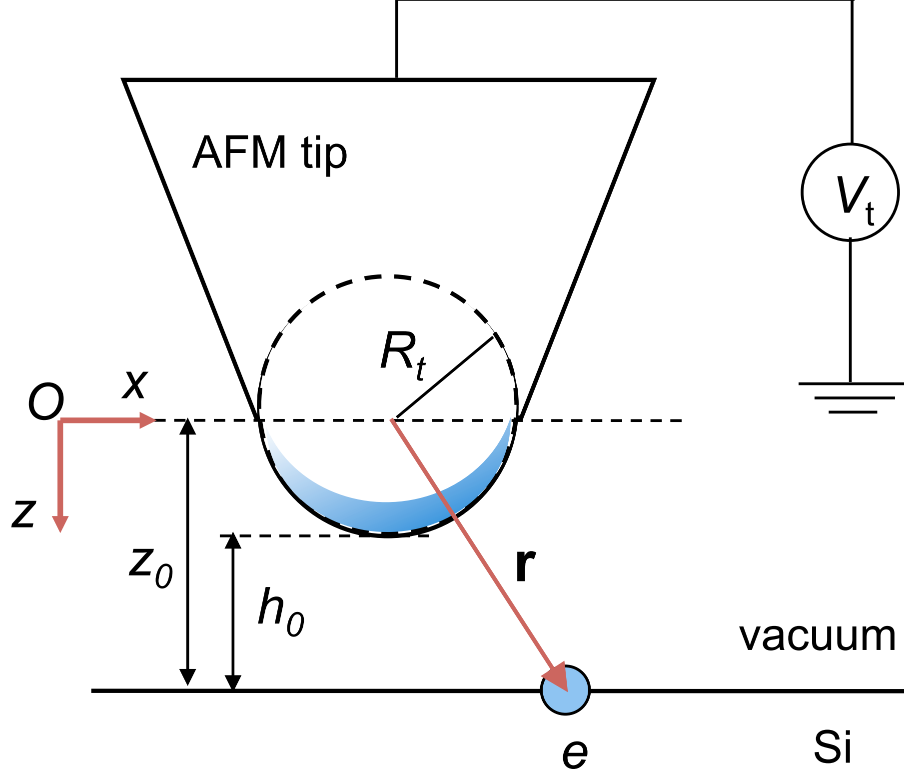

Figure 6.5: Schematic of AFM setup for charge sensing, illustrating the geometrical parameters relevant for the tip-sample interactions. The choice of the coordinate system (xOz), the position vector of the DB charge ($\boldsymbol{r}$), and the "boss sphere" (dashed circle) fitted to the apex of the AFM tip are shown. [reproduced from ref. [3], Fig. 7]

6.2.2 Trapped charge in the tip-sample system

A. Electrostatic potential energy

The DBP$^-$ can be treated as a trapped charge oscillating between the left and right DBs. This single charge is located within the plane of the Si surface (Fig. 6.5). Thus, the charge interacts with other entities such as the space-charge layer in the semiconductor substrate and other charges in the substrate and on the biased AFM tip, if present (see Sec. 3.1.3 for some background information on space-charge layer). Here we analyze the problem from a basic viewpoint in order to capture the essential electrostatic elements at play.

For an n-type Si sample with a donor concentration N_D, the presence of a locally planar electrode at a height h_0 above the surface biased at a voltage V_t induces a subsurface space-

charge layer in the semiconductor with a width w approximated by the solution of the quadratic equation [115]

$$\frac{eN_D}{2\varepsilon_r h_0}w^2 + eN_D w + \frac{\varepsilon_0 V_\mathrm{t}}{h_0} = 0, \tag{6.19}$$

where ε_0 and ε_r are the vacuum permittivity and semiconductor dielectric constant, respectively.

Correspondingly, the so-called band bending potential at a depth z_d into the sample can be written in the quadratic approximation as [115]

$$V_\mathrm{Si}\left(z_\mathrm{d}\right) = V_0\left(1 - \frac{z_\mathrm{d}}{w}\right)^2 \tag{6.20}$$

where V_0 is the potential at the surface given by

$$V_0 \approx \frac{eN_D w^2}{2\varepsilon_0\varepsilon_r}\mathrm{sign}\left(V_\mathrm{t}\right) \tag{6.21}$$

where 'sign' gives the sign of the applied tip bias. As the AFM tip is usually not locally planar the above equation is a coarse approximation for band bending representing an upper limit for the real case.

In order to calculate the potential at the Si surface, we approximate the electrostatic potential due to the biased AFM tip as being that of a biased conducting sphere with radius R_t fitted to the apex region of the tip (or the "boss" as depicted in Fig. 6.5). In order to reflect the contribution of the mobile charge carriers in the substrate, we apply a rescaling of this spherical potential, namely we recalibrate the value of the potential at the Si surface location directly under the tip apex, $\boldsymbol{r}_0 = (0, z_0)$, to be just V_0 given above.

From this analysis, at the location $\boldsymbol{r} = (x, z)$ of the DB, the *bare* potential due to the tip is

$$\phi\left(r\right) = \frac{V_0 r_0}{r} \tag{6.22}$$

where the coordinate origin is chosen at the center of the boss sphere. This bare potential does not include the image charge effects, which are accounted for below. Furthermore, for

the case when the amplitudes of the AFM cantilever are small, we can neglect the variation of V_0 with the tip height and use henceforth only its value at the equilibrium scanning height.

With the above assumptions, the effective electrostatic energy of the tip-charge system can be written as [167]

$$W^{\mathrm{eff}}(r) = -\frac{1}{2}C_{\mathrm{t}}V_{\mathrm{t}}^2 + \frac{eV_0 z_0}{r} - \frac{1}{8\pi\varepsilon_0}\frac{e^2 R_{\mathrm{t}}}{r^2 - R_{\mathrm{t}}^2} \tag{6.23}$$

where the last term accounts for the image charge inside the tip and for the charge redistribution via the voltage source as explained by Kantorovich et al. [167]Then the force exerted on the tip in the direction normal to the surface can be calculated as

$$F_z(r) = -\frac{\partial W^{\mathrm{eff}}}{\partial z} = \frac{eV_0 z_0 z}{r^3} - \frac{1}{4\pi\varepsilon_0}\frac{e^2 R_{\mathrm{t}} z}{\left(r^2 - R_{\mathrm{t}}^2\right)^2}. \tag{6.24}$$

This expression for force can then be substituted into Eq. (24) to approximate the expected AFM frequency shift.

B. Atomic-force-microscope frequency shift

The AFM frequency shift is obtained from the derivative of the force with respect to z, as in Eq. (6.18)

$$\Delta\omega = \frac{1}{2m\omega_0}\left[-\frac{eV_0 z_0\left(x^2 - 2z_0^2\right)}{r^5} + \frac{1}{4\pi\varepsilon_0}\frac{e^2 R_{\mathrm{t}}\left(R_{\mathrm{t}}^2 - x^2 + 3z_0^2\right)}{\left(R_{\mathrm{t}}^2 - r^2\right)^3}\right]. \tag{6.25}$$

In readout of a DBP$^-$ excess charge, the total AFM frequency shift is given by

$$\begin{aligned}
\Delta\omega_{\mathrm{AFM}} &= \rho_{\mathrm{L}}\Delta\omega^{(\mathrm{L})} + \rho_{\mathrm{R}}\Delta\omega^{(\mathrm{R})} \\
&= \rho_{\mathrm{L}}\left(\omega^{(\mathrm{L})} - \omega_0\right) + \left(1 - \rho_{\mathrm{L}}\right)\left(\omega^{(\mathrm{R})} - \omega_0\right) \\
&= \xi\rho_{\mathrm{L}} + \left(\omega^{(\mathrm{R})} - \omega_0\right),
\end{aligned} \tag{6.26}$$

where $\Delta\omega^{(\mathrm{L})}$ ($\Delta\omega^{(\mathrm{R})}$) is the frequency shift due to the charge localized in the left (right) DB and each frequency shift is weighted by the corresponding time-averaged charge probability ρ_{L} (ρ_{R}). The parameter ξ is the differential frequency shift of the cantilever caused by the excess charge tunneling from the right to the left DB; i.e.

$$\xi = \omega^{(\mathrm{L})} - \omega^{(\mathrm{R})}. \tag{6.27}$$

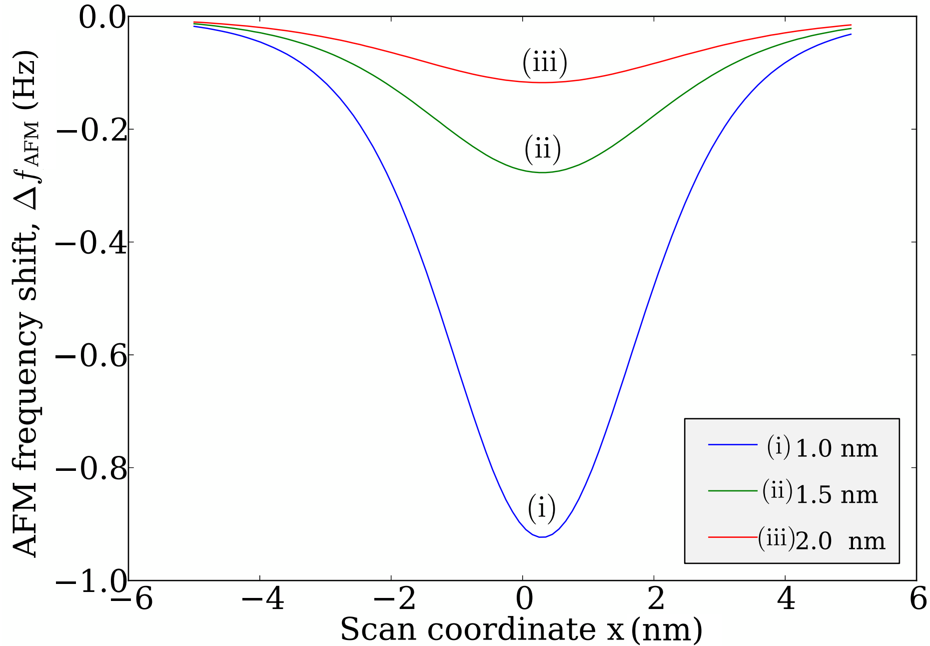

Figure 6.6: AFM frequency shift as the tip scans along a line coinciding with the DBP axis. The three curves correspond to as many equilibrium heights of the AFM tip indicated in the legend, while the other scan characteristics have the values indicated in the text. [reproduced from ref. [3], Fig. 8]

Equation (6.26) indicates that the AFM readout $\Delta\omega_{\mathrm{AFM}}$ is linear in ρ_{L}. Thus, we expect to observe resonances in the AFM output signal while scanning through a range of bias values V_{b}, owing to the existence of resonance features for ρ_{L} as seen in Fig. 6.2.

Note that the task of sensing the location of a single charge as in previous experimental work [107] is different from the current task, where we attempt to obtain information about both the location and the rates of (driven) motion of the electron. However, this does not violate the uncertainty principle as we are not measuring the *instantaneous* location and momentum of the particle, but rather time-averaged quantities, and the ultimate knowledge we aim to obtain of the quantum system is statistical in nature.

In order to optimize the AFM read-out, we judiciously choose experimental parameters. First, the AFM cantilever parameters should be chosen so that the noise is much lower than the signal. Second, for a given cantilever, we choose an appropriate oscillation amplitude

for the AFM tip. Larger amplitudes yield lower noise, whereas lower amplitudes offer better spatial resolution. Finally, ξ should be maximized with respect to x to achieve the largest possible frequency-shift read-out.

Although the greater sensitivity of silicon cantilevers is certainly a desirable feature for the purpose of the current study, at present it seems unlikely that they would allow the required atomic resolution mainly due to their inability to achieve low-amplitude oscillations and thus perform scans very close to the sample, 1-2 nm. Attempting such tasks would likely lead to undesired frequent jump-to-contact events and thus very poor scans.

On the other hand, the qPlus tuning-fork system, although less sensitive, has been already proven to sense single charge with atomic spatial resolution [107] due to its robustness and ability to scan very close to the sample at low amplitudes. (It easily avoids certain problems such as the jump-to-contact issue [168].) It also allows combined AFM/STM studies thus facilitating DB fabrication and precise positioning during the experiment. Therefore in this study we choose parameters representative of the qPlus system, keeping in mind that the optimal system may have characteristics somewhere in between those of the tuning fork and silicon cantilevers.

As experimental values, we henceforth assume $f_0 = 30$ kHz, $k = 1800$ N/m, $Q = 5 \times 10^4$, $R_\mathrm{t} = 5$ nm, $V_\mathrm{t} = 0$ V, and operation at liquid helium temperature. Also, unless otherwise specified, the oscillation amplitude and equilibrium height for the AFM tip are assumed to be 3 Å and 1 nm, respectively. The total noise in the frequency shift signal estimated for all the results below is less than 5 mHz at 4 K and 9 mHz at 77 K. As the AFM experiments yield the frequency shift in units of Hz, we present our results below in terms of $\Delta f_\mathrm{AFM} = \Delta\omega_\mathrm{AFM}/2\pi$.

For a DBP^- with separation of 7.68 Å, the AFM maximum differential-frequency shift is obtained when the left dangling-bond is $x \approx 3$ Å away from the AFM tip central axis. Figure 6.6 depicts the AFM frequency shift Δf_AFM as a function of the lateral tip position x. In this figure, it is clear that the effect of a trapped charge on the value of the AFM

frequency is highly dependent on tip height. The great increase in signal for a tip height less than 1 nm is due to the fact that image-charge forces dominate in such close proximity to the localized charge.

Note that despite the simplicity of our model, the calculated magnitude of the signal is commensurate with past experimental results of single-charge sensing with atomic resolution [107]. Hence, this scheme is appropriately sensitive to small displacements of single trapped charge.

Figure 6.7 shows the resonant peaks in the AFM signal. These resonant features are reflected in the oscillation frequency of the AFM tip when the DBP^- is simultaneously exposed to a static bias and a driving radiation. In fact, the resonances can be exploited by varying the static bias for a fixed driving frequency. For each value of driving frequency a pair of resonant peaks appear on the AFM signal for two symmetric static-bias values. These peaks contain information about our system and can be used to determine the tunneling frequency Δ of the excess charge.

More generally, Fig. 6.8 shows the AFM frequency shift as we sweep both the MIR driving frequencies and the applied static bias V_b from a negative to a positive value. The resonance loci appear here as ridges (trenches) when the MIR driving frequency is commensurate with the ramped tunneling frequency. These resonance trends mirror the parabolic relationship between the MIR driving frequency and the static bias, as shown in Fig. 6.4.

6.3 Damped dangling bond pair dynamics

Until now our analysis ignores noise causing decoherence in the two-level system. In this section we study the effect of noise on the shape and width of the resonances used to characterize electron tunneling. We show that the noise model can be tested by the measurements, and we consider the specific model of spin-boson coupling [39] to illustrate how the model is tested and the parameters are acquired by measurement.

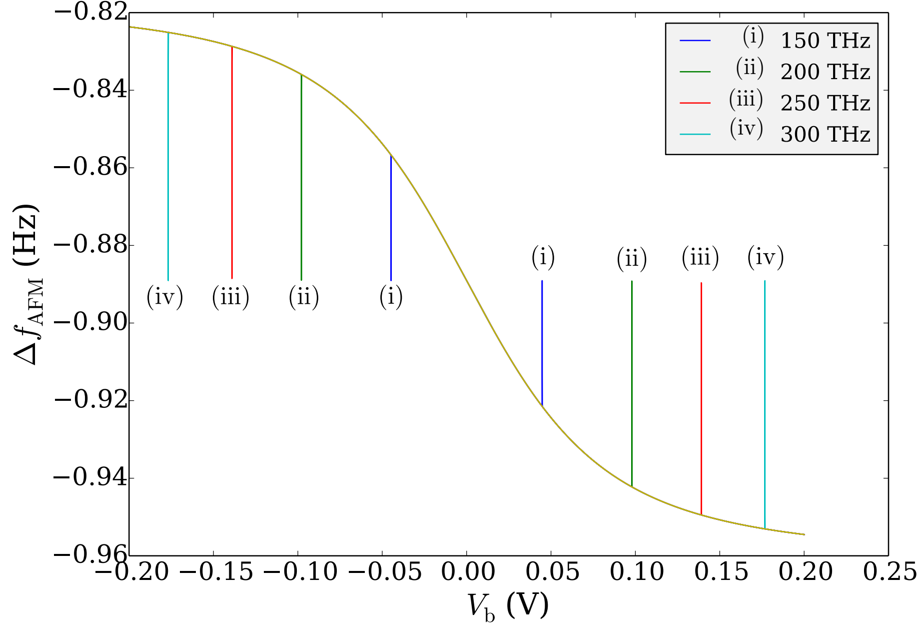

Figure 6.7: AFM frequency shift (Δf_{AFM}) as a function of static bias ($\mathrm{V_b}$) for four different values of driving radiation frequency given in the legend and Ω_{MIR}= 1 GHz. At each frequency a set of two resonant peaks appear for two symmetric static bias values. [reproduced from ref. [3], Fig. 9]

The spin-boson model characterizes weak coupling between a two-level system and a generic bosonic bath, such as phonons or charge fluctuations [39]. It is described by the Hamiltonian

$$\hat{H}_{\mathrm{sb}} = \sum_i \hbar\omega_i \hat{b}_i^\dagger \hat{b}_i + \hat{\sigma}_z \sum k_i \left(\hat{b}_i^\dagger + \hat{b}_i\right) \tag{6.28}$$

with ω_i the ith oscillator frequency, $\hat{b}_i^\dagger$ and $\hat{b}_i$ the corresponding creation and annihilation operators, and k_i the coupling strength between the dangling-bond pair and the bath.

The first term on the right-hand side of Eq. (6.28) is the free bath Hamiltonian, and the second term is the system-bath interaction Hamiltonian. The interaction Hamiltonian indicates that the coupling depends linearly on the coordinates of the dangling-bond pair and the bath harmonic oscillators. The total Hamiltonian of the system would then be

$$\hat{H} = \hat{H}_{\mathrm{b}} + \hat{H}_{\mathrm{d}} + \hat{H}_{sb}, \tag{6.29}$$

where the first two terms are given in Eqs. (6.2) and (6.9). More elaboration on spin-

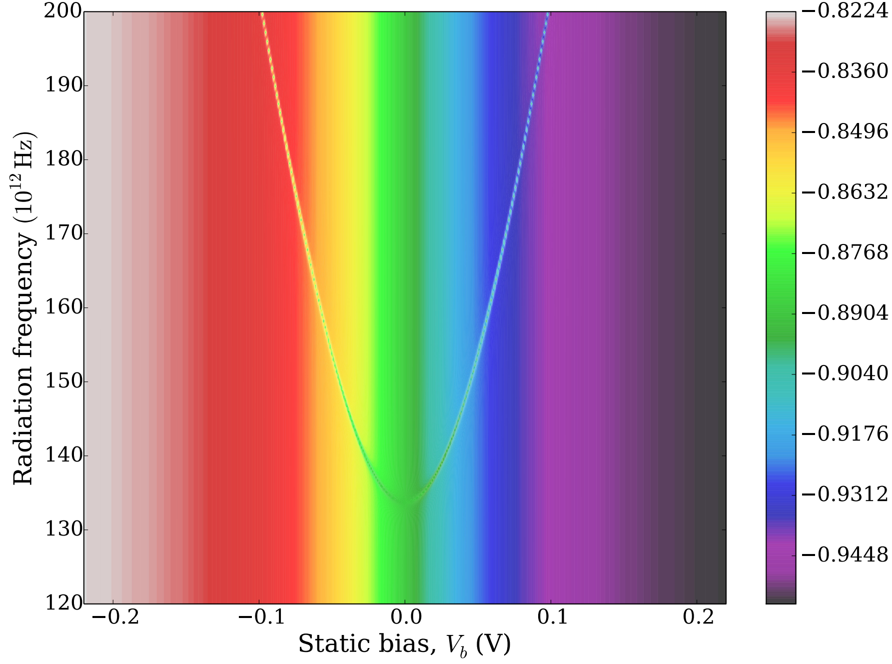

Figure 6.8: Location of the resonance peaks in Δf_{AFM} in the two-dimensional parameter space of the static bias and the driving radiation frequency. The DBP^- has a separation of 7.68 Å and the Rabi frequency is Ω_{MIR}= 500 GHz. [reproduced from ref. [3], Fig. 10]

boson model can be found in Sec. 2.6. Solving the master equation for the dangling-bond pair [169, 48], the steady-state probability for the excess charge to be in the left quantum dot is [81]

$$\rho_{\text{L-sb}} = \frac{1}{2} + \frac{eV_{\mathrm{b}}\Gamma_{\mathrm{r}}}{2\hbar\Delta'} \frac{\eta^2 + \Gamma_{\phi'}^2}{\eta^2\Gamma_{\mathrm{r}} + \Omega_{\mathrm{MIR}}^2\Gamma_{\phi'} + \Gamma_{\mathrm{r}}\Gamma_{\phi'}^2}, \tag{6.30}$$

with decoherence rate $\Gamma_{\phi'} = \Gamma_\phi + \Gamma_{\mathrm{r}}/2$ for relaxation rate Γ_{r} and dephasing rate Γ_ϕ. For $\Gamma_{\phi'} \to 0$ and $\tan\varphi = \frac{|\Omega|}{\eta}$, Eq. (6.30) reduces to Eq. (6.17). In another limit, the relaxation rate Γ_{r} and dephasing rate Γ_ϕ are equal up to second order in the limit of weak qubit-bath coupling: $\Gamma := \Gamma_r \approx \Gamma_\phi$.

The AFM frequency shift is shown in Fig. 6.9 as a function of static bias for MIR driving frequency ω_{MIR} fixed to 250 THz and various decoherence rates given in the legends. As the Rabi frequency is sampled in decreasing order over three orders of magnitude in (a), (b), and (c), we notice a very strong narrowing of the resonance peaks, which was also seen in

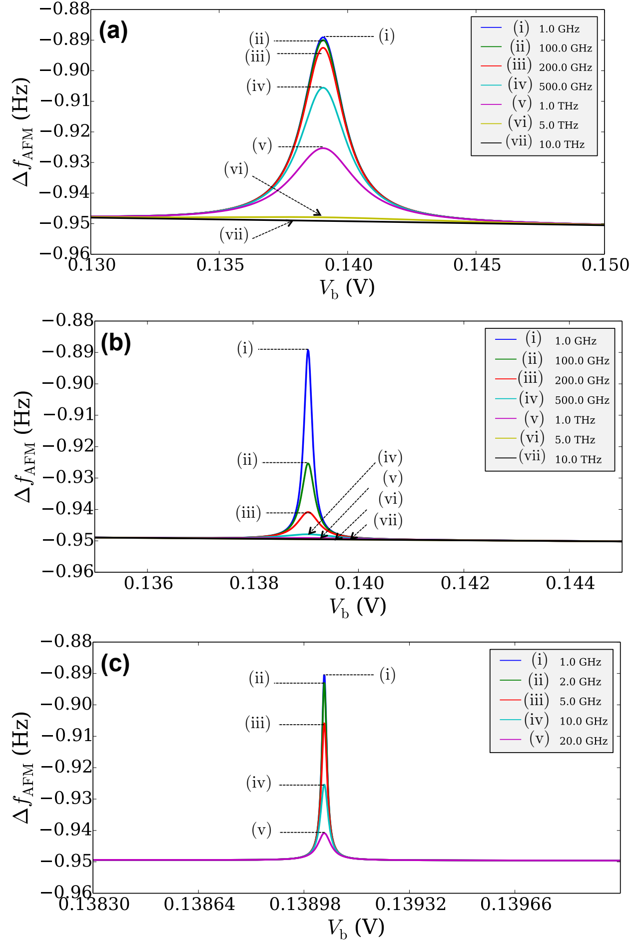

Figure 6.9: AFM frequency shift as a function of static bias for different decoherence rates shown in the legends and for three chosen values of the Rabi frequency: 1 THz in (a), 100 GHz in (b), and 10 GHz (c). The laser frequency was fixed to ω_{MIR}= 250 THz in all cases. Note the progressive narrowing of the range on the horizontal axis from top to the bottom panels. [reproduced from ref. [3], Fig. 11]

Fig. 6.3 in the absence of any decoherence.

A different range of decoherence rate was sampled in each case in order to capture the main effect: peak height decreases with increasing decoherence rate and the effect is measurable when the Rabi frequency is commensurate (same order of magnitude) with the decoherence rate. This is similar to the behavior of a critically damped driven harmonic oscillator.

For a Rabi frequency exactly equal to the decoherence rate, the peak height is about 40% of its predicted decoherence-free value. Note that the plots in (c) are predicted to be

applicable at low temperature (4K), while (a) and (b) could be used at higher temperatures if the decoherence rates go up. As our proposed experiment is to take place at temperatures of 4 K and higher, a Rabi frequency of 10 GHz seems sufficient to capture these decoherence signatures in the low temperature regime. This corresponds to an applied laser intensity of about 2×10^5 W/m^2. Note however that an even smaller laser intensity (2×10^3 W/m^2) is sufficient if one does not seek decoherence measurements, but only the native tunneling rates of the qubit.

Experimentally, the limiting factors in measuring these peaks are the (horizontal) resolution in the voltage on the biasing electrodes, and the (vertical) resolution in the frequency shift of the AFM. In practice, measured resonant peaks can be compared with model curves to yield information about the decoherence rates. For a sufficiently weak MIR field, the full-width-at-half-maximum height of each peak directly yields the decoherence rate. Even if the coupling strength between the MIR field and the DBP$^-$ is unknown, the decoherence rate can still be determined by extracting the resonant peak height as a function of width for various values of the power of the incident MIR field [81].

Fig. 6.9 conveys three key points of our proposal: how the tunneling rate Δ can be inferred, how the decoherence model can be tested, and how the decoherence rate Γ is obtained if the model is correct. The tunneling rate is revealed by observing resonances of the AFM frequency shift and is obtained by choosing ω_{MIR} and V_{b} judiciously. The decoherence model is tested by seeing whether the frequency shift obeys the model-predicted dependence on driving-field frequency and static bias. Finally, the decoherence rate is obtained by comparing the measured resonance peak heights with those predicted for a decoherence-free system. The plots in Fig. 6.10 serve as examples of expected behavior and can be used in practice for extracting decoherence parameters from experimental data.

In the spin-boson decoherence model discussed here, the decoherence rate can be determined solely from the width of the peak because Γ_{r} and Γ_{ϕ} are equal up to second order

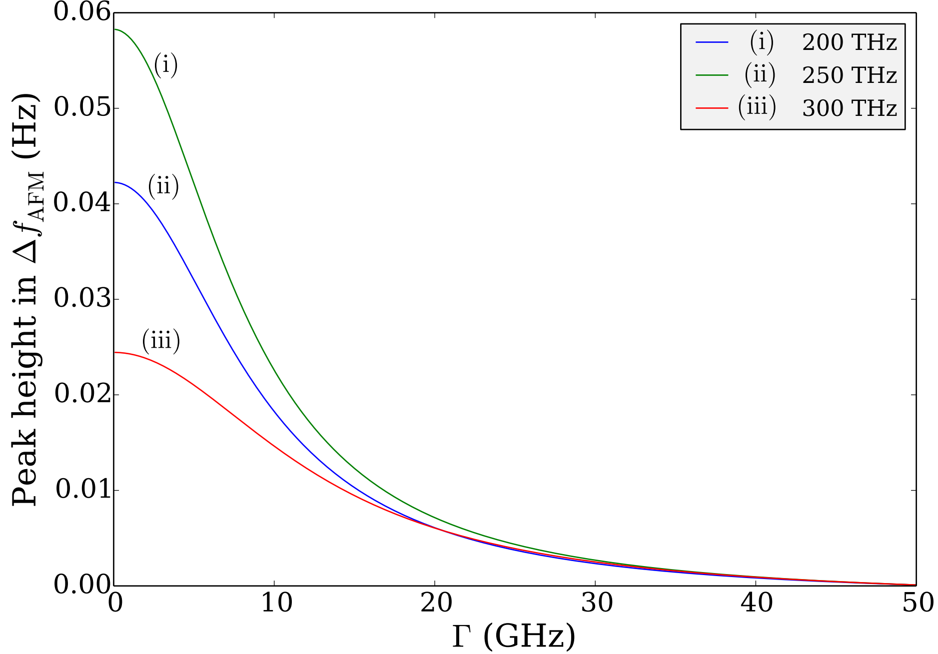

Figure 6.10: Resonant peak magnitudes in the AFM frequency shift as a function of decoherence rate Γ for different fixed frequency ω_{MIR} of the driving radiation shown in the legend and for a Rabi frequency set at 10 GHz. [reproduced from ref. [3], Fig. 12]

in the limit of weak qubit-bath coupling. For a noise model with independent relaxation and dephasing rates, Eq. (6.30) demonstrates sensitivity to changes in each of these rates independently.

A practical concern in performing the experiment is the back-action of our detector (AFM) on the quantum system being measured. The AFM cantilever has a frequency of 10^4 Hz, whereas the oscillation frequency of the dangling-bond excess-charge is estimated to be 10^{14} Hz. Thus, the AFM tip motion looks adiabatic to the excess charge and the back-action of the tip on coherent electron dynamics in the dangling-bond pair is negligible.

There is, however, a static component of the tip perturbation on the qubit, which is the flipside of the AFM sensitivity of charge location: the tip creates a static bias along the DBP^- axis. We calculated this bias for our optimized setup to have a maximum of 15.8 meV at the spatial location of maximum AFM sensitivity. Fortunately, this static bias does not significantly alter our scheme as it just adds to the applied static bias, and the resonance

peaks will still be obtained albeit with a horizontal shift of 15.8 meV. Therefore, correcting for this back-action is just a simple matter of recalibrating the horizontal (V_{b}) axis in our plots so the peak locations become again symmetric. Thus we have the ability to measure this shift and compensate for it in any subsequent data processing.

6.4 Summary

We have proposed a feasible experimental scheme for characterizing the fast tunneling rate as well as the nature and rate of decoherence of an excess charge shared between a pair of coupled dangling bonds on the surface of silicon. In our scheme, the electrostatic potential across the dangling-bond pair is ramped by external electrodes. Furthermore the dangling-bond pair is driven by a MIR field, and the resulting resonances correspond to equal distribution of the electron location in the dangling-bond pair despite, and independent of, the strength of the static bias thereby revealing the desired tunneling properties.

The distribution of the excess electron between left and right dangling bonds is detected by capacitively coupling the DB excess charge to an atomic force microscope tip. Resonances are observed on the AFM frequency-shift signal when the MIR field matches the ramped tunneling frequency of the excess charge.

Experimentally, charge qubit geometries must be chosen so that tunnel splittings (and corresponding driving frequencies) should avoid undesired excitations such as the different vibration modes of H-Si bonds [61, 62]. In practice, a control experiment would first be used to calibrate the AFM probe in the absence of driving radiation. In order to calibrate the vertical oscillation frequency as a function of lateral position, an AFM tip will be placed at different positions near a *single* DB^{-}. The AFM vertical oscillation frequency will exhibit a shift that depends on the lateral position of the tip with respect to the charge and the tip height. Oscillation amplitudes and tip height can then be adjusted to obtain maximum signal.

Our scheme will enable in-depth studies of quantum coherent transport of electrons between dangling bonds on the surface of silicon and enable the study of phonons and other interactions. As dangling bond systems are promising building blocks for quantum-level engineering of novel devices including quantum-dot cellular automata [1] and quantum computing [2] a detailed quantitative analysis of electron dynamics in dangling bond assemblies is an important step.

Chapter 7

Summary, Conclusion and Future Work

In this thesis, I presented theories and proposed a scheme for characterizing the coherent dynamics of a coupled dangling-bond pair (DBP^-) located on a Si surface. A dangling bond is known as a surface defect and a charge trapper in semiconductor systems. Our aim is to change this defect to a useful tool for quantum computing and quantum engineering purposes, at nanometer and even sub-nanometer scales.

My research project leverages on an experiment in 2009, demonstrating that Si-surface DBs that are located close enough to each other, display a different brightness in STM imaging of the surface, and also the level of DB-pair brightness depends on the separation distance between them [1]. The conjecture was the DBs were coupled to each other by sharing a single excess charge, but whether this coupling was coherent or not remained an open question. This open question became the main focus of my PhD studies.

Dangling bonds are localized entities, have unique shape, and can be created selectively on a Si surface by means of a nano tool such as scanning tunneling microscope tip. In addition, they are on the surface rather than in the crystal bulk, thus enabling more direct preparation, control, and readout. Considering these features plus their sub-nanometer size, dangling bonds are an excellent candidate for an atomic-scale quantum dot.

Learning about the coherent dynamics of a coupled dangling-bond pair opens up opportunities for using the DBP^- as the building block of more complex systems, such as quantum computating architectures [2], quantum cellular automata unit cells [1], and DBs sub-nanowires [33, 34]. Furthermore, it helps to have a better understanding of the coherence and bonding properties of the Si surface of interest. In the following, I first summarize the main points of our research work, and then propose future directions that can be undertaken

from each result.

7.1 Summary and Conclusion

7.1.1 DBP$^-$ as a charge qubit

As the first objective, we showed that coupled-DB pairs, located on the phosphorous-doped hydrogen-terminated Si(100)-2×1 surface, have excellent coherence properties. Thus, DBP$^-$s can be a potential candidate for a charge qubit. This feature raises from the miniaturization of charge qubit to atomic realm, which leads to extremely high tunneling rate while decoherence scales weakly with DBs separation.

We employed *ab initio* (time-dependent) density functional theory and also Wentzel-Kramers-Brillouin approximation theory to calculate tunneling rates of DBP$^-$s sharing the same configuration (i.e. vertical configuration) but with different DB-pair separation distances. Also, we used the spin-boson model to calculate the effect of voltage fluctuations in biasing electrodes and also the effect of surface and bulk phonons in the Si crystal, as the main sources of error, on the decoherence rate of these DBP$^-$s.

Furthermore, we developed the dynamics of a complex system that is composed of any number of DBs. For this purpose, we employed the extended Hubbard model and modified the model by adding an extra term corresponding to time-dependent potential biases. This term finds applications such as controlling the DBP$^-$s tunneling rate, and generating correlation (via Coulombic interaction) between different DBP$^-$s.

For a well-patterned architecture of the DBs (such that DBs are in pair with a well-chosen separation between the pairs), our model simplifies to a Hamiltonian consisting of DBP$^-$ dynamics with controllable tunneling rates and single- and two-DBP$^-$s operation gates. Also, while the complete fulfillment of the DiVincenzo's criteria is not explicitly addressed, but initialization, gating time and readout are briefly discussed for such a QC architecture.

7.1.2 Ab initio calculation of DBP^{-}s energy splitting

As the second objective, we investigated the effect of the anisotropic structure of the Si surface on energy splitting of coupled dangling-bond pairs. For this purpose, we calculated the ground state and the first excited state of the DBP^{-} by employing the *ab initio* DFT and time-dependent DFT techniques. The DBP^{-} energy splitting is then the energy difference between these two energy states. The tunneling rate of a DBP^{-} excess charge is linearly proportional to the energy splitting of the corresponding DBP^{-}.

For a multiparticle system, e.g. the system of our interest, finding the exact solution to the Schrödinger equation by the wavefunction theory is impossible due to limitations on computational resources. Density functional theory introduces a smart approach to this obstacle by using the system's electron density as the variable rather than using particles' spin and spatial coordinates. In the DFT approach, one is required to specify a theoretical method (which determines the degree of electrons correlation in the desired system) and a basis set in order to solve the Schrödinger equation of the system. Although some approximations are involved with this method, this method is called *ab initio* as it usually provides results that are in good agreement with experimental results.

In order to develop an understanding of the effect of the surface structure on the energy splitting of a DBP^{-}, we modeled a wide variety of DBP^{-} configurations with DBs located on pyramidal-shape Si clusters. These cluster models were then used as inputs for the DFT calculations. In each cluster model, the two DBs of a chosen DBP^{-}, were selected either from the same site or opposite sites of the Si dimers, where the dimers could be from the same row or adjacent rows of the Si-cluster surface. Also DB-pair separation could vary up to the limit determined by the Si cluster size.

We found that although the DBP^{-} energy splitting decreases *almost* exponentially as a function of DB-pair separation, the rate of decrease depends on the type of configurations. Based on the computed results, we could categorize DBP^{-} configurations to four different

types where each type reflects a particular effect of the surface structure. Learning about the structure and the orientation of the dangling-bond orbital played an important role in understanding and categorizing the DBP^- configurations.

In addition, we analyzed the effect of the cluster size and its surface edges on the DBP^- energy splitting. This effect has been checked by choosing a particular DBP^- on different cluster sizes and looking for the convergence properties in the calculated results. We identified the minimum size that a cluster model should have for the results on DBP^- energy splitting to be reliable.

Also, we analyzed the effect of the dopant's location within the clusters on the results of energy-splitting calculation. The position of the phosphorous atom within a cluster is important as the dopant P should not be very close to the DBs in order to avoid strong interaction with them. We found a proper location for the P atom beyond which the calculated results converged to a unique value. The results indicate that the P atom acts like an excess charge for our system when it is positioned beyond certain distance from the DBs.

The obtained results provide good insight on the effect of our desired Si-surface on the coherence of DBP^-. As a step forward, experimental characterization of the coherent dynamics of these DBP^- is of paramount importance. We found that the tunneling rate of the DBP^- excess-charge is extremely high, such that it cannot be detected by conventional electronic techniques. In the following section, we propose a scheme to indirectly characterize the coherence dynamics of our DB system.

7.1.3 Proposed scheme for characterizing DBP^- coherent dynamics

The extremely high tunneling-rates of the DBP^- excess charge results in some practical difficulties in monitoring the oscillation of the charge and thus directly characterizing its dynamics by any straightforward method. As the third objective, we proposed a feasible experimental scheme to indirectly characterize the fast tunneling rate of the DBP^- excess charge as well as the nature and rate of decoherence. The scheme is based on monitoring

the time-averaged charge-distribution in the coupled-DB pair.

Our scheme has three components: an atomic force microscope (AFM) capacitively-coupled to a DBP^-, a DC potential-bias applied along the DBP^-, and a tunable mid-infrared (MIR) driving field that is capable of inducing Rabi frequency in our system. In this scheme, the time-averaged charge distribution of the DBP^- is monitored by the AFM tip, while driving the DBP^- by the MIR field concomitantly with sweeping the applied bias from a negative value to its positive counterpart. When the driving field becomes resonant with the bias-imposed DBP^- tunneling rate, the time-averaged charge distribution becomes symmetric between the two DB sites (despite the strength of the bias applied), which leads to resonant peaks in the AFM read-out signal. From these resonant features we can extract the tunneling and decoherence rates of the DBP^- excess-charge.

We developed a theory describing the role of all the components involved in our scheme. For a chosen DBP^-, we specified the values that each component should have in an experiment in order to detect the DBP^- excess-charge dynamics. Also, we assumed that our system is ideal and thus analyzed it in the absence of any sources of noise. Then, we modified our theoretical model by including the effect of dominant sources of noise. Our scheme will enable in-depth studies of quantum coherent transport of electrons between dangling bonds on the silicon surface and enable the study of phonons and other interactions.

7.2 Future work

Experimental observation of coupled-DB pairs on the Si surface has provided a new and interesting topic of study that has the potential to bridge quantum information and computation with nanotechnology. I pursued three objectives during the course of my studies, but this topic certainly has the potential to lead many short- and long-term future research objectives. In the following, I suggest some of the future work that can branch from the objectives summarized above.

1. Considering that a DBP^- has the potential to be employed as a charge qubit, a logical step forward would be to further develop quantum computing implementations with the need to fully address all DiVincenzo's criteria [18] for such architectures. Possible computing schemes suitable for our DBP^- charge qubit can be a four-rail flying qubit model analogous to the one for nuclei-spin qubits in the bulk silicon [75], or a one-way quantum computing scheme [154], where the qubits are stationary.

2. Addressing all DiVincenzo criteria will of course require much elaboration. For instance, ways to introduce fresh, initialized DBP^-s; schemes to ensure that DBP^- phases are properly tracked and gates are correctly applied; the scalability of the system; how DBP^- qubits can be effectively moved over spin chains to enact interactions in a flying circuit model; and possibly incorporating readout during the computation for the purpose of quantum error correction.

3. Short-term efforts can focus on developing ways to investigate a small number of DBP^-s, both theoretically and experimentally. For instance, from theoretical aspects, instead of idealizing the charge qubits at the outset and using standard quantum circuit theory, we can use the extended Hubbard model to characterize idealized proposals for charge-qubit circuits using this second-quantized description with short- and medium-range interactions. In particular we can study how one- and two-qubit gates would perform for realistic systems. We can apply our theory to a three-qubit system, such as teleportation of a single charge qubit. In a further step, we can simulate non-unitary forms of single- and two-qubit gate operations by incorporating noises in our system.

4. Another potential direction for new investigations is to find ways to tune and

control the potential-barrier height between DBs. This is especially important for the purpose of controlling DBs interaction as it can facilitate and help with turning on and off the gate operations and also controlling the qubit measurement. Tuning the potential barrier may be achieved by changing the doping level, applying controllable molecular attachments, or using nano-size electrodes in order to vary the local electrostatic potential. Each of these approaches opens up a new topic of study on its own.

5. As mentioned earlier, the scaling advantage of the DBP^- qubit comes at the price of having to achieve rapid gating control, which entails some technical obstacles such as scaling down the nanowire network required for biasing qubits and accurate control of the amplitudes of the pulsed fields. Such a fast and spatially precise control is beyond the current capability of standard electronics, but in principle is conceivable by placing a suitable pattern of metallic nanowires near the surface and irradiating it with a laser pulse. The resulting electromagnetic field, created via plasmonic action [170], can bias the surface with a temporal control comparable to the duration of the pulse, which can be as short as femtoseconds. Different gates could be affected by time-varying biases achieved by controlled laser pulses. This problem of fast control by its own can be a new subject of studies at the graduate level.

6. *Ab initio* DFT calculations can be applied to larger Si clusters, though at the price of requiring more computational resources. However, it is worth trying as it helps to collect more data (by running calculations for more DBP^- configurations) and thus providing a more accurate insight on the effect of the Si surface on the coherence of DBP^-. Furthermore, a larger cluster can accommodate more than two DBs. Thus, one can develop new theories for the coherence and bonding of coupled DBs with the help of the results. These

results can be used for understanding and analyzing possible single- and two-qubit gate operations applied to the DB-pairs. Also, it helps to develop new theories for the quantum cellular automata unit cells.

7. Following our proposed scheme for measuring DBP^- coherent dynamics, the next step forward is to test this scheme experimentally. Based on our theoretical estimations one can reveal DBP^- coherence rate as well as the nature and rate of decoherence. In our studies, we assumed a weak coupling between the DBP^- and its surrounding environment and used the spin-boson model to estimate the decoherence rate. However, if the data collected from the experiment does not match the theory then we need to employ a different noise model to test and find the nature of our system's decoherence mechanism.

8. So far, we focused only on the hydrogen-terminated Si(100)–2×1, as this surface is one of the most commonly used surface orientations in the Si-wafer fabrication technology [36]. However, dangling bonds can reside on other Si surfaces and other types of semiconductors, thus providing an opportunity for investigating the properties of coupled DBs on other semiconductor surfaces as well.

Finally, since the dangling bond systems are promising building blocks for quantum engineering of novel devices, a detailed quantitative analysis of the electron dynamics in dangling bond assemblies is an important step forward.

Bibliography

[1] M. B. Haider, J. L. Pitters, G. A. DiLabio, L. Livadaru, J. Y. Mutus, and R. A. Wolkow. Controlled coupling and occupation of Silicon atomic quantum dots at room temperature. *Phys. Rev. Lett.*, 102:046805, 2009.

[2] L. Livadaru, P. Xue, Z. Shaterzadeh-Yazdi, G. A. DiLabio, J. Mutus, J. L. Pitters, B. C. Sanders, and R. A. Wolkow. Dangling-bond charge qubit on a Silicon surface. *New J. Phys.*, 12:083018, 2010.

[3] Z. Shaterzadeh-Yazdi, L. Livadaru, M. Taucer, J. Mutus, J. Pitters, R. A. Wolkow, and B. C. Sanders. Characterizing the rate and coherence of single-electron tunneling between two dangling bonds on the surface of silicon. *Phys. Rev. B*, 89:035315, 2014.

[4] P. W. Shor. Algorithms for quantum computation: discrete logarithms and factoring. In *Proc. 35th Ann. Sym. Fnd. of Comp. Sc*, SFCS '94, pages 124–134, Washington, DC, USA, 1994. IEEE Computer Society.

[5] L. K. Grover. Quantum mechanics helps in searching for a needle in a haystack. *Phys. Rev. Lett.*, 79(2):325, 1997.

[6] Y. Nakamura, Yu. A. Pashkin, and J. S. Tsai. Coherent control of macroscopic quantum states in a single-Cooper-pair box. *Nature (London)*, 398:786–788, 1999.

[7] V. Bouchiat, D. Vion, P. Joyez, D. Esteve, and M. H. Devoret. Quantum coherence with a single Cooper pair. *Phys. Scr.*, T76:165–170, 1998.

[8] A. Wallraff, D. I. Schuster, A. Blais, L. Frunzio, J. Majer, M. H. Devoret, S. M. Girvin, and R. J. Schoelkopf. Approaching unit visibility for control of a superconducting qubit with dispersive readout. *Phys. Rev. Lett.*, 95:060501, 2005.

[9] B. E. Kane. A silicon-based nuclear spin quantum computer. *Nature*, 393:133–37, 1998.

[10] T. Hayashi, T. Fujisawa, H. D. Cheong, Y. H. Jeong, and Y. Hirayama. Coherent manipulation of electronic states in a double quantum dot. *Phys. Rev. Lett.*, 91(22):226804, 2003.

[11] J. Gorman, D. G. Hasko, and D. A. Williams. Charge-qubit operation of an isolated double quantum dot. *Phys. Rev. Lett.*, 95(9):090502, 2005.

[12] R. Vrijen, E. Yablonovitch, K. Wang, H. W. Jiang, A. Balandin, V. Roychowdhury, T. Mor, and D. DiVincenzo. Electron-spin-resonance transistors for quantum computing in silicon-germanium heterostructures. *Phys. Rev. A*, 62:012306, 2000.

[13] S. D. Barrett and G. J. Milburn. Measuring the decoherence rate in a semiconductor charge qubit. *Phys. Rev. B*, 68:155307, 2003.

[14] B. C. Sanders, L. C. L. Hollenberg, D. Edmundson, and A. Edmundson. Visualizing a silicon quantum computer. *New J. Phys.*, 10:125005, 2008.

[15] D. Loss and D. P. DiVincenzo. Quantum computation with quantum dots. *Phys. Rev. A*, 57(1):120, 1998.

[16] M. Fuechsle, J. A. Miwa, S. Mahapatra, H. Ryu, S. Lee, O. Warschkow, L. C. L. Hollenberg, G. Klimeck, and M. Y. Simmons. A single-atom transistor. *Nat. Nanotechnol.*, 7:242–246, 2012.

[17] S. Mahapatra, H. Büch, and M. Y. Simmons. Charge sensing of precisely positioned P donors in Si. *Nano Lett.*, 11(10):4376–4381, 2011.

[18] D. P. DiVincenzo. Quantum computation. *Science*, 270:255, 1995.

[19] D. P. DiVincenzo and P. W. Shor. Fault-tolerant error correction with efficient quantum codes. *Phys. Rev. Lett.*, 77:3260, 1996.

[20] A. M. Steane. Overhead and noise threshold of fault-tolerant quantum error correction. *Phys. Rev. A*, 68:042322, 2003.

[21] J. M. Elzerman, R. Hanson, L. H. Willems van Beveren, B. Witkamp, L. M. K. Vandersypen, and L. P. Kouwenhoven. Single-shot read-out of an individual electron spin in a quantum dot. *Nature (London)*, 430:431–435, 2004.

[22] L. C. L. Hollenberg, A. S. Dzurak, C. Wellard, A. R. Hamilton, D. J. Reilly, G. J. Milburn, and R. G. Clark. Charge-based quantum computing using single donors in semiconductors. *Phys. Rev. B*, 69(11):113301, 2004.

[23] T. Fujisawa, T. Hayashi, and Y. Hirayama. Controlled decoherence of a charge qubit in a double quantum dot. *J. Vac. Sci. Technol. B*, 22:2035, 2004.

[24] J. L. Pitters, L. Livadaru, M. B. Haider, and R. A. Wolkow. Tunnel coupled dangling bond structures on hydrogen terminated silicon surfaces. *J. Chem. Phys.*, 134(064712):1–6, 2011.

[25] R. A. Wolkow, L. Livadaru, J. Pitters, M. Taucer, P. Piva, M. Salomons, M. Cloutier, and B. Vieira Cunha Martins. Silicon atomic quantum dots enable beyond-CMOS electronics. arXiv:1310.4148v1 [cond-mat.str-el], 2013.

[26] X. Tong and R. A. Wolkow. Electron-induced H atom desorption patterns created with a scanning tunneling microscope: Implications for controlled atomic-scale patterning on H-Si(100). *Surf. Sci.*, 600:L199–L203, 2006.

[27] M. McEllistrem, M. Allgeier, and J. J. Boland. Dangling bond dynamics on the Silicon(100)-2$\times$1 surface: Dissociation, diffusion, and recombination. *Science*, 279:545, 1998.

[28] E. J. Buehler and J. J. Boland. Dimer preparation that mimics the transition state for the adsorption of H_2 on the Si(100)-2×1 surface. *Science*, 290:506, 2000.

[29] B. P. Lemke and D. Haneman. Dangling bonds on silicon. *Phys. Rev. B*, 17:1893, 1978.

[30] J. T. Yates. Surface chemistry of silicon-the behaviour of dangling bonds. *J. Phys.: Condens. Matter*, 3:S143–S156, 1991.

[31] W. Ye, K. Min, P. Peña Martin, A. A. Rockett, N. R. Aluru, and J. W. Lyding. Scanning tunneling spectroscopy and density functional calculation of silicon dangling bonds on the Si(100)-2×1:H surface. *Surf. Sci.*, 609:147–151, 2013.

[32] J. Zikovsky, S. A. Dogel, M. H. Salomons, J. L. Pitters, G. A. DiLabio, and R. A. Wolkow. Indications of field-directing and self-templating effects on the formation of organic lines on silicon. *J. Chem. Phys.*, 134:114707, 2011.

[33] R. Robles, M. Kepenekian, S. Monturet, C. Joachim, and N. Lorente. Energetics and stability of dangling-bond silicon wires on H passivated Si(100). *J. Phys.: Condens. Matt.*, 24(445004), 2012.

[34] S. R. Schofield, P. Studer, C. F. Hirjibehedin, N. J. Curson, G. Aeppli, and D. R. Bowler. Quantum engineering at the silicon surface using dangling bonds. *Nature Commun.*, 4(1649), 2013.

[35] M. A. Walsh and M. C. Hersam. Atomic-scale templates patterned by ultrahigh vacuum scanning tunneling microscopy in silicon. *Annu. Rev. Chem.*, 60:193–216, 2009.

[36] W. C. O'Mara, R. B. Herring, and L. P. Hunt. *Handbook of Semiconductor Silicon Technology.* NOYES Publications, Park Ridge, New Jersey, 1990.

[37] B. D. Thoms and J. E. Butler. HREELS and LEED of H/C(100): the 2×1 monohydride dimer row reconstruction. *Surf. Sci.*, 328:291, 1995.

[38] A. J. Leggett, S. Chakravarty, A. T. Dorsey, M. P. A. Fisher, A. Garg, and W. Zwerger. Dynamics of the dissipative two-state system. *Rev. Mod. Phys.*, 59(1):1–85, 1987.

[39] A. O. Caldeira and A. J. Leggett. Influence of dissipation on quantum tunneling in macroscopic systems. *Phys. Rev. Lett.*, 46:211, 1981.

[40] S. E. S. Andresen, R. Brenner, C. J. Wellard, C. Yang, T. Hopf, C. C. Escott, R. G. Clark, A. S. Dzurak, D. N. Jamieson, and L. C. L. Hollenberg. Charge state control and relaxation in an atomically doped silicon device. *Nano. Lett.*, 7(7):2000–2003, 2007.

[41] A. Y. Kitaev. Fault-tolerant quantum computation by anyons. *Ann. Phys.*, 303:2–30, 2003.

[42] J. Hubbard. Generalized Wigner lattices in one dimension and some applications to tetracyanoquinodimethane (TCNQ) salts. *Phys. Rev. B*, 17(2):494, 1978.

[43] P. Hohenberg and W. Kohn. Inhomogeneous electron gas. *Phys. Rev.*, 136:B864–B871, 1964.

[44] J. B. Foresman and Frish A. *Exploring Chemistry with Electronic Structure Methods: a Guide to Using Gaussian.* Gaussian Inc., Pittsbrugh, PA, USA, second edition, 1996.

[45] M. A. L. Marques and E. K. U. Gross. Time-dependent density functional theory. *Ann. Rev. Phys. Chem.*, 55:427–455, 2004.

[46] J. Gardner, S. D. Bennett, and A. A. Clerk. Mechanically probing coherent tunneling in a double quantum dot. *Phys. Rev. B*, 84:205316, 2011.

[47] J. R. Petta, A. C. Johnson, C. M. Marcus, M. P. Hanson, and A. C. Gossard. Manipulation of a single charge in a double quantum dot. *Phys. Rev. Lett.*, 93(18):186802, 2004.

[48] T. M. Stace, A. C. Doherty, and S. D. Barrett. Population inversion of a driven two-level system in a structureless bath. *Phys. Rev. Lett.*, 95:106801, 2005.

[49] J. Zhu, M. Brink, and P. L. McEuen. Frequency shift imaging of quantum dots with single-electron resolution. *Appl. Phys. Lett.*, 87:242102, 2005.

[50] F. J. Giessibl. Advances in atomic force microscopy. *Rev. Mod. Phys.*, 75:949–983, 2003.

[51] J. L . Pitters, I. A. Dogel, and R. A. Wolkow. Charge control of surface dangling bonds using nanoscale Schottky contacts. *ACS Nano*, 5(3):1984–1989, 2011.

[52] W. C. O'Mara, R. B. Herring, and L. P. Hunt, editors. *Handbook of Semiconductor Silicon Technology.* Noyes Publications, Park Ridge, New Jersey, USA, 1st edition, 1990.

[53] K. Oura, V. G. Lifshits, A. Saranin, A. V. Zotov, and M. Katayama, editors. *Surface Science: an Introduction.* Springer-Verlag, Berlin, 1st edition, 2003.

[54] Y. Matsuda, J. Tahir-Kheli, and W. A. Goddard. Surface and electronic properties of hydrogen terminated Si [001] nanowires. *J. Phys. Chem. C*, 115:12586–12591, 2011.

[55] W. Spitzer and H. Y. Fan. Infrared absorption in n-type silicon. *Phys. Rev.*, 108:268–271, 1957.

[56] W. Kress and F. W. de Wette, editors. *Study of Surface Phonons by the Slab Method.* Springer-Verlag, Berlin Heidelberg, 1991.

[57] J. Szeftel. Surface phonon dispersion, using electron energy loss spectroscopy. *Surf. Sci.*, 152-153:797–810, 1985.

[58] P. Brüesch, editor. *Phonons: Theory and Experiments I.* Springer, Berlin Heidelberg, 1982.

[59] B. C. Daly, K. Kang, Y. Wang, and David G. Cahill. Picosecond ultrasonic measurements of attenuation of longitudinal acoustic phonons in silicon. *Phys. Rev. B*, 80:174112, 2009.

[60] J. J. Letcher, K. Kang, D. G. Cahill, and D. D. Dlott. Effects of high carrier densities on phonon and carrier lifetimes in Si by time-resolved anti-Stokes Raman scattering. *Appl. Phys. Lett.*, 90(25):1–3, 2007.

[61] G. Lucovsky, R. J. Nemanich, and J. C. Knights. Structural interpretation of the vibrational spectra of a-Si: H alloys. *Phys. Rev. B*, 19(4):2064, 1979.

[62] G. Lucovsky. Relation of Si-H vibrational frequencies to surface bonding geometry. *J. Vac. Sci. Technol.*, 16(5):1225–1228, 1979.

[63] I. Tamm. On the possible bound states of electrons on a crystal surface. *Phys. Z. Sowjet.*, 1:733–735, 1932.

[64] J. Bardeen. Surface states and rectification at a metal semi-conductor contact. *Phys. Rev.*, 71:717–727, 1947.

[65] A. H. Edwards. Interaction of H and H_2 with the silicon dangling orbital at the $\langle 111 \rangle$ Si/SiO_2 interface. *Phys. Rev. B*, 44:1832, 1991.

[66] T. C. G. Reusch, M. W. Radny, P. V. Smith, O. Warschkow, N. A. Marks, N. J. Curson, D. R. McKenzie, and M. Y. Simmons. Single phosphorous atoms in Si(001): doping-induced charge transfer into isolated si dangling bonds. *J. Phys. Chem. C*, 111:6428–6433, 2007.

[67] L. Livadaru, J. Pitters, M. Taucer, and R. A. Wolkow. Theory of nonequilibrium single-electron dynamics in stm imaging of dangling bonds on a hydrogenated silicon surface. *Phys. Rev. B*, 84:205416, 2011.

[68] C. R. Helms and E. H. Poindexter. The silicon-silicon dioxide system: Its microstructure and imperfections. *Rep. Prog. Phys.*, 57(8):791–852, 1994.

[69] L. Liu, J. Yu, and J. W. Lyding. Scanning tunneling microscopy observation of single dangling bonds on the Si(100)-2×1:H Surface. *MRS Proceedings*, 705, 2001.

[70] M. Taucer, L. Livadaru, P. G. Piva, R. Achal, H. Labidi, J. Pitters, and R. A. Wolkow. Single electron charging dynamics of atomic silicon quantum dots on the H-Si(100) surface. arXiv:1305.3597v1 [cond-mat.mes-hall], 2014.

[71] E. T. Foley, A. F. Kam, J. W. Lyding, and Ph. Avouris. Cryogenic UHV-STM study of hydrogen and deuterium desorption from Si(100). *Phys. Rev. Lett.*, 80:1336–1339, 1998.

[72] G. P. Lopinski, D. D. M. Wayner, and R. A. Wolkow. Self-directed growth of molecular nanostructures on silicon. *Nature*, 406:48–51, 2000.

[73] S. A. Dogel, G. A. DiLabio, J. Zikovsky, J. L. Pitters, and R. A. Wokow. Experimental and theoretical studies of trimethylene sulfide-derived nanostructures on p- and n-type H-Silicon(100)-2×1. *J. Phys. Chem. C*, 111:11965–11969, 2007.

[74] D. P. Divincenzo. The physical implementation of quantum computation. *Fortschr. Phys.*, 48:771–783, 2000.

[75] L. C. L. Hollenberg, A. D. Greentree, A. G. Fowler, and C. J. Wellard. Two-dimensional architectures for donor-based quantum computing. *Phys. Rev. B*, 74(4):45311, 2006.

[76] X. Hu, B. Koiller, and S. Das Sarma. Charge qubits in semiconductor quantum computer architecture: Tunnel coupling and decoherence. *Phys. Rev. B*, 71:235332, 2005.

[77] Z. Shi, C. B. Simmons, D. R. Ward, J. R. Prance, R. T. Mohr, T. S. Koh, J. K. Gamble, X. Wu, D. E. Savage, M. G. Lagally, M. Friesen, S. N. Coppersmith, and M. A. Eriksson. Coherent quantum oscillations and echo measurements of a si charge qubit. *Phys. Rev. B*, 88:075416, 2013.

[78] Y. Dovzhenko, J. Stehlik, K. D. Petersson, J. R. Petta, H. Lu, and A. C. Gossard. Nonadiabatic quantum control of a semiconductor charge qubit. *Phys. Rev. B*, 84:161302, 2011.

[79] K. D. Petersson, J. R. Petta, H. Lu, and A. C. Gossard. Quantum coherence in a one-electron semiconductor charge qubit. *Phys. Rev. Lett.*, 105(24):246804, 2010.

[80] C. A. Stafford and Ned S. Wingreen. Resonant photon-assisted tunneling through a double quantum dot: an electron pump from spatial rabi oscillations. *Phys. Rev. Lett.*, 76:1916, 1996.

[81] S. D. Barrett and T. M. Stace. Continuous measurement of a microwave-driven solid state qubit. *Phys. Rev. Lett.*, 96(1):017405, 2006.

[82] R. J. Warburton. Single spins in self-assembled quantum dots. *Nat. Mater.*, 12:483–493, 2013.

[83] K. Saeedi, S. Simmons, J. Z. Salvail, P. Dluhy, H. Riemann, N. V. Abrosimov, P. Becker, H.-J. Pohl, J. J. L. Morton, and M. L. W. Thewalt. Room-temperature quantum bit storage exceeding 39 minutes using ionized donors in silicon-28. *Science*, 342:830, 2013.

[84] A. V. Khaetskii, D. Loss, and L. Glazman. Electron spin decoherence in quantum dots due to interaction with nuclei. *Phys. Rev. Lett.*, 88:186802, 2002.

[85] D. A. Lidar, I. L. Chuang, and K. B. Whaley. Decoherence-free subspaces for quantum computation. *Phys. Rev. Lett.*, 81:2594, 1998.

[86] H. Bluhm, S. Foletti, I. Neder, M. Rudner, D. Mahalu, V. Umansky, and A. Yacoby. Dephasing time of GaAs electron-spin qubits coupled to a nuclear bath exceeding 200μsec. *Nat. Phys.*, 7:109–113, 2011.

[87] M. Steger, K. Saeedi, M. L. W. Thewalt, J. J. L. Morton, H. Riemann, N. V. Abrosimov, P. Becker, and H.-J. Pohl. Quantum information storage for over 180 s using donor spins in a ^{28}si semiconductor vacuum. *Science*, 336(6086):1280, 2012.

[88] A. Blais, R. Huang, A. Wallraff, S. M. Girvin, and R. J. Schoelkopf. Cavity quantum electrodynamics for superconducting electrical circuits: An architecture for quantum computation. *Phys. Rev. A*, 69:062320, 2004.

[89] A. Wallraff, D. I. Schuster, A. Blais, L. Frunzio, R.-S. Huang, J. Majer, S. Kumar, S. M. Girvin, and R. J. Schoelkopf. Strong coupling of a single photon to a superconducting qubit using circuit quantum electrodynamics. *Nature*, 431:162–167, 2004.

[90] C. Rigetti, J. M. Gambetta, S. Poletto, B. L. T. Plourde, J. M. Chow, A. D. Córcoles, J. A. Smolin, S. T. Merkel, J. R. Rozen, G. A. Keefe, M. B. Rothwell, M. B. Ketchen, and M. Steffen. Superconducting qubit in a waveguide cavity with a coherence time approaching 0.1 ms. *Phys. Rev. B*, 86:100506, 2012.

[91] H. Paik, D. I. Schuster, Lev S. Bishop, G. Kirchmair, G. Catelani, A. P. Sears, B. R. Johnson, M. J. Reagor, L. Frunzio, L. I. Glazman, S. M. Girvin, M. H. Devoret, and R. J. Schoelkopf. Observation of high coherence in Josephson junction qubits measured in a three-dimensional circuit QED architecture. *Phys. Rev. Lett.*, 107:240501, 2011.

[92] J. A. Schreier, A. A. Houck, Jens Koch, D. I. Schuster, B. R. Johnson, J. M. Chow, J. M. Gambetta, J. Majer, L. Frunzio, M. H. Devoret, S. M. Girvin, and R. J. Schoelkopf. Suppressing charge noise decoherence in superconducting charge qubits. *Phys. Rev. B*, 77:180502, 2008.

[93] D. Baeriswyl, D. K. Campbell, J. M. P. Carmelo, F. Guinea, and E. Louis, editors. *The Hubbard Model: Its Physics and Its Mathematical Physics.* Plenum Press, New York, 1995.

[94] H. A. Gersch and G. C. Knollman. Quantum cell model for bosons. *Phys. Rev.*, 129:959–967, 1963.

[95] S.-J. Gu, S.-S. Deng, Y.-Q. Li, and H.-Q. Lin. Entanglement and quantum phase transition in the extended hubbard model. *Phys. Rev. Lett.*, 93:086402, 2004.

[96] T. Esslinger. Fermi-Hubbard physics with atoms in an optical lattice. *Annu. Rev. Condens. Mat. Phys.*, 1:129–152, 2010.

[97] E. S. Caixeiro and A. Troper. Superconductivity and hybridization in a two-dimensional extended Hubbard model: Strong coupling regime. *J. Magn. Magn. Mater.*, 320(14):e490 – e492, 2008.

[98] S. Onari, R. Arita, K. Kuroki, and H. Aoki. Phase diagram of the two-dimensional extended Hubbard model:phase transitions between different pairing symmetries when charge and spin fluctuations coexist. *Phys. Rev. B*, 70:094523, 2004.

[99] M. J. Hornbach and Y. Dakhnovskii. Electron transfer in a slow relaxation bath: Coherence and nonexponential kinetics. *J. Chem. Phys.*, 111:5073, 1999.

[100] A. Garg, J. N. Onuchic, and V. Ambegaokar. Effect of friction on electron transfer in biomolecules. *J. Chem. Phys.*, 83:4491, 1985.

[101] J. J. Sakurai and J. Napolitano. *Modern Quantum Mechanics.* Addison-Wesley, San Francisco, second edition, 1993.

[102] D. J. Griffiths. *Introduction to Quantum Mechanics.* Prentice Hall, New Jersey, 1995.

[103] L. Cockins, Y. Miyahara, S. D. Bennett, A. A. Clerk, S. Studenikin, P. Poole, A. Sachrajda, and P. Grutter. Energy levels of few-electron quantum dots imaged and characterized by atomic force microscopy. *Proc. Nat. Acad. Sci. U.S.A*, 107(21):9496–9501, 2010.

[104] L. Cockins, Y. Miyahara, S. D. Bennett, A. A. Clerk, and P. Grutter. Excited-state spectroscopy on an individual quantum dot using atomic force microscopy. *Nano Lett.*, 12(2):709–713, 2012.

[105] F. Marchi, R. Dianoux, H. J. H. Smilde, P. Mur, F. Comin, and J. Chevrier. Characterisation of trapped electric charge carriers behaviour at nanometer scale by electrostatic force microscopy. *J. Electrostat.*, 66(9-10):538–547, 2008.

[106] S. Morita, F. J. Giessibl, and R. Wiesendanger, editors. *Noncontact Atomic Force Microscopy.* Springer-Verlag, Berlin, 2009.

[107] L. Gross, F. Mohn, P. Liljeroth, J. Repp, F. J. Giessibl, and G. Meyer. Measuring the charge state of an adatom with noncontact atomic force microscopy. *Science*, 324(5933):1428, 2009.

[108] M. Schneiderbauer, D. Wastl, and F. J. Giessibl. qPlus magnetic force microscopy in frequency-modulation mode with millihertz resolution. *Beilstein J. Nanotechnol.*, 3(1):174–178, 2012.

[109] K. Kobayashi, H. Yamada, and K. Matsushige. Reduction of frequency noise and frequency shift by phase shifting elements in frequency modulation atomic force miscroscopy. *Rev. Sci. Instrum.*, 82:1–9, 2011.

[110] C. Bai. *Scanning Tunneling Microscopy and Its Applications.* Springer-Verlag, New York, 2000.

[111] C. J. Chen. *Introduction to Scanning Tunneling Microscopy.* Oxford University Press, New York, 1993.

[112] D. A. Bonnell, editor. *Scanning Probe Microscopy and Spectroscopy: Theory, Techniques, and Applications.* Wiley-VCH, New York, 2001.

[113] Z. Zhang and J. T. Yates. Band bending in semiconductors: chemical and physical consequences at surfaces and interfaces. *Chem. Rev.*, 112:5520–5551, 2012.

[114] X. Tong and R. A. Wolkow. Scanning tunneling microscopy characterization of low-profile crystalline TiSi2 microelectrodes on a Si(111) surface. *Appl. Phys. Lett.*, 86(20):1–3, 2005.

[115] R. M. Feenstra. Electrostatic potential for a hyperbolic probe tip near a semiconductor. *J. Vac. Sci. Technol. B*, 21(5):2080–2088, 2003.

[116] P. G. Piva, G. A. Dilabio, J. L. Pitters, J. Zikovsky, M. Rezeq, S. Dogel, W. A. Hofer, and R. A. Wolkow. Field regulation of single-molecule conductivity by a charged surface atom. *Nature (London)*, 435:658–661, 2005.

[117] F. K. Tittel, D. Richter, and A. Fried. Mid-infrared laser applications in spectroscopy. *Top. Appl. Phys.*, 89:458–529, 2003.

[118] R. F. Curl and F. K. Tittel. Tunable infrared laser spectroscopy. *Annu. Rep. Prog. Chem, Sect. C: Phys. Chem*, 98:219, 2002.

[119] Y. Yao, A. J. Hoffman, and C. F. Gmachi. Mid-infrared quantum cascade lasers. *Nat. Photonics*, 6(7):432–439, 2012.

[120] W. Kohn and L. J. Sham. Self-consistent equations including exchange and correlation effects. *Phys. Rev.*, 140:A1133–A1138, 1965.

[121] Density functional Methods. Gaussian 09 user's reference @ONLINE. `http://www.gaussian.com/g_tech/g_ur/k_dft.htm`, 2013.

[122] D. M. Ceperley and B. J. Alder. Ground state of the electron gas by a stochastic method. *Phys. Rev. Lett.*, 45:566–569, 1980.

[123] A. D. Becke. A new mixing of Hartree-Fock and local density-functional theories. *J. Chem. Phys.*, 98:1372–1377, 1993.

[124] A. D. Becke. Density-functional thermochemistry. III. The role of exact exchange. *J. Chem. Phys.*, 98(7):5648–5652, 1993.

[125] S. H. Vosko, L. Wilk, and M. Nusair. Accurate spin-dependent electron liquid correlation energies for local spin density calculations: A critical analysis. *Can. J. Phys.*, 58(8):1200–1211, 1980.

[126] C. Lee, W. Yang, and R. G. Parr. Development of the colle-salvetti correlation-energy formula into a functional of the electron density. *Phys. Rev. B*, 37(2):785–789, 1988.

[127] J. C. Grossman. Benchmark quantum monte carlo calculations. *J. Phys. Chem.*, 117(4):1434–1440, 2002.

[128] A. D. Becke. Density-functional exchange-energy approximation with correct asymptotic behavior. *Phys. Rev. A*, 38:3098, 1988.

[129] Y. Zhao and D. G. Truhlar. The M06 suite of density functionals for main group thermochemistry, thermochemical kinetics, noncovalent interactions, excited states, and transition elements: two new functionals and systematic testing of four M06-class functionals and 12 other functionals. *Theor. Chem. Account*, 120:215–241, 2008.

[130] G. G. Hall. The Lennard-Jones paper of 1929 and the foundations of Molecular Orbital Theory. *Adv. Quantum Chem.*, 22:1–6, 1991.

[131] L. A. Curtiss, K. Raghavachari, P. C. Redfern, and J. A. Pople. Assessment of Gaussian-3 and density functional theories for a larger experimental test set. *J. Chem. Phys.*, 112(17):7374–7383, 2000.

[132] O. Warschkow, T. L. McDonell, and Marks N. A. NH3 on Si(001): Can gaussian cluster and planewave slab models agree on energetics? *Surf. Sci.*, 601(14):3020 – 3033, 2007.

[133] C. S. Garoufalis and A. D. Zdetsis. Real space optical gap calculations in oxygenated Si nanocrystals. *J. Phys.: Conf. Ser.*, 10(1):69, 2005.

[134] C. Lin, W. Cheng, J. Wang, and R. Zhang. Size and hydrogen saturation effects on third-order polarizabilities of Si clusters. *Chem. Phys. Lett.*, 509(4–6):124–128, 2011.

[135] J. Bai, X. C. Zeng, H. Tanaka, and J. Y. Zeng. Metallic single-walled silicon nanotubes. *Proceedings of the National Academy of Sciences of the United States of America*, 101(9):2664–2668, 2004.

[136] H. Kruse, L. Goerigk, and S. Grimme. Why the standard B3LYP/6-31G* model chemistry should not be used in DFT calculations of molecular thermochemistry: Understanding and correcting the problem. *J. Org. Chem.*, 77:10824–10834, 2012.

[137] I. Mayer and P. Valiron. Second order Mo/ller-Plesset perturbation theory without basis set superposition error. *J. Chem. Phys.*, 109(9):3360–3373, 1998.

[138] F. B. van Duijneveldt, J. G. C. M. van Duijneveldt-van de Rijdt, and J. H. van Lenthe. State of the art in counterpoise theory. *Chem. Rev.*, 94:1873–1885, 1994.

[139] R. Konecny and D.J. Doren. Cycloaddition reactions of unsaturated hydrocarbons on the Si(100)-(2×1) surface: theoretical predictions. *Surf. Sci.*, 417(2-3):169–188, 1998.

[140] I. Y. Zhang, J. Wu, and X. Xu. Extending the reliability and applicability of B3LYP. *Chem. Commun.*, 46:3057–3070, 2010.

[141] J. Paier, M. Marsman, and G. Kresse. Why does the B3LYP hybrid functional fail for metals? *J. Chem. Phys.*, 127:1–10, 2007.

[142] Z.-L. Cai, K. Sendt, and J. R. Reimers. Failure of density-functional theory and time-dependent density-functional theory for large extended systems. *J. Chem. Phys.*, 117:5543–5549, 2002.

[143] E. Runge and E. K. U. Gross. Density-functional theory for time-dependent systems. *Phys. Rev. Lett.*, 52:997, 1984.

[144] M. Lopez del Puerto, M. Jain, and j. R. Chelikowsky. Time-dependent density functional theory calculations for the stokes shift in hydrogenated silicon clusters. *Phys. Rev. B*, 81:035309, 2010.

[145] A. Dreuw and M. Head-Gordon. Failure of time-dependent density functional theory for long-range charge-transfer excited states: the ZincbacteriochlorinBacteriochlorin and BacteriochlorophyllSpheroidene complexes. *J. Am. Chem. Soc.*, 126:4007–4016, 2004.

[146] A. Dreuw and M. Head-Gordon. Single-reference ab initio methods for the calculation of excited states of large molecules. *Chem. Rev.*, 105:4009–4037, 2005.

[147] A. Dreuw, G. R. Fleming, and M. Head-Gordon. Charge-transfer state as a possible signature of a ZeaxanthinChlorophyll dimer in the non-photochemical quenching process in green plants. *J. Phys. Chem. B*, 107:6500–6503, 2003.

[148] A. L. Sobolewski and W. Domcke. Ab initio study of the excited-state coupled electron-proton-transfer process in the 2-aminopyridine dimer. *Chem. Phys.*, 294(1):73–83, 2003.

[149] M. J. Frisch, G. W. Trucks, H. B. Schlegel, G. E. Scuseria, M. A. Robb, J. R. Cheeseman, J. A. Montgomery, Jr., T. Vreven, K. N. Kudin, J. C. Burant, J. M. Millam, S. S.

Iyengar, J. Tomasi, V. Barone, B. Mennucci, M. Cossi, G. Scalmani, N. Rega, G. A. Petersson, H. Nakatsuji, M. Hada, M. Ehara, K. Toyota, R. Fukuda, J. Hasegawa, M. Ishida, T. Nakajima, Y. Honda, O. Kitao, H. Nakai, M. Klene, X. Li, J. E. Knox, H. P. Hratchian, J. B. Cross, V. Bakken, C. Adamo, J. Jaramillo, R. Gomperts, R. E. Stratmann, O. Yazyev, A. J. Austin, R. Cammi, C. Pomelli, J. W. Ochterski, P. Y. Ayala, K. Morokuma, G. A. Voth, P. Salvador, J. J. Dannenberg, V. G. Zakrzewski, S. Dapprich, A. D. Daniels, M. C. Strain, O. Farkas, D. K. Malick, A. D. Rabuck, K. Raghavachari, J. B. Foresman, J. V. Ortiz, Q. Cui, A. G. Baboul, S. Clifford, J. Cioslowski, B. B. Stefanov, G. Liu, A. Liashenko, P. Piskorz, I. Komaromi, R. L. Martin, D. J. Fox, T. Keith, M. A. Al-Laham, C. Y. Peng, A. Nanayakkara, M. Challacombe, P. M. W. Gill, B. Johnson, W. Chen, M. W. Wong, C. Gonzalez, and J. A. Pople. Gaussian 03, Revision C.02. Gaussian, Inc., Wallingford, CT, 2004.

[150] U. Bockelmann and G. Bastard. Phonon scattering and energy relaxation in two-, one-, and zero-dimensional electron gases. *Phys. Rev. B*, 42(14):8947–8951, 1990.

[151] H. M. Tütüncü, S. J. Jenkins, and G. P. Srivastava. Theoretical studies of atomic vibrations on the Si (001)(2× 1) surface. *Phys. Rev. B*, 56(8):4656, 1997.

[152] H. Benisty. Reduced electron-phonon relaxation rates in quantum-box systems: Theoretical analysis. *Phy. Rev. B*, 51(19):13281, 1995.

[153] A. Barenco, C. H. Bennett, R. Cleve, D. P. DiVincenzo, N. Margolus, P. Shor, T. Sleator, J. A. Smolin, and H. Weinfurter. Elementary gates for quantum computation. *Phys. Rev. A*, 52(5):3457, 1995.

[154] R. Raussendorf and H. J. Briegel. A one-way quantum computer. *Phys. Rev. Lett.*, 86(22):5188, 2001.

[155] A. Y. Anagaw, R. A. Wolkow, and G. A. DiLabio. Theoretical study of work function

modification by organic molecule-derived linear nanostructure on H–Silicon(100)–2×1. *J. Phys. Chem. C*, 112:3780–3784, 2008.

[156] M. J. Frisch, G. W. Trucks, H. B. Schlegel, G. E. Scuseria, M. A. Robb, J. R. Cheeseman, G. Scalmani, V. Barone, B. Mennucci, G. A. Petersson, H. Nakatsuji, M. Caricato, X. Li, H. P. Hratchian, A. F. Izmaylov, J. Bloino, G. Zheng, J. L. Sonnenberg, M. Hada, M. Ehara, K. Toyota, R. Fukuda, J. Hasegawa, M. Ishida, T. Nakajima, Y. Honda, O. Kitao, H. Nakai, T. Vreven, J. A. Montgomery, Jr., J. E. Peralta, F. Ogliaro, M. Bearpark, J. J. Heyd, E. Brothers, K. N. Kudin, V. N. Staroverov, R. Kobayashi, J. Normand, K. Raghavachari, A. Rendell, J. C. Burant, S. S. Iyengar, J. Tomasi, M. Cossi, N. Rega, J. M. Millam, M. Klene, J. E. Knox, J. B. Cross, V. Bakken, C. Adamo, J. Jaramillo, R. Gomperts, R. E. Stratmann, O. Yazyev, A. J. Austin, R. Cammi, C. Pomelli, J. W. Ochterski, R. L. Martin, K. Morokuma, V. G. Zakrzewski, G. A. Voth, P. Salvador, J. J. Dannenberg, S. Dapprich, A. D. Daniels, Ö. Farkas, J. B. Foresman, J. V. Ortiz, J. Cioslowski, and D. J. Fox. Gaussian 09 Revision A.1. Gaussian Inc. Wallingford CT 2009.

[157] P. Kinsler, P. Harrison, and R. W. Kelsall. Intersubband electron-electron scattering in asymmetric quantum wells designed for far-infrared emission. *Phys. Rev. B*, 58:4771–4778, 1998.

[158] N. R. Das, M. W. Shinwari, M. J. Deen, and J.-S. Lee. Electron states in a silicon nanowire in the presence of surface potential and field. *Nanotechnology*, 23(41):415201, 2012.

[159] Woodbridge (GB2) M. G. Burt. Quantum well structures. Patent, 1996. US 5481397.

[160] W. G. van der Wiel, S. De Franceschi, J. M. Elzerman, T. Fujisawa, S. Tarucha, and L. P. Kouwenhoven. Electron transport through double quantum dots. *Rev. Mod. Phys.*, 75:1–22, 2002.

[161] L. Allen and J. H. Eberly. *Optical Resonance and Two-Level Atoms*. John Wiley and Sons, New York, 1975.

[162] V. Raghunathan, R. Shori, O. M. Stafsudd, and B. Jalili. Nonlinear absorption in silicon and the prospects of mid-infrared silicon raman lasers. *phys. stat. sol. (a)*, 203(5):R38–R40, 2006.

[163] C. H. Schwalb, M. Lawrenz, M. Dürr, and U. Höfer. Real-space investigation of fast diffusion of hydrogen on Si (001) by a combination of nanosecond laser heating and STM. *Phys. Rev. B*, 75(8):085439, 2007.

[164] L. Cockins, Y. Miyahara, and P. Grutter. Spatially resolved low-frequency noise measured by atomic force microscopy. *Phys. Rev. B*, 79(12):121309, 2009.

[165] R. Stomp, Y. Miyahara, S. Schaer, Q. Sun, H. Guo, P. Grutter, S. Studenikin, Ph. Poole, and A. Sachrajda. Detection of single-electron charging in an individual inas quantum dot by noncontact atomic-force microscopy. *Phys. Rev. Lett.*, 94(5):056802, 2005.

[166] M. Rezeq, J. Pitters, and R. A. Wolkow. Tungsten nanotip fabrication by spatially controlled field-assisted reaction with Nitrogen. *J. Chem. Phys.*, 124(3):204716, 2006.

[167] L. N. Kantorovich, A. I. Livshits, and M. Stoneham. Electrostatic energy calculation for the interpretation of scanning probe microscopy experiments. *J. Phys.: Condens. Matter*, 12(6):795, 2000.

[168] F. J. Giessibl. Forces and frequency shifts in atomic-resolution dynamic-force microscopy. *Phys. Rev. B*, 56:16010, 1997.

[169] G. Lindblad. On the generators of quantum dynamical semigoups. *Comm. Math. Phys.*, 48:119–130, 1976.

[170] S. A. Maier and H. A. Atwater. Plasmonics: Localization and guiding of electromagnetic energy in metal/dielectric structures. *J. Appl. Phys.*, 98:011101, 2005.

Appendix A

Samples used for energy-splitting calculation

Below, we present all the Si-cluster models that we prepared for the purpose of evaluating the energy splitting of different DBP^- configurations, by means of *ab initio* (TD) DFT. Any individual box is representing the hydrogen-terminated Si(100)-2×1 surface. Each horizontal line in the box corresponds to a Si-Si dimer. Pair of red dots in each box represents a DBP^-, and the dot with letter P stands for the phosphorous atom doped within the clusters. The cluster size is shown by $n \times m$, where n is the number of rows and m is the number of Si-dimers per row.

DBP^- configurations are categorized based on the size of the cluster on which they are located. The name of each sample clearly shows the corresponding cluster size and the type of configuration, i.e. 'V' for vertical, 'H' for horizontal, and 'D' for diagonal. There are thirty-six cluster samples all together, which include all possible DBP^- configuration on these cluster sizes. Furthermore, depending on the type of configuration, a cluster can have *Cs*, or *C2* symmetry. Clusters with *Cs* have a mirror-plane symmetry, whereas clusters with *C2* symmetry does not change in shape under a rotation of 180 degrees around a rotational axis that is perpendicular to surface.

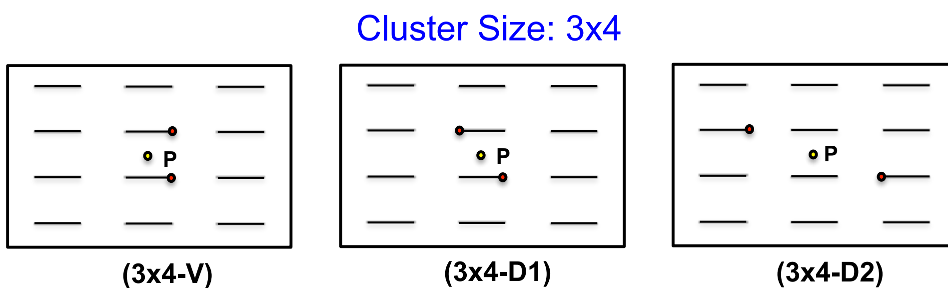

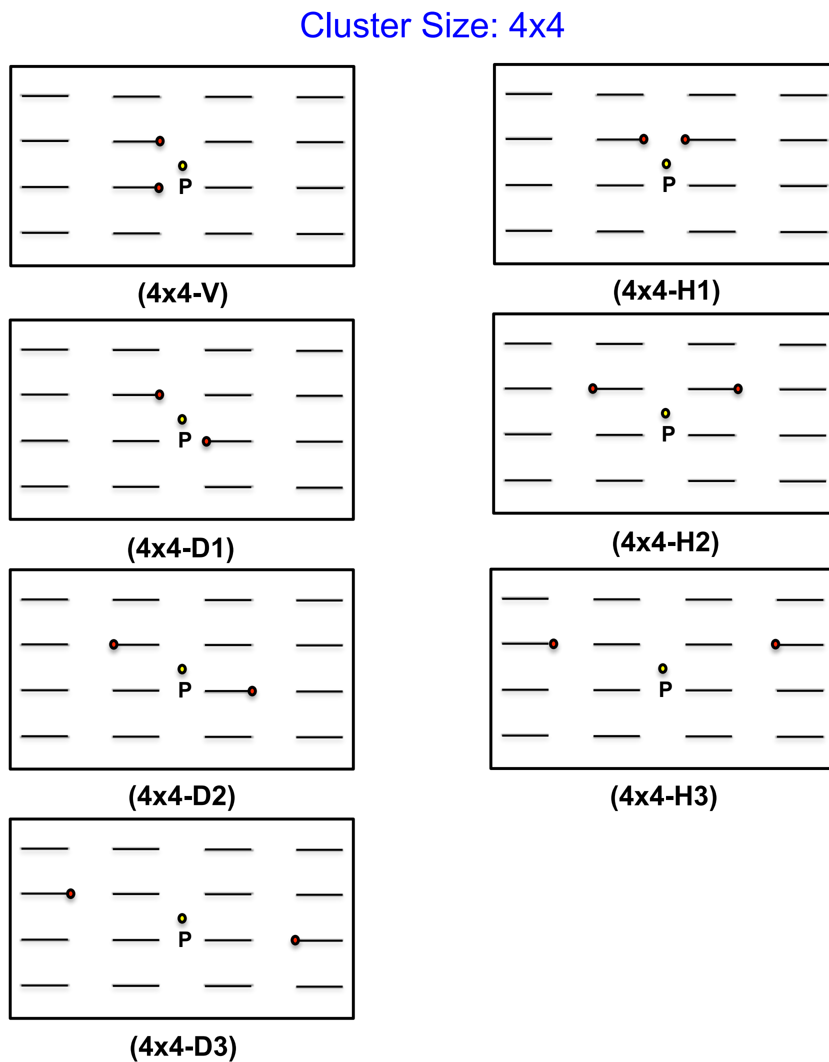

Figure A.1: DBP^- configurations on two different sizes of cluster: 3×4 (i.e. 3 rows with 4 silicon dimers per row) and 4×4 (i.e. 4 rows with 4 silicon dimers per row). The rectangular box represents Si(100)-2×1 surface of a desired cluster model; horizontal short lines in each box represent Si dimers, and the red and yellow small circles represent the DBs and the P dopant, respectively. The letters V, D, and H stand for vertical, diagonal, and horizontal DBP^- configurations.

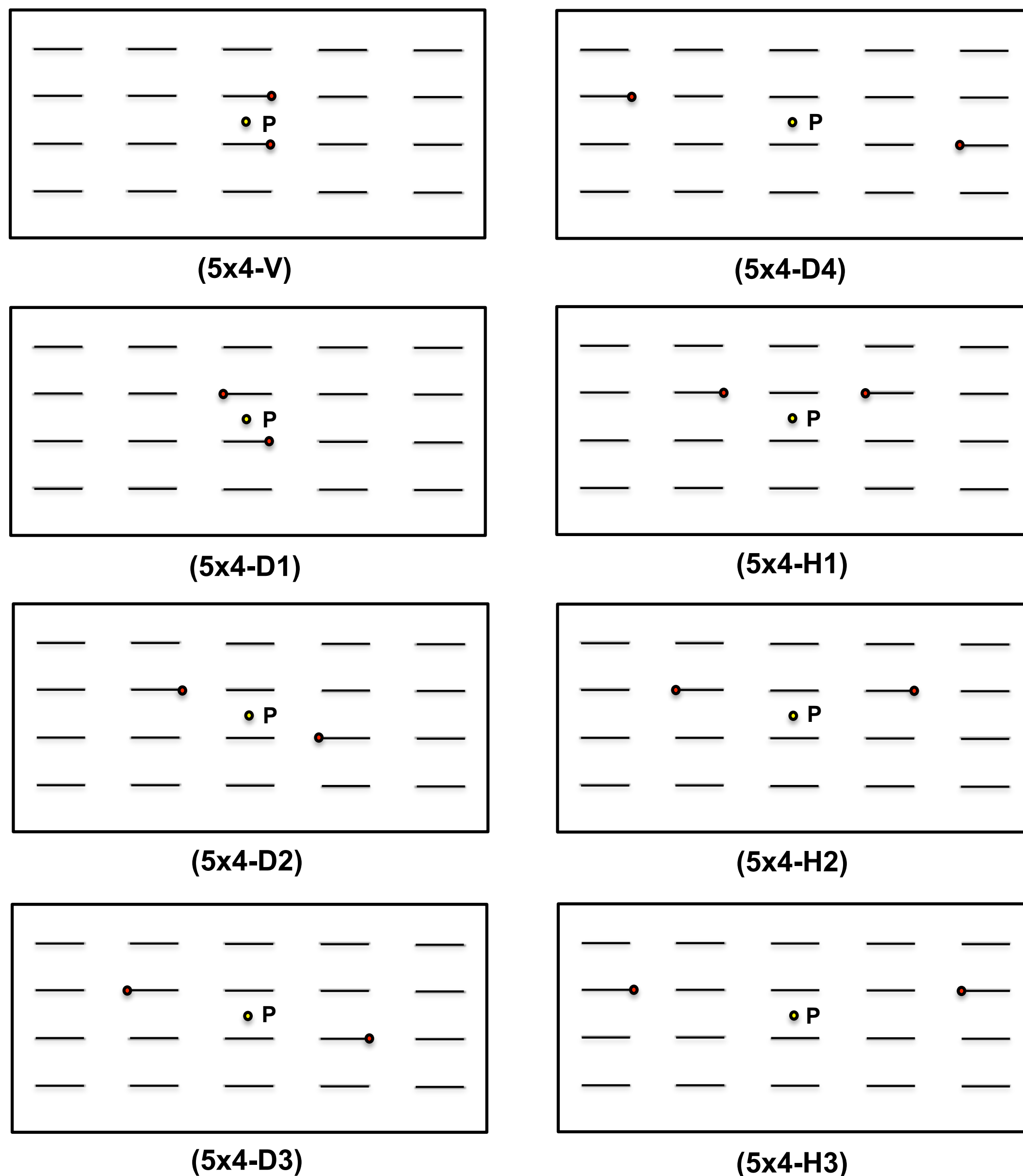

Figure A.2: DBP^- configurations on the cluster size 5×4; each cluster model has 5 rows with 4 silicon dimers per row). The rectangular box represents Si(100)-2×1 surface of a desired cluster model; horizontal short lines in each box represent Si dimers, and the red and yellow small circles represent the DBs and the P dopant, respectively. The letters V, D, and H stand for vertical, diagonal, and horizontal DBP^- configurations.

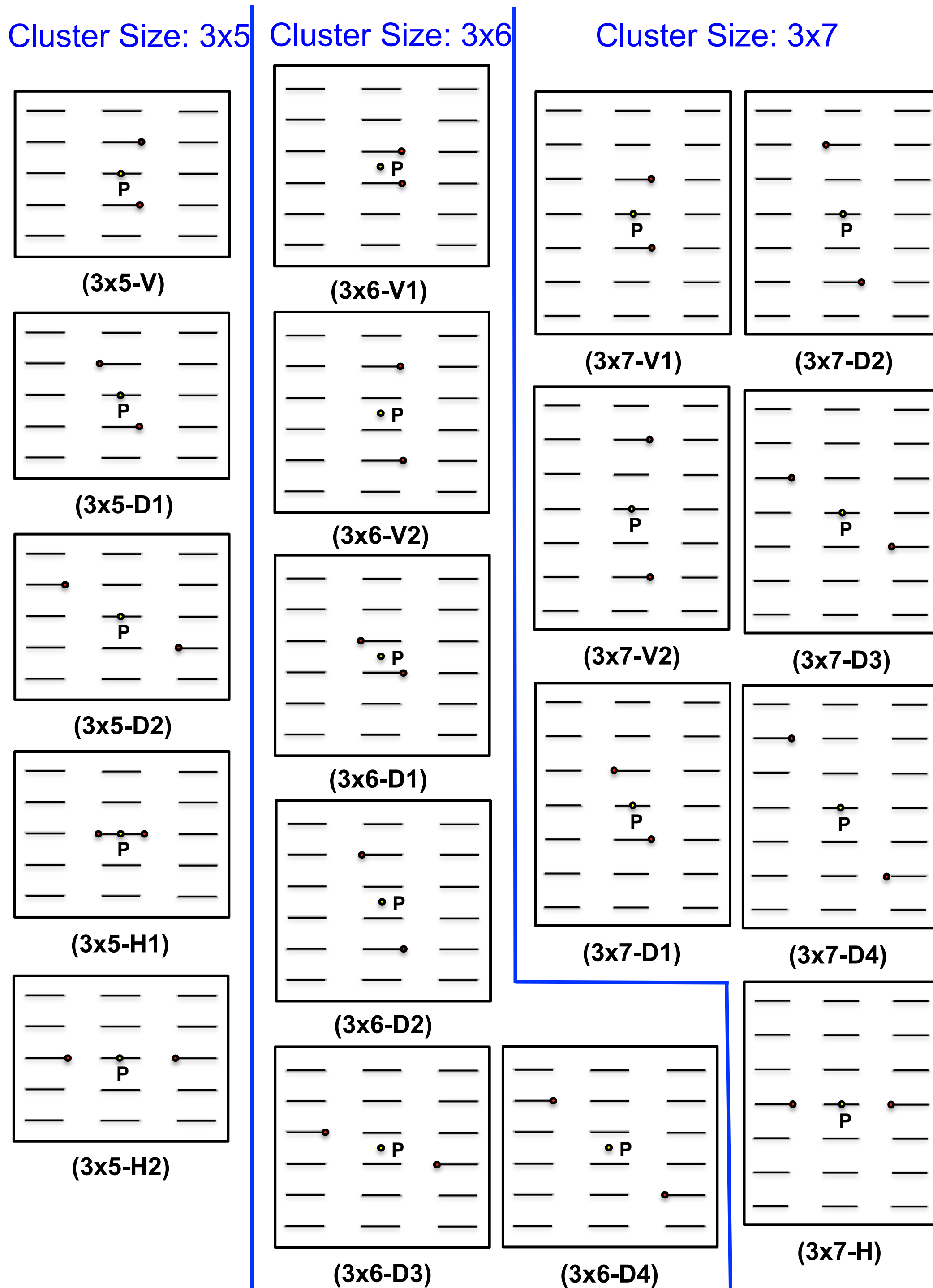

Figure A.3: DBP$^-$ configurations on cluster size $3\times m$ where $m \in \{5, 6, 7\}$; each cluster model has 3 rows and m number of dimers per row. The rectangular box represents Si(100)-2×1 surface of a desired cluster model; horizontal short lines in each box represent Si dimers, and the red and yellow small circles represent the DBs and the P dopant, respectively. The letters V, D, and H stand for vertical, diagonal, and horizontal DBP$^-$ configurations.

Appendix B

From basic theory to computation

For each cluster, a Gaussian input file is prepared, in which the number of processors and the amount of memory required for the job are allocated; desired type of calculation, basis set and theoretical method are set; molecular structure of the cluster consisting of the atomic coordinates and the charge and spin-multiplicity of the cluster are given, and any additional constraint is also specified. Depending on the size of clusters, we used 4, 6, or 12 processors and 15 to 22 GB of memory. The type of calculation was selected to be either DFT or TDDFT. The calculations are done using B3LYP as the theoretical method and 6-31G(d) as the basis set. The atomic coordinates of the clusters are built by a graphical interface called GaussView, and calculations took from 15 to 30 days to be completed.

Usually, the file starts with a line defining the location of the scratch files and the amount of memory and the number of processors allocated to the job. Then, the required sections, known as 'route section', 'title section' and 'molecule specification section' are set. In the route section, the desired functional, basis set, and the type of calculation should be specified. The title section contains descriptive information about the job. This information would appear in the output file and help remembering what had been pursued in that job. In the molecule specification section, we need to specify the electronic and physical structure of the cluster. This section begins with specifying the electronic structure including the 'charge' and the 'spin multiplicity' of the cluster and then is followed by introducing the coordinates of the atoms in that cluster.

Charge specification corresponds to the total charge added to or subtracted from a cluster. For a neutral cluster, the charge should be set to zero, whereas for a charged or uncharged one, this is changed to a positive or a negative integer, respectively. Spin multiplicity of a

cluster is given by the number of unpaired electrons plus +1, or alternatively is given by $2S + 1$ where S is the total spin of the cluster. Paired charges do not contribute to this quantity, but each unpaired charge contributes $+1/2$ to S. In my cluster samples, I set the charge to 0 and the spin multiplicity to 2, because the excess charge of the dangling bond pairs belongs to the phosphorous atom and it is obviously an unpaired charge.

Physical structure of a cluster is specified by the type of atoms it contains, and their coordinates. Position of atoms can be set in Cartesian format, or internal format or a mixture of both. In Cartesian format, each atom of the cluster is specified by its symbol, and its x, y, and z coordinates, whereas in the internal coordinate the location of atoms are specified using the bond lengths, bond angles, and dihedral (torsion) angles between an atom and its neighboring ones. Mixture of both formats is useful when some parts of a cluster is more easily specified in one format whereas other parts are more easily described by the other one. I use Cartesian coordinates to specify the structure of my clusters.

For large multi-atomic systems, manual preparation of the systems' structure is difficult. However, there are other ways that would greatly facilitate the preparation of the cluster structure in a desired coordinate format. For instance, we can use a graphical interface such as GaussView or a drawing package utility such as NewZMat. Alternatively, we can obtain this information from an experimental literature or a previous calculation. I use GaussView to prepare the crystal structures of my interest, and then extract the atoms coordinates in Cartesian format to use in the corresponding Gaussian input files.

The input file can contain an optional section determining values for the variables used in the molecular-structure specification section. For instance, in my cluster samples, I freeze in place the hydrogen atoms that are located on the edges of the clusters. For better understanding of the structure of a Gaussian input file, a (shortened) sample is given below:

```
%Chk=Fig3x4-V.chk

%mem=15GB
```

```
%nprocshared=4

# opt=modredundant B3LYP 6-31G(d)


3x4 Si cluster, with DBs in vertical configuration and one dimer-spacing apart


0 2

Si    5.78322038 -8.83162745 3.45524010
⋮
P     0.00000000 0.00000000 -4.16545106
⋮
H      -1.88186705 -1.63253191 4.85080865 X 165 B

⋮
X 237 B

X * F
```